ABSTRACT

Title of Dissertation: NONLINEAR PROPAGATION OF ORBITAL ANGULAR MOMENTUM LIGHT IN TURBULENCE AND FIBER

Henry F Elder
Doctor of Philosophy, 2024

Dissertation directed by: Professor Phillip Sprangle
Department of Physics
Department of Electrical and Computer Engineering

Light that carries orbital angular momentum (OAM), also referred to as optical vortices or twisted light, is characterized by a helical or twisted wavefront $\propto \exp[im\varphi]$. In contrast to spin angular momentum (SAM), where photons are limited to two states, OAM allows for, in principle, an infinite set of spatially orthogonal states. OAM-carrying light has found applications ranging from quantum key distribution in free space and guided-wave communication systems, particle trapping and optical tweezers, nanoscopy, and remote sensing. Understanding how OAM light propagates through complex environments, and how to efficiently generate particular OAM states, is critical for any such application.

In the first part of this dissertation, we describe how OAM light propagates through a turbulent atmosphere. We build analytic models which describe (1) the OAM mode mixing caused by turbulence, (2) the evolution of short, high-power OAM pulses undergoing the effects

of self-phase modulation (SPM) and group velocity dispersion (GVD), and (3) the evolution of high-power Gaussian pulses including SPM, GVD, and turbulence. The models are validated against both experimental data and nonlinear, turbulent pulse propagation simulation programs, the latter of which we have made freely available. We also explore how self-focusing can minimize certain deleterious effects of turbulence for OAM light.

The second part of this dissertation considers nonlinear effects of OAM light propagating in azimuthally symmetric waveguides. Such waveguides have so-called spin-orbit (SO) modes, which are quantized based on their total angular momentum (TAM). We develop a generalized theory of four wave mixing-based parametric amplification of SO modes and show that these processes conserve TAM, but under certain circumstances can be taken to conserve SAM and OAM independently. Our theory is validated against a nonlinear multimode beam propagation simulation program which we developed and, again, have made freely available.

NONLINEAR PROPAGATION OF ORBITAL ANGULAR MOMENTUM LIGHT IN TURBULENCE AND FIBER

by

Henry F Elder

Dissertation submitted to the Faculty of the Graduate School of the
University of Maryland, College Park, in partial fulfillment
of the requirements for the degree of
Doctor of Philosophy
2024

Advisory Committee:
Professor Phillip Sprangle, Chair
Professor Thomas Murphy
Professor Howard Milchberg
Professor Thomas Antonsen
Professor Wendell Hill III

© Copyright by
Henry F Elder
2024

Dedication

To Julia, Violet, and Audrey.

Acknowledgements

Research is rarely an individual effort, and this dissertation is no different; as such, many individuals are owed thanks. First, I would like to thank my advisor Professor Phillip Sprangle. As a part-time PhD student there were frequent administrative and professional hurdles we often had to navigate; his grace and flexibility (and first-hand knowledge of Navy / government employment) not only made my time at UMD feasible, but quite enjoyable.

I also received significant support from key people at my "day job" as a physicist at the Naval Surface Warfare Center, Carderock Division. First, I thank my supervisors Jessica McElman and Natalie Alvarez, who supported my desire to pursue a PhD and made it possible. I also thank Drs. Jack Price and Paul Shang, who were critical in my receiving funding through the Extended Term Training (ETT) and In-house Laboratory Independent Research (ILIR) programs. In addition, Drs. Brian Glover, Tim Bole, Meagan Schaal, Srikanth Raghavan, and Steve Potashnik, for serving as guiding stars for professional life after the PhD.

I also thank Prof. Thomas Murphy and Dr. Sai Kanth Dacha for many enlightening discussions regarding fiber optics and OAM light in waveguides.

The University's High Performance Computing (HPC) IT personnel also deserve thanks. Much of the simulation work involved in this dissertation ran on UMD's Deepthought2 computing cluster (before it was retired and replaced by Zaratan). While utilizing a supercomputer is a daunting task, the HPC group made it remarkably easy and user-friendly.

And finally, my wife Julia – who may be more excited than I am for my evenings and weekends to be freed up.

Table of Contents

Dedication ii
Acknowledgements iii
Table of Contents iv
List of Figures vi
List of Acronyms xi
Chapter 1 Introduction 1
1.1 A Brief of History and Context 1
1.2 Dissertation Outline 3
Chapter 2 Low-Intensity, Continuous-Wave Orbital Angular Momentum Beams in Turbulence 8
2.1 Chapter Overview 8
2.2 Optical Orbital Angular Momentum Modes in Free Space 8
2.3 Optical Beams in Atmospheric Turbulence 13
2.4 Laguerre-Gauss Mode Spectrum in Turbulence 17
2.4.1 Analytic Characterization of LG Mode Mixing 18
2.4.2 Comparison to Simulations 21
2.4.3 Impact of RMS Spot Size on Remaining Pump Mode Power 25
2.4.4 Comparison to Experiment 27
2.5 Summary 28
Chapter 3 High-Intensity, Orbital Angular Momentum Pulses in Turbulence 30
3.1 Chapter Overview 30
3.2 Dispersion and Nonlinear Polarization 31
3.2.1 Dispersion 31
3.2.2 Nonlinear Polarization 32
3.3 Governing Equation for High-Intensity Pulse Propagation in Turbulence 34
3.4 Self-Focusing to Mitigate Turbulence 37
3.5 Dynamics of Short, High-Power Laguerre-Gauss Pulses Without Turbulence 40
3.5.1 Analytic Expression for the Spot Size and Pulse Length 40
3.5.2 Comparison to Simulations 42
3.6 Dynamics of Short, High Power Gaussian Pulses in Turbulence 45
3.6.1 Analytic Expression for the Spot Size and Pulse Length 45
3.6.2 Comparison to Simulations 47
3.6.3 Comparison to Experiment 49
3.7 Mitigating Optical Turbulence With Kerr Focusing for OAM Light 51
3.8 Conclusions 55
Chapter 4 High-Power Orbital Angular Momentum Beams in Waveguides 57
4.1 Chapter Overview 57
4.2 Spin-Orbit Modes in Waveguides 58
4.3 Four-Wave Mixing of Spin-Orbit Modes: Theory 62
4.4 Comparison To Simulations 66
4.4.1 Simulation Overview 66
4.4.2 Scalar Modulation Instability of the (0,+, –8) Spatial Mode 69

4.4.3 Cross Phase Modulation Instability of the (0,±,+2) Spatial Modes 72
4.5 Generation of New Spatial Modes 73
4.6 Conclusions 76
Chapter 5 Future Work 78
Appendix A: Simulations of Low Power Beams in Turbulence 79
Appendix B: Simulations of High-Power Pulses in Turbulence 83
Appendix C: Simulations of High-Power Pulses in Waveguides 88
List of Publications and Talks 91
Collection of MATLAB Scripts and Functions 92
References 109

List of Figures

Figure 1.1: Experimental demonstrations of optical angular momentum, by transferring that angular momentum to objects. (a) A circularly polarized Gaussian beam has its polarization flipped by a half wave plate, thus imparting $2\hbar$ of angular momentum to the plate per photon. (b) A linearly polarized Laguerre-Gauss beam is absorbed by a particle, thus imparting $m\hbar$ of angular momentum to the particle per photon. 2

Figure 1.2: Schematic for low-intensity propagation of a CW OAM beam in atmospheric turbulence. Here, m indicates the OAM mode of the beam. With an initially pure OAM mode m_0, turbulence will mix the modal content, effectively changing the expectation value for the beam's OAM. 3

Figure 1.3: Schematic for a self-focused OAM beam propagating in atmospheric turbulence. As will be discussed, turbulence has an inner scale length ℓ_0 which characterizes the lower spatial bound at which distortions rapidly drop off. If a beam maintains an RMS spot-size W smaller than ℓ_0 via self-focusing, the degradation by turbulence can be reduced. 5

Figure 1.4: A typical experimental setup and result of FWM-based parametric amplification of SO modes in fibers. The number of lobes in the field profiles indicate the OAM m, while the circular arrow indicates the dominant polarization. BPF: band pass filter, OSA optical spectrum analyzer. 6

Figure 2.1: Illustrations of various LG modes. The top and bottom image of each set are the mode's intensity and phase profile, respectively. All modes shown have w = 1.3 cm and $f = \infty$, and each image is 4 × 4 cm. The mode indices p and m dictate the number of π and 2π phase shifts in the radial and azimuthal directions, respectively. Each 2π wrapping of phase is highlighted as a dashed white line for clarity. 12

Figure 2.2: Illustration of the energy cascade theory for turbulence, from Andrews and Phillips [17]. Large scale wind shear and convection generates eddies with "outer" length scale L_0, which further produce smaller eddies, cascading down to ones with "inner" scale length ℓ_0. Near the surface of the Earth L_0 is typically on the order of the altitude while ℓ_0 is on the order of 1 ~ 10 mm. 14

Figure 2.3: Examples of Kolmogorov and modified von Kármán spectra. The inner scale length ℓ_0 = 2 cm and the outer scale length L_0 = 20 m. The Kolmogorov spectrum is often sufficiently accurate when considering transverse length scales (perpendicular to the propagation direction) between ℓ_0 and L_0. The rapid drop-off in Φ_n for $\kappa > \kappa_m$ is a critical aspect to utilizing Kerr-induced self-focusing to "beat" atmospheric turbulence. 16

Figure 2.4: An example of the intensity and phase distortions of a light beam caused by atmospheric turbulence. The beam spreading (the increased size of the beam) and scintillation (speckling) are apparent, and are often detrimental to applications such as remote sensing and communication. Less obvious, but also important, is the OAM mode mixing, which is often driven by phase distortions. 17

Figure 2.5: Mixing of two OAM channels. Two LG mode pumps (p_1,m_1) and (p_2,m_2) are sent through a turbulent region. The power remaining in each channel is the remaining pump power plus the power transferred from all other modes. Note that some of the pump power will be injected into non-input modes, symbolized by the arrows "leaving" the propagation channel. 18

Figure 2.6: The fractional power transferred from LG mode (2,2) to modes (p',m') as a function of $\varepsilon = w/2^{1/2}\rho_0$, for $p' = 0$ and $m' = -2$ to 6. The filled circles represent the split-step simulation results, the dashed lines Eq. (2.4.8) (without quadratic approximation), and the solid lines Eq. (2.4.9) (with quadratic approximation). The left figures (*a*,*c*,*e*) correspond to $m' \le m$, and the right (*b*,*d*,*f*) to $m' \ge m$. 22

Figure 2.7: The fractional power transferred from LG mode (2,2) to modes (p',m') as a function of $\varepsilon = w/2^{1/2}\rho_0$, for $p' = 1$ to 3 and $m' = -2$ to 6. The filled circles represent the split-step simulation results, the dashed lines Eq. (2.4.8) (without quadratic approximation), and the solid lines Eq. (2.4.9) (with quadratic approximation). The left figures (*a*,*c*,*e*) correspond to $m' \le m$, and the right (*b*,*d*,*f*) to $m' \ge m$. 23

Figure 2.8: The fractional power transferred from LG mode (2,2) to modes (p',m') as a function of $\varepsilon = w/2^{1/2}\rho_0$, for $p' = 4$ to 6 and $m' = -2$ to 6. The filled circles represent the split-step simulation results, the dashed lines Eq. (2.4.8) (without quadratic approximation), and the solid lines Eq. (2.4.9) (with quadratic approximation). The left figures (*a*,*c*,*e*) correspond to $m' \le m$, and the right (*b*,*d*,*f*) to $m' \ge m$. 24

Figure 2.9: The fractional power remaining in various input LG mode as a function of $(2p+|m|+1)^{1/2}\varepsilon$, where $\varepsilon = w/2^{1/2}\rho_0$ and $W = (2p+|m|+1)^{1/2} w$ is the RMS spot size of the (p,m) LG mode. The different tick marks represent the split-step simulation results, and the solid lines Eq. (2.4.9). 26

Figure 2.10: (a) Picture of the OAM transmitter and receiver systems. The light propagates 200 m and is reflected back by a flat mirror (red box). (b) Diagram of the receiver system, which characterizes the OAM content of the beam. (c) Measured OAM power spectrum. (d) Predicted OAM power spectrum, based on Eq. (2.4.8). (a–c) are reproduced from Ref. [24] with the permission of J. Anguita. 28

Figure 3.1: A sample phase screen for MVK turbulence with parameters: wavelength λ = 875 nm, propagation distance z = 1 km, structure constant $C_n^2 = 3\times10^{-15}$ m$^{-2/3}$, inner scale length ℓ_0 = 1 cm, and outer scale length L_0 = 20 m. The left figure shows the phase perturbations for a 40 × 40 cm aperture, while the right figure is focused down to a 1 × 1 cm aperture. The colorbars indicate the phase perturbation in radians. 39

Figure 3.2: Comparison between simulations (circles) and Eq. (3.5.5) (lines) for the spot size and pulse length parameters of short, high-peak-power, collimated and unchirped (0,1) LG pulses. The dotted black line corresponds to low power (linear) propagation. The pulses initially have (0,1) LG transverse profiles and Gaussian temporal profiles. 43

Figure 3.3: Comparison between simulations (circles) and Eq. (3.5.5) (lines) for the spot size and pulse length parameters of short, high-peak-power, focused and chirped (0,1) LG pulses. The dotted black line corresponds to low power (linear) propagation. The pulse initially has a (0,1) LG transverse profiles, Gaussian temporal profiles.... 44

Figure 3.4: Evolution of the temporal profile for a short, high-peak-power OAM pulse. The pulse initially has a (0,5) LG mode transverse profile, Gaussian temporal profile, and $1.10\times P_{\mathrm{cr}}^{(0,5)}$ peak power. Remaining parameters are the same as for Fig. 3.2. Pulse splitting can be observed, breaking the self-similar evolution assumption used for our analytic theory. 45

Figure 3.5: Comparison between simulations (circles) and Eq. (3.6.5) (lines) for the ensemble average spot size and pulse length parameters of short, collimated, chirped, high-peak-power Gaussian pulses in turbulence. The initial peak powers are $P_0 = 2.1\times P_{\mathrm{cr}}^{(0,0)} = 5.1\,\mathrm{GW}$. The dotted lines correspond to low power (linear), nonturbulent propagation. Note that the low power spot size evolution is the same for all three cases. 48

Figure 3.6: Comparison between simulations (circles) and Eq. (3.6.5) (lines) for the ensemble average spot size and pulse length parameters of short, focused, unchirped, high-peak-power Gaussian pulses in turbulence. The initial peak powers are $P_0 = 4.8\times P_{\mathrm{cr}}^{(0,0)} = 11.5\,\mathrm{GW}$. The dotted lines correspond to low power (linear), nonturbulent propagation. 49

Figure 3.7: The RMS spot size for a Gaussian beam in turbulence. The distributions are experimental and numerical simulation results. The black curve is the low power CW theory from Andrews and Phillips [17]. The red dashed line is our theory, and the green dashed line is also our theory but in the low power CW limit. Part of this figure is reproduced from Ref. [25] with the permission of M. Helle..... 50

Figure 3.8: Probability distributions and ensemble averages of the short-term centroid wander for high- and low-power OAM pulses in MVK turbulence, with initial RMS spot size $W(0)$ smaller than the turbulence inner scale length ℓ_0. The two cases largely behave similarly, which is consistent with the Gaussian pulse results presented by Helle *et al*. [25]. 52

Figure 3.9: Probability distributions and ensemble averages of the short-term hot-spot sizes for high- and low-power OAM pulses in MVK turbulence, with initial RMS spot size $W(0)$ smaller than the turbulence inner scale length ℓ_0. The self-focused pulses maintain a much higher power density, which is consistent with the Gaussian pulse results presented by Helle *et al*. [25]. 53

Figure 3.10: Probability distributions and ensemble averages of the (0,1) mode weight of the peak-power segment for high- and low-power OAM pulses in MVK turbulence. The cases with initial RMS spot size $W(0)$ smaller than the turbulence inner scale length ℓ_0, both high- and low-power, stay in the (0,1) mode much longer than the $W(0) > \ell_0$. 54

Figure 4.1: A generic refractive index profile for an azimuthally symmetric fiber, which supports SO modes. Analytically, the cladding is often taken to extend to infinity. The z-axis points in or out of the page. 59

Figure 4.2: (a) Refractive index profile for the air-core ring fiber under consideration. (b) Field profiles of the (0,–,+2) and (0,+,+8) modes. The mode solving procedure utilized generates profiles with purely real F^z components and purely complex F^+ and F^- components. (c) Relative strengths of mode components for select fiber modes, quantified per Eq. (4.4.3). The radial orders p is omitted to keep the figure more legible but are equal to 0. All quantities displayed are evaluated at 1.064 μm..... 68

Figure 4.3: Simulation and theory results of a pump in the (0,–,+8) spatial mode at 1.064 μm, 1 kW peak power, and propagating over 3 m. The two pairs of peaks are also in the (0, –,+8) spatial mode, and are characteristic of SMI. 70

Figure 4.4: Simulation and theory results of a pump in the (0,–,+8) spatial mode at 1.064 μm, 100 W power, and propagating over 30 m. Compared to the prior case, the lower power and longer fiber length allows for new signals with narrower bandwidths. 71

Figure 4.5: Simulation and theory results of pumps in the (0,+,+2) and (0,–,+2) spatial modes at 1.064 μm, 100 W power, and propagating over 30 m. The set of peaks with the slow mode (higher β_1) Stokes shifted and fast mode (lower β_1) anti-Stokes shifted is consistent with the XPMI phenomenon..... 73

Figure 4.6: New modes created by *degenerate* FWM-based parametric amplification from (0,+,+2) and (0,–,+2) pumps at 1.064 μm. The radial orders p is omitted to keep the figure more legible, but are equal to 0. The last numbers in the mode labels are the wavelengths in μm. Processes that conserve SAM and OAM independently are marked with blue circles, while those that only conserve TAM are marked with red x's..... 74

Figure 4.7: Modes created by *nondegenerate* FWM-based parametric amplification with (0,+,+2) and (0,–,+2) pumps at 1.064 μm. The radial orders p is omitted to keep the figure more legible, but are equal to 0. The last numbers in the mode labels are the wavelengths in μm. Processes that conserve SAM and OAM independently are marked with blue circles, while those that only conserve TAM are marked with red x's..... 75

Figure A.1: Illustration of the split-step beam propagation method for a low power CW beam in turbulence. Each step size Δz obeys $\sigma_R^2(\Delta z) \ll 1$, such that the Rytov approximation is valid..... 81

Figure A.2: Simulation results for the propagation of a low power CW Gaussian beam in Kolmogorov turbulence. The average on-axis intensity and beam wander are compared to analytic relations. 82

Figure B.1: Illustration of the nonlinear split-step beam propagation method for a high-power pulse in turbulence. The step size obeys $\Delta\eta \ll L_{\mathrm{NL}}$ where $L_{\mathrm{NL}} = 8n_0^2 \big/ 3k_0\chi^{(3)}\left|U\right|_{\max}^2$ is the characteristic nonlinear length scale. The phase screens are separated by L_T, which satisfies $\sigma_R^2(L_T) \ll 1$ 85

Figure B.2: Simulation results for the propagation of high power Gaussian pulse water. The left and right figures show the evolution of the envelope magnitudes along the x and τ axes, respectively. The peak power is large enough to instigate self-focusing and pulse splitting, but not enough to cause collapse. The black traces show what the linear evolution would be. 86

Figure C.1: Simulation results for the propagation of a bright-dark soliton pair. Without the nonlinear interactions the pulses would lengthen to about 1 ps..... 89

List of Acronyms

BPF – Band Pass Filter

CW – Continuous Wave

FWM – Four Wave Mixing

GVD – Group Velocity Dispersion

LCP – Left Circular Polarization

LG – Laguerre Gauss

MCF – Mutual Coherence Function

MVK – Modified von Kármán

MM-GNLSE – Multimode Nonlinear Schrödinger Equation

OAM – Orbital Angular Momentum

OSA – Optical Spectrum Analyzer

RCP – Right Circular Polarization

RMS – Root Mean Square

SAM – Spin Angular Momentum

SLM – Spatial Light Modulator

SMI – Scalar Modulation Instability

SO – Spin Orbit

SPM – Self Phase Modulation

TAM – Total Angular Momentum

TE – Transverse Electric

TM – Transverse Magnetic

XPM – Cross Phase Modulation

XPMI – Cross Phase Modulation Instability

Chapter 1 Introduction

1.1 A Brief of History and Context

From Maxwell's theory, it is readily observable that electromagnetic waves carry momentum [1]. This momentum can be split into linear and angular contributions. Borrowing a concept from atomic physics, angular momentum can be further separated into spin and orbital components.

Spin angular momentum (SAM) was first observed by Beth [2] when he considered the torque exerted on a half-wave plate by a light beam. SAM is related to the polarization of an electromagnetic field: each photon in the field carries $\sigma_{\pm}\hbar$ of SAM, where $\sigma_{\pm} = +1$ for left-circularly polarized (LCP) light or $\sigma_{\pm} = -1$ for right-circularly polarized (RCP) light. (Throughout this dissertation we utilize the convention that LCP light has *positive* helicity, whereas RCP light has *negative* helicity.) Since a half-wave plate flips the handedness of light that propagates through it, each photon will impart $2\hbar$ of angular momentum to the plate. Thus, under illumination by circularly polarized light, the plate rotates, with the rotation direction dependent on the polarization of the light. This process is depicted in Figure 1.1(a).

It wasn't until the seminal paper by Allen *et al.* [3] that a similar quantization of orbital angular momentum (OAM) was presented. They found that the Laguerre-Gauss (LG) modes of light, which have a characteristic $\exp[im\varphi]$ phase dependence, result in a measure of $(\sigma_{\pm}+m)\hbar$ total angular momentum per photon. An analogous experiment to Beth's followed by spinning laser-trapped particles with a linearly polarized OAM beam [4]; this is depicted in Fig. 1.1(b).

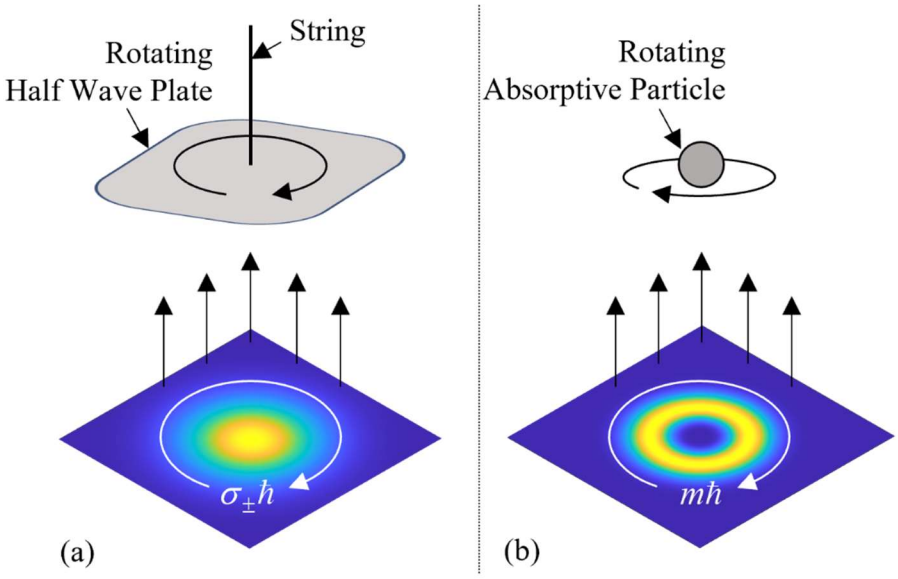


Figure 1.1: Experimental demonstrations of optical angular momentum, by transferring that angular momentum to objects. (a) A circularly polarized Gaussian beam has its polarization flipped by a half wave plate, thus imparting $2\hbar$ of angular momentum to the plate per photon. (b) A linearly polarized Laguerre-Gauss beam is absorbed by a particle, thus imparting $m\hbar$ of angular momentum to the particle per photon.

OAM light has since found applications ranging from remote sensing [5] [6], classical and quantum communication [7] [8] [9], particle trapping and optical tweezers [10], and microscopy [11] [12]. Understanding how OAM light propagates through complex environments, and how to efficiently generate particular OAM states, is critical for any such application. In the first part of this dissertation, we describe how atmospheric turbulence distorts OAM beams, often changing or “mixing up" the modal composition. We then explore how Kerr-induced self-focusing can be leveraged to reduce such distortions. In the second part, we describe how specific OAM states are generated via four-wave mixing-

based parametric amplification in specially designed fibers, and the unique selection rules that arise in such interactions.

1.2 Dissertation Outline

While the two main parts of this dissertation both involve OAM light, the physical characteristics of how such light behaves in bulk and in waveguides necessitates a bifurcated organization. In addition, the combination of numerous phenomena in the first part (OAM light, turbulence, self-focusing, and dispersion) naturally leads to an intricate presentation. Therefore, it is worthwhile to provide an overview on the structure of this dissertation.

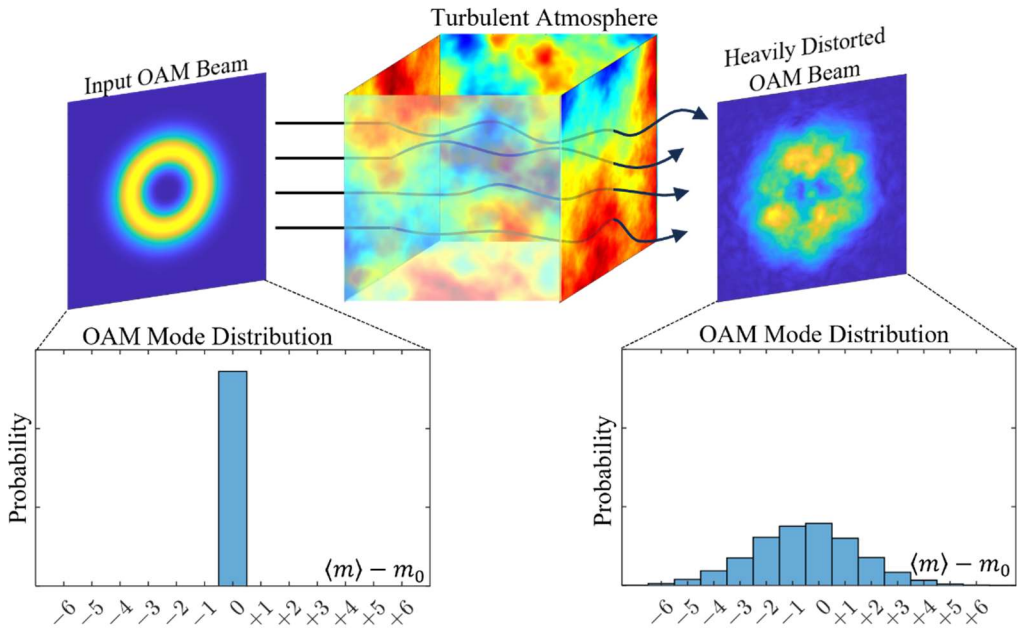


Figure 1.2: Schematic for low-intensity propagation of a CW OAM beam in atmospheric turbulence. Here, m indicates the OAM mode of the beam. With an initially pure OAM mode m_0, turbulence will mix the modal content, effectively changing the expectation value for the beam's OAM.

Chapter 2 discusses how atmospheric turbulence distorts OAM light in the linear regime. It starts with a formal presentation of OAM light in free space, followed by a brief background on the phenomenology of atmospheric turbulence and its effects on non-OAM light. It then develops an analytical model describing how low-intensity, continuous-wave (CW) OAM beams evolve in atmospheric turbulence, as depicted in Figure 1.2. The model is validated against numerical simulations and is shown to be valid into the strong turbulence regime – an often elusive goal. The model is also compared to experimental results which illustrate the importance of capturing the higher-radial-order mode behavior.

In Chapter 3, we move from low-intensity CW beams to high-intensity pulses, with the aim of describing how self-focused OAM light propagates through atmospheric turbulence. First, nonlinear susceptibility and dispersion are introduced, followed by a derivation of the governing nonlinear wave equation that dictates how light propagates under the combined effects of diffraction, dispersion, turbulence, and self-phase modulation (SPM). We then develop an analytic model for how OAM beams evolve under the combined effects of SPM and GVD and validate it against numerical simulations. The model is then augmented by including turbulence. By comparing the model to experimental data and numerical simulations, we show that it can accurately describe the evolution of short, high-intensity Gaussian pulses in turbulence. Unfortunately, the model is not accurate for OAM light, since such light is exceptionally prone to filamentation at high intensities – an effect not considered in our analysis. At the

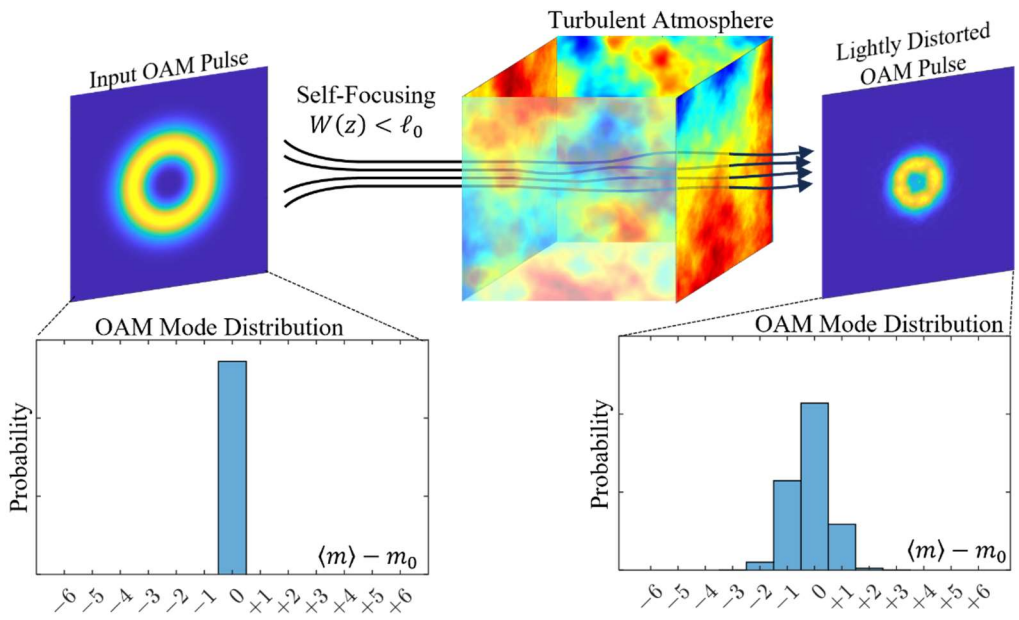


Figure 1.3: Schematic for a self-focused OAM beam propagating in atmospheric turbulence. As will be discussed, turbulence has an inner scale length ℓ_0 which characterizes the lower spatial bound at which distortions rapidly drop off. If a beam maintains an RMS spot-size W smaller than ℓ_0 via self-focusing, the degradation by turbulence can be reduced.

end of the chapter, we show how self-focusing can reduce turbulence-induced distortions for OAM light. This behavior is depicted in Figure 1.3.

In Chapter 4 we move on from atmospheric propagation and consider propagation in fiber waveguides. We first provide an introduction to the structure of so-called "Spin-Orbit" (SO) fiber modes. We then use the Multimode Generalized Nonlinear Schrödinger's equation to study how these SO modes undergo nonlinear interactions, with a focus on how new SO modes can be generated via four wave mixing (FWM). This process is depicted in Figure 1.4. We show that, along with the typical selection rules for FWM processes

(conservation

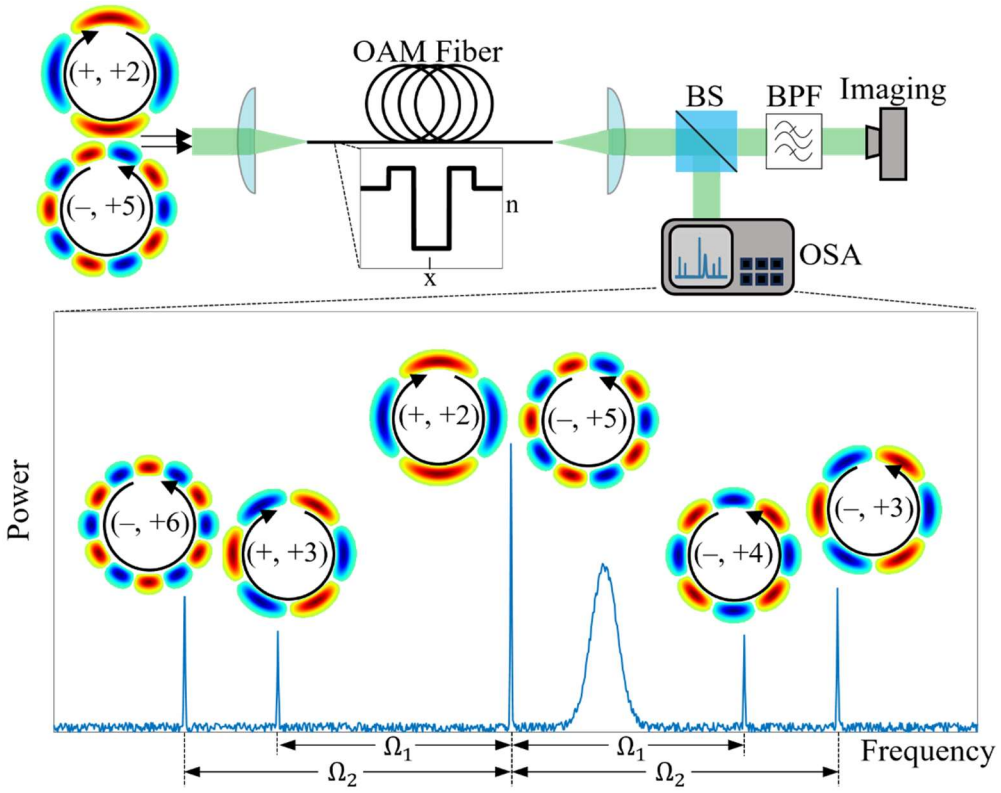


Figure 1.4: A typical experimental setup and result of FWM-based parametric amplification of SO modes in fibers. The number of lobes in the field profiles indicate the OAM *m*, while the circular arrow indicates the dominant polarization. BPF: band pass filter, OSA optical spectrum analyzer.

---

of linear momentum and energy), the total angular momentum must also be conserved. These predictions are further tested against numerical simulations.

Throughout this dissertation we make use of numerical simulations to test the accuracy of analytic models. There are three fundamental beam propagation programs:

Program 1: Low-power, CW beams in turbulence,

Program 2: High-power pulses in turbulence, and

Program 3: Two-spatial-mode, high-power pulses in fiber.

These simulation routines were developed by the author. Details on how these simulations are performed, along with sample MATLAB scripts and functions for performing such calculations, are provided in the Appendices. The code has also been made available for download online at https://gitlab.com/henry.elder/nonlin-beam-prop.

Chapter 2 Low-Intensity, Continuous-Wave Orbital Angular Momentum Beams in Turbulence

2.1 Chapter Overview

To study the combined effects of OAM, turbulence, SPM, and dispersion, we begin with a relatively simple configuration and build upon it. The starting point is developing a model for how turbulence mixes the OAM states of low-intensity, CW beams. By "low intensity" we mean that the peak field intensity is sufficiently small such that the medium's nonlinear susceptibility (and thus SPM) is negligible; and with CW light, we mean that the beam is sufficiently narrowband such that the medium's dispersive properties are negligible. Both of these effects will be introduced later in Chapter 3.

This chapter is organized as follows. First, in section 2.2, we introduce the free-space modes of light that carry OAM. Then, in section 2.3, we review the basic phenomenology of atmospheric turbulence. In section 2.4 we derive our analytic models of how OAM modes are distorted by turbulence and their validation against split-step simulations and experimental data.

2.2 Optical Orbital Angular Momentum Modes in Free Space

We start with a formal introduction to OAM modes of light. Consider Maxwell's equations in macroscopic media,

$$\begin{aligned} \nabla \cdot \mathbf{D} &= \rho_f, \\ \nabla \cdot \mathbf{B} &= 0, \\ \nabla \times \mathbf{E} + \partial_t \mathbf{B} &= 0, \\ \nabla \times \mathbf{H} &= \mathbf{J}_f + \partial_t \mathbf{D}, \end{aligned} \tag{2.2.1}$$

where $\mathbf{E}$ and $\mathbf{H}$ are the electric and magnetic fields, $\mathbf{D}$ and $\mathbf{B}$ are the electric and magnetic flux densities, $\mathbf{J}_f$ is the free current density and ρ_f the free charge

density. All quantities are functions of space and time ($\mathbf{r}$,t). The fields and fluxes are related by the constitutive relationships

$$\begin{aligned} \mathbf{D} &= \varepsilon_0 \mathbf{E} + \mathbf{P}, \\ \mathbf{B} &= \mu_0 (\mathbf{H} + \mathbf{M}), \end{aligned} \tag{2.2.2}$$

where $\varepsilon_0 \approx 8.85\times10^{-12}$ F/m is the vacuum permittivity, $\mu_0 = 4\pi\times10^{-7}$ H/m is the vacuum permeability, and **P** and **M** are the electric and magnetic polarizations.

Throughout the entirety of this dissertation we will be assuming no free charge or current ($\rho_f = 0$ and $\mathbf{J}_f = 0$) and nonmagnetic media ($\mathbf{M} = 0$). In the following, we write the electric flux density as $\mathbf{D} = \varepsilon_0 \varepsilon_r^{(1)} \mathbf{E}$, where $\varepsilon_r^{(1)}$ is the linear part of the medium's relative permittivity and is related to the refractive index n via $n^2 = \varepsilon_r^{(1)}$. Maxwell's equations, with the above stipulations, can then be formulated into the vector wave equation for **E**

$$\left[\nabla^2 - \frac{\varepsilon_r^{(1)}(\mathbf{r})}{c^2}\partial_t^2\right]\mathbf{E}(\mathbf{r},t) + \nabla\left[\mathbf{E}(\mathbf{r},t)\cdot\nabla\varepsilon_r^{(1)}(\mathbf{r})\right] = 0. \tag{2.2.3}$$

For atmospheric propagation the term $\nabla\left[\mathbf{E}(\mathbf{r},t)\cdot\nabla\varepsilon_r^{(1)}(\mathbf{r})\right]$ is small and can be neglected. This is not the case for propagation in fibers, which will be discussed in Chapter 4. Performing a temporal Fourier transform yields

$$\left[\nabla^2 + k^2(\omega)\right]\tilde{\mathbf{E}}(\mathbf{r},\omega) = 0, \tag{2.2.4}$$

where we have defined the wavenumber $k(\omega) = \sqrt{\varepsilon_r^{(1)}}\,\omega/c$. **H** is readily recovered via the Maxwell-Faraday equation. The obvious procedure is to write the electric field $\tilde{\mathbf{E}}$ as a sum of modes,

$$\tilde{\mathbf{E}}(\mathbf{r},\omega)=\frac{1}{2}\sum_{q}\hat{\mathbf{e}}_q\,a_q\,\tilde{F}_q(\mathbf{r},\omega)\exp\left[ik(\omega)z\right]+\text{c.c.}, \tag{2.2.5}$$

where q is the modal index, $\hat{\mathbf{e}}_q$ is the polarization vector, and each mode satisfies the wave equation. We then assume $\tilde{F}_q$ is slowly varying along z such that $\left|\partial_z^2\tilde{F}_q\right|\ll\left|k\partial_z\tilde{F}_q\right|$. This leads to the paraxial wave equation

$$\left[\partial_z-\frac{i}{2k(\omega)}\nabla_\perp^2\right]\tilde{F}_q(\mathbf{r},\omega)=0. \tag{2.2.6}$$

One set of solutions to the paraxial wave equation are the aforementioned Laguerre-Gauss (LG) modes, defined in cylindrical coordinates (r,ϕ,z) as

$$\begin{aligned}\tilde{F}_{(p,m)}(\mathbf{r},\omega)=&\sqrt{\frac{2p!}{\pi(p+|m|)!}}\frac{1}{w(z,\omega)}\left(\frac{\sqrt{2}r}{w(z,\omega)}\right)^{|m|}\mathrm{L}_p^{|m|}\left(\frac{2r^2}{w^2(z,\omega)}\right)\\&\times\exp\left[-\left(\frac{1}{w^2(z,\omega)}+\frac{ik(\omega)}{2f(z,\omega)}\right)r^2+im\phi+i\left(2p+|m|+1\right)\theta(z,\omega)\right],\end{aligned} \tag{2.2.7}$$

where p and m are the radial and azimuthal mode numbers, $w(z,\omega)=w(0,\omega)\left[\left(1-z/f(0,\omega)\right)^2+z^2/z_R^2(\omega)\right]^{1/2}$ characterizes the transverse size of the beam, $\mathrm{L}_p^{|m|}$ is the associated Laguerre polynomial,

$$f(z,\omega)=z\frac{w^2(z,\omega)}{w^2(0,\omega)}\left[1-\frac{z}{f(0,\omega)}-\frac{w^2(z,\omega)}{w^2(0,\omega)}\right]^{-1}, \tag{2.2.8}$$

is the phase front curvature, $\theta(z,\omega)=\arctan\left[z_{\min}/z_R(\omega)\right]$ is the Gouy phase, $z_{\min}$ is the position of the beam waist, and $z_R(\omega)=k(\omega)w^2(0,\omega)/2$ is the Rayleigh length. Note that the lowest order mode, $p = m = 0$, is simply a Gaussian mode. Some LG modes are depicted in Fig. 2.1. Each mode displayed has the same

value of w, and thus one can observe the mode-order dependence of the RMS spot size W

$$W^2(z) = \frac{2\int d\mathbf{r}_\perp r^2 \left|\tilde{F}(\mathbf{r}_\perp, z)\right|^2}{\int d\mathbf{r}_\perp \left|\tilde{F}(\mathbf{r}_\perp, z)\right|^2} = (2p + |m| + 1) w^2(z). \tag{2.2.9}$$

The LG modes form a complete and orthogonal set. That is, any function $U(\mathbf{r}_\perp)$ e.g. transverse beam shape, can be decomposed into a weighted sum of LG modes, i.e. $U(\mathbf{r}_\perp) = \sum_{(p,m)} c_{(p,m)} \tilde{F}_{(p,m)}(\mathbf{r}_\perp)$ where $c_{(p,m)} = \int d\mathbf{r}_\perp U(\mathbf{r}_\perp) \tilde{F}^*_{(p,m)}(\mathbf{r}_\perp)$.

LG modes are a natural characterization of beams in azimuthally symmetric environments. Bessel beams also carry OAM [13] [14], but the LG modes have become favored for applications involving long range propagation (>100 meters). There are other solutions to the paraxial wave equation suitable for different geometries, such as the Hermite-Gauss modes for cartesian [13] and Ince-Gauss modes for elliptical [15].

If a beam starts in one of the LG modes, it will stay in that mode while propagating through a vacuum or uniform medium. Many applications of OAM light involve transmitting long ranges through the atmosphere – typically with the desire to "hit" a remote target or patch of air with light in a specific OAM state. However, Earth's atmosphere is not a uniform medium; rather, turbulence imparts a pseudo- random spatial variation to the permittivity. Understanding how

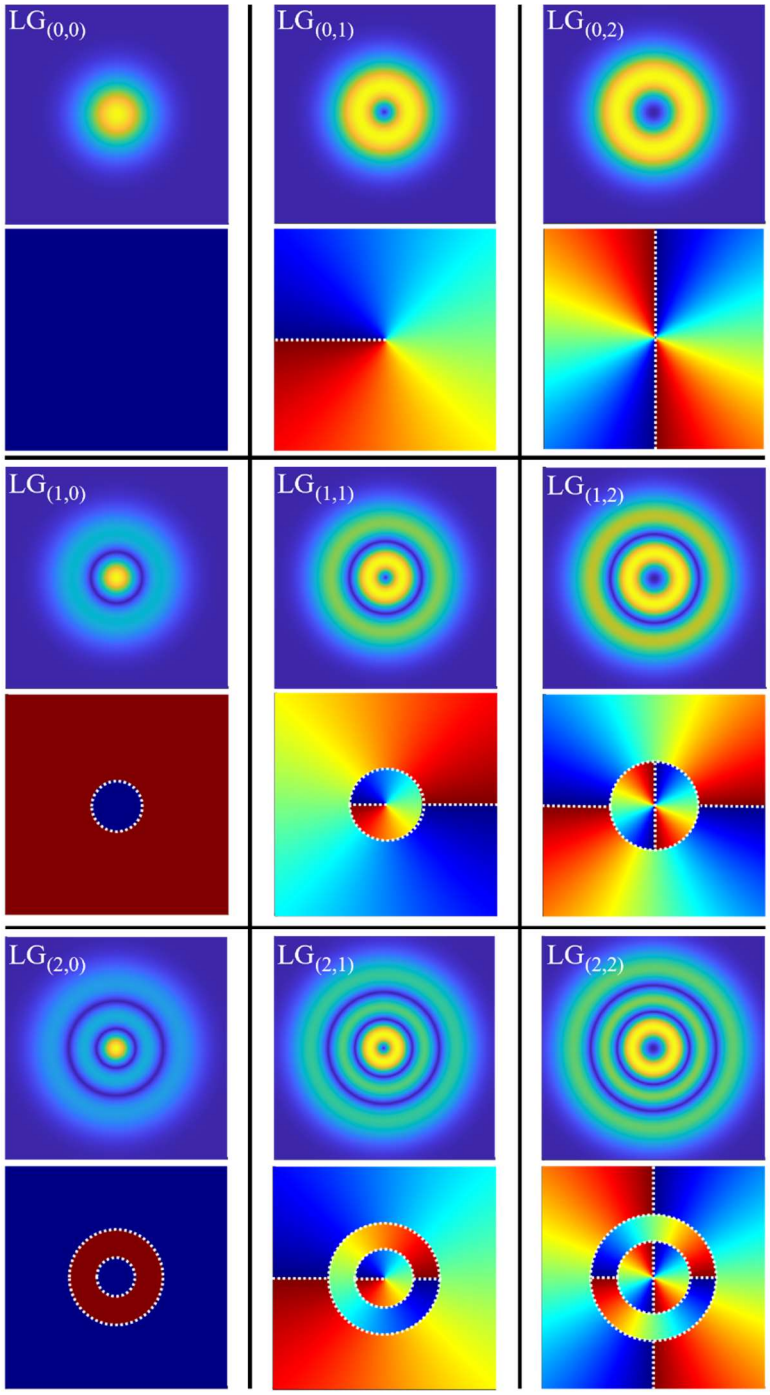


Figure 2.1: Illustrations of various LG modes. The top and bottom image of each set are the mode's intensity and phase profile, respectively. All modes shown have w = 1.3 cm and $f = \infty$, and each image is 4 × 4 cm. The mode indices p and m dictate the number of π and 2π phase shifts in the radial and azimuthal directions, respectively. Each 2π wrapping of phase is highlighted as a dashed white line for clarity.

turbulence affects OAM light is critical for assessing the viability of any atmospheric applications.

2.3 Optical Beams in Atmospheric Turbulence

Just like any fluid in a dynamic environment, the atmosphere experiences turbulent flow – that is, flow in which the air undergoes irregular fluctuations and mixing. An instructive characterization of atmospheric turbulence is energy cascade theory, introduced by Richardson [16]. In this picture, depicted in Figure 2.2, large scale wind shear and convection generate eddies in the local atmosphere. Due to the viscosity of air, these eddies continue to break up into smaller and smaller eddies until thermal diffusion dictates the energy transforms into heat. The characteristic spatial sizes of these eddies range from the outer scale length L_0 to the inner scale length ℓ_0.

Kolmogorov [17] introduced the first statistical theory of turbulence from which related characterizations of optical propagation are often derived. By using dimensional analysis, he proposed that the longitudinal structure function of wind velocity v obeys a 2/3rd power law

$$D_v(r) \equiv \left\langle \left(v(r) - v(r') \right)^2 \right\rangle = C_v^2 r^{2/3}, \ \ell_0 \ll r \ll L_0, \tag{2.3.1}$$

where $\langle a \rangle$ indicates the expectation value (ensemble average) of the parameter a and C_v^2 is the velocity structure constant. Optical propagation through the atmosphere will largely depend on the refractive index n; while n does depend on wind velocity, the air temperature is a more dominant factor. Performing an

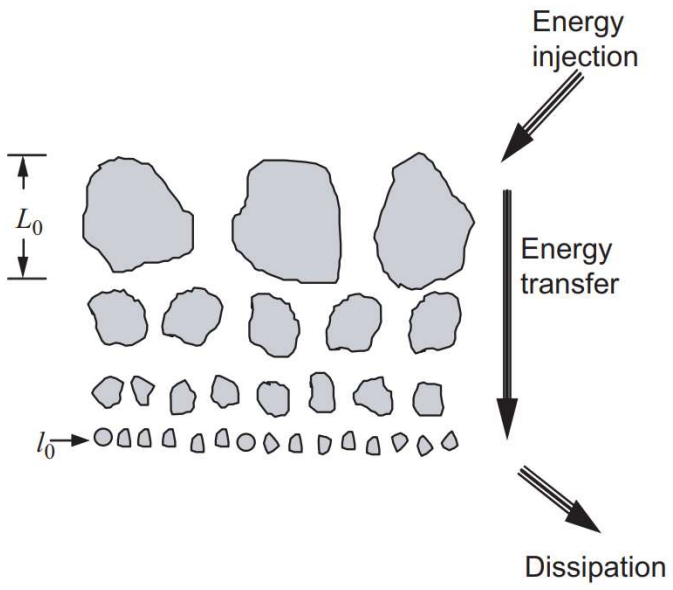


Figure 2.2: Illustration of the energy cascade theory for turbulence, from Andrews and Phillips [17]. Large scale wind shear and convection generates eddies with "outer" length scale L_0, which further produce smaller eddies, cascading down to ones with "inner" scale length ℓ_0. Near the surface of the Earth L_0 is typically on the order of the altitude while ℓ_0 is on the order of 1 ~ 10 mm.

analogous procedure to Kolmogorov's for n yields the similar structure function

$$D_n(r) \equiv \left\langle \left(n(r) - n(r') \right)^2 \right\rangle = C_n^2 r^{2/3}, \ \ell_0 \ll r \ll L_0, \tag{2.3.2}$$

where C_n^2 is the refractive index structure constant with units $\mathrm{m}^{-2/3}$ [18]. When it comes to calculations regarding the propagation of light through turbulence, the refractive index power spectral density Φ_n is a more useful quantity than the structure function. Utilizing the relationship between the structure and covariance functions for homogenous and isotropic quantities, along with the Wiener-Khinchin theorem, one can obtain

$$\Phi_n(\kappa) = 0.033 C_n^2 \kappa^{-11/3}, \ 1/L_0 \ll \kappa \ll 1/\ell_0. \tag{2.3.3}$$

Equation (2.3.3) is called the Kolmogorov spectrum. Since the work of Kolmogorov, more thorough characterizations of turbulence have been developed. In addition, certain calculations regarding light propagation in turbulence which utilize the Kolmogorov spectrum as-is end up with divergent results due to the lack of a well-defined outer scale length L_0. Other spectral models have varying balances of physical accuracy and analytic tractability. One popular "middle-ground" turbulent spectrum is the modified von Kármán (MVK) spectrum

$$\Phi_n(\kappa) = 0.033 C_n^2 \frac{\exp\left[-\kappa^2/\kappa_m^2\right]}{\left(\kappa^2 + \kappa_0^2\right)^{11/6}}, \tag{2.3.4}$$

where $\kappa_0 = 2\pi/L_0$ and $\kappa_m = 5.92/\ell_0$. Examples of the Kolmogorov and MVK spectra are shown in Fig. 2.3. One can clearly observe the effects of the finite inner and outer scale lengths: the outer scale provides a plateau for lower wavenumbers, whereas the inner scale provides a knee at which the power spectrum rapidly decays. These will be the two principal turbulent spectrum models utilized throughout this dissertation.

The strength of turbulence is often quantified using the Rytov variance, defined as $\sigma_R^2 = 1.23 C_n^2 k_0^{7/6} z^{11/6}$. Generally speaking, $\sigma_R^2 \ll 1$ corresponds to "weak" turbulence; $\sigma_R^2 \sim 1$ to "moderate" turbulence, and $\sigma_R^2 \gg 1$ to "strong" turbulence. For more details on characterizing turbulence strength, see Charnotskii [19].

The effects of turbulence on an OAM beam can be observed in Fig. 2.4. There are many quantities of interest when characterizing a distorted optical beam

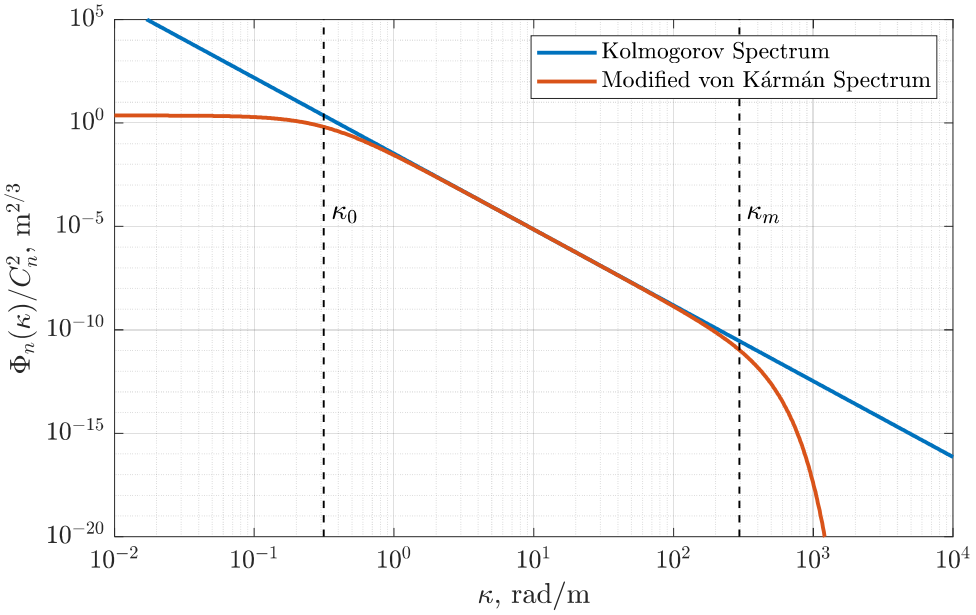


Figure 2.3: Examples of Kolmogorov and modified von Kármán spectra. The inner scale length $\ell_0 = 2$ cm and the outer scale length $L_0 = 20$ m. The Kolmogorov spectrum is often sufficiently accurate when considering transverse length scales (perpendicular to the propagation direction) between ℓ_0 and L_0. The rapid drop-off in Φ_n for $\kappa > \kappa_m$ is a critical aspect to utilizing Kerr-induced self-focusing to "beat" atmospheric turbulence.

$U(\mathbf{r}_\perp, z)$. Some of the more common are the mutual coherence function (MCF) $\Gamma_2(\mathbf{r}_\perp, \mathbf{r}'_\perp, z) = \langle U(\mathbf{r}_\perp, z) U^*(\mathbf{r}'_\perp, z) \rangle$, the long-term spot size

$$\langle W^2(z) \rangle = \frac{2\int d\mathbf{r}_\perp \, r^2 \langle |U(\mathbf{r}_\perp, z)|^2 \rangle}{\int d\mathbf{r}_\perp \langle |U(\mathbf{r}_\perp, z)|^2 \rangle}, \tag{2.3.5}$$

and the scintillation index

$$\sigma_I^2(\mathbf{r}_\perp, z) = \frac{\langle |U(\mathbf{r}_\perp, z)|^4 \rangle}{\langle |U(\mathbf{r}_\perp, z)| \rangle^4} - 1. \tag{2.3.6}$$

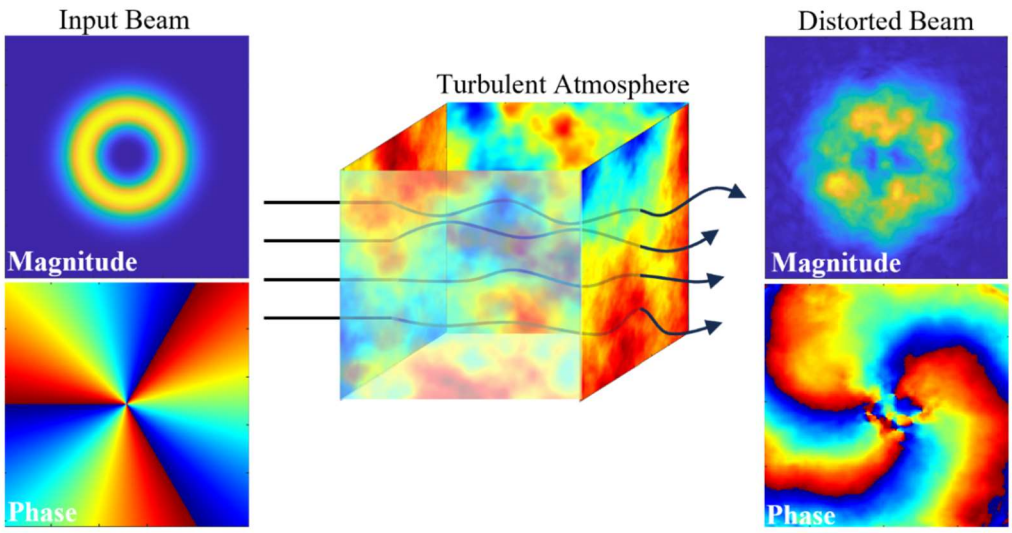


Figure 2.4: An example of the intensity and phase distortions of a light beam caused by atmospheric turbulence. The beam spreading (the increased size of the beam) and scintillation (speckling) are apparent, and are often detrimental to applications such as remote sensing and communication. Less obvious, but also important, is the OAM mode mixing, which is often driven by phase distortions.

Analytic forms for these, and other, quantities exist for planar, spherical, and Gaussian waveforms [18] [20]. While such results for LG beams do exist, they are less abundant and ill-posed for our particular needs [21] [22] [23]. Thus, our first goal is to develop a model to quantify the turbulence-induced mode-mixing for LG beams.

2.4 Laguerre-Gauss Mode Spectrum in Turbulence

As discussed, atmospheric turbulence creates a temporal and spatial varying refractive index which can distort optical fields. In the context of OAM light, turbulence causes mixing between OAM states. This mixing process is illustrated in Fig. 2.5 for two pump LG states, (p_1, m_1) and (p_2, m_2). The total power in each mode consists of the remaining pump power, denoted $P_{(p,m)\to(p,m)}$, plus the

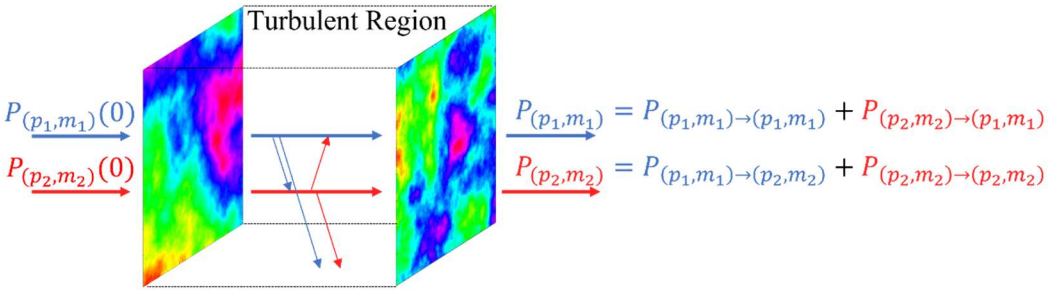


Figure 2.5: Mixing of two OAM channels. Two LG mode pumps (p_1,m_1) and (p_2,m_2) are sent through a turbulent region. The power remaining in each channel is the remaining pump power plus the power transferred from all other modes. Note that some of the pump power will be injected into non-input modes, symbolized by the arrows "leaving" the propagation channel.

power transferred from all other modes $(p',m') \neq (p,m)$, denoted $P_{(p',m')\to(p,m)}$.

An ability to predict the modal power spectrum of OAM beams after propagating through turbulence would be beneficial in its own right, but also as a step towards characterizing self-focused LG pulses in turbulence.

2.4.1 Analytic Characterization of LG Mode Mixing

The fractional power transferred from an input LG mode (p,m) to mode (p',m') after propagating through turbulence is given by

$$\frac{P_{(p,m)\to(p',m')}(z)}{P_{(p,m)}(0)} = \left\langle \left| \int d\mathbf{r}_\perp \, U_{(p,m)}(\mathbf{r}_\perp, z) \, F^*_{(p',m')}(\mathbf{r}_\perp, z) \right|^2 \right\rangle, \tag{2.4.1}$$

where $U_{(p,m)}(\mathbf{r}_\perp, z)$ is the beam, initially in the (p,m) LG state, after propagating through turbulence, and F indicates diffraction-only propagation given by Eq. (2.2.7). Expanding the norm in Eq. (2.4.1), it is apparent that we will need to determine the MCF for LG beams $\Gamma_{(p,m)}(\mathbf{r}_\perp, \mathbf{r}'_\perp, z) = \left\langle U_{(p,m)}(\mathbf{r}_\perp, z) U^*_{(p,m)}(\mathbf{r}'_\perp, z) \right\rangle$.

To do so, we start with the paraxial wave equation (Eq. (2.2.6)) modified to account for a spatially-varying refractive index $n(\mathbf{r}) = n_0 + \delta n(\mathbf{r})$,

$$\left[2ik_0\partial_z + \nabla_\perp^2 + 2k_0^2\frac{\delta n(\mathbf{r})}{n_0}\right]U_{(p,m)}(\mathbf{r}) = 0. \tag{2.4.2}$$

We consider propagation through air for which $n_0 \simeq 1$. Writing U as a sum of LG modes, i.e. $U_{(p,m)}(\mathbf{r}) = \sum_{(p,m)} c_{(p,m)}(z) F_{(p,m)}(\mathbf{r})$, Eq. (2.4.2) takes the form

$$\sum_{(p,m)}\left[F_{(p,m)}(\mathbf{r})\partial_z c_{(p,m)}(z) - ik_0\delta n(\mathbf{r}) c_{(p,m)}(z) F_{(p,m)}(\mathbf{r})\right] = 0, \tag{2.4.3}$$

For a well-collimated beam, i.e. the total propagation distance is much less than the Rayleigh length z_R, one can add $\sum_{(p,m)} c_{(p,m)}(z)\partial_z F_{(p,m)}(\mathbf{r}) \simeq 0$ to the left side of Eq. (2.4.3) to yield $\left[\partial_z - ik\,\delta n(\mathbf{r})\right]U_{(p,m)}(\mathbf{r}) = 0$. We consider well-collimated beams in anticipation of analyzing critically-focused beams later. This can then be manipulated into the form

$$\partial_z \Gamma_{(p,m)}(\mathbf{r}_\perp, \mathbf{r}'_\perp) = ik_0\left\langle\left(\delta n(\mathbf{r}_\perp) - \delta n(\mathbf{r}'_\perp)\right)U_{(p,m)}(\mathbf{r}_\perp)U^*_{(p,m)}(\mathbf{r}'_\perp)\right\rangle, \tag{2.4.4}$$

where the z-dependence of the variables has been suppressed for clarity. It can be shown that

$$\begin{aligned}\left\langle\left(\delta n(\mathbf{r}_\perp, z) - \delta n(\mathbf{r}'_\perp, z)\right)U_{(p,m)}(\mathbf{r}_\perp, z)U^*_{(p,m)}(\mathbf{r}'_\perp, z)\right\rangle \\ = ik_0\left[\mathrm{A}_n(0) - \mathrm{A}_n(\mathbf{r}_\perp - \mathbf{r}'_\perp)\right]\Gamma_{(p,m)}(\mathbf{r}_\perp, \mathbf{r}'_\perp, z),\end{aligned} \tag{2.4.5}$$

where A_n is the transverse coherence function for the refractive index [18]. Thus, the solution for the MCF is

$$\begin{aligned}\Gamma_{(p,m)}(\mathbf{r}_\perp, \mathbf{r}'_\perp, z) &= \Gamma_{(p,m)}(\mathbf{r}_\perp, \mathbf{r}'_\perp, 0)\exp\left[-k_0^2 z\left(\mathrm{A}_n(0) - \mathrm{A}_n(\mathbf{r}_\perp - \mathbf{r}'_\perp)\right)\right] \\ &= \Gamma_{(p,m)}(\mathbf{r}_\perp, \mathbf{r}'_\perp, 0)\exp\left[-\mathrm{D}_{\mathrm{pl}}\left(\left|\mathbf{r}_\perp - \mathbf{r}'_\perp\right|, z\right)/2\right],\end{aligned} \tag{2.4.6}$$

where D_{pl} is the plane wave structure function. For a Kolmogorov spectrum, $D_{pl}(\mathbf{r}_\perp, \mathbf{r}'_\perp, z) = \exp\left[-\left|\mathbf{r}_\perp - \mathbf{r}'_\perp\right|^{5/3} / \rho_0{}^{5/3}(z)\right]$ where $\rho_0(z) = \left(1.46 C_n^2 k_0^2 z\right)^{-3/5}$ is the spatial coherence radius. Assuming the input LG beam is perfectly coherent (i.e. $\Gamma_{(p,m)}(\mathbf{r}_\perp, \mathbf{r}'_\perp, 0) = F_{(p,m)}(\mathbf{r}_\perp, 0) F^*_{(p,m)}(\mathbf{r}'_\perp, 0)$), Eq. (2.4.1) takes the form

$$\begin{aligned} \frac{P_{(p,m)\to(p',m')}(z)}{P_{(p,m)}(0)} &= \int d\mathbf{r}_\perp \, d\mathbf{r}'_\perp \, F_{(p,m)}(\mathbf{r}_\perp, z) F^*_{(p,m)}(\mathbf{r}'_\perp, z) \\ &\quad \times F_{(p',m')}(\mathbf{r}'_\perp, z) F^*_{(p',m')}(\mathbf{r}_\perp, z) \exp\left[-\left|\mathbf{r}_\perp - \mathbf{r}'_\perp\right|^{5/3} / \rho_0{}^{5/3}\right] \end{aligned} \tag{2.4.7}$$

Defining $x = 2r^2/w^2$, $\varepsilon = w/2^{1/2}\rho_0$, and $\zeta = \phi' - \phi$ Eq. (2.4.7) can be written as

$$\begin{aligned} \frac{P_{(p,m)\to(p',m')}(z)}{P_{(p,m)}(0)} &= \frac{p!\,p'!}{2\pi(p+|m|)!(p'+|m'|)!} \int dx \int dx' \int d\zeta \\ &\quad \times (xx')^{(|m|+|m'|)/2} \mathrm{L}_p^{|m|}(x) \mathrm{L}_{p'}^{|m'|}(x) \mathrm{L}_p^{|m|}(x') \mathrm{L}_{p'}^{|m'|}(x') \\ &\quad \times \exp[-(x+x') + i(m-m')\zeta] \\ &\quad \times \exp\left[\varepsilon^{5/3}(x + x' - 2(xx')^{1/2}\cos\zeta)^{5/6}\right]. \end{aligned} \tag{2.4.8}$$

The integrals in Eq. (2.4.8) can be difficult to evaluate due to their oscillatory nature, especially as the azimuthal mode number separation increases. One can make the so-called quadratic approximation, i.e. $\varepsilon^{5/3}(x + x' - 2(xx')^{1/2}\cos\zeta)^{5/6} \approx \varepsilon^2(x + x' - 2(xx')^{1/2}\cos\zeta)$ [18] [20]. The integral over ζ can then be carried out using the identity $\exp[\alpha\cos\zeta] = \sum_{\nu=-\infty}^{\infty} \mathrm{I}_\nu[\alpha]\exp[i\nu\zeta]$ where I_ν is the modified Bessel function of the first kind. This yields

$$\begin{aligned} \frac{P_{(p,m)\to(p',m')}(z)}{P_{(p,m)}(0)} &= \frac{p!\,p'!}{(p+|m|)!(p'+|m'|)!} \int dx \int dx' \\ &\quad \times (xx')^{(|m|+|m'|)/2} \mathrm{L}_p^{|m|}(x) \mathrm{L}_{p'}^{|m'|}(x) \mathrm{L}_p^{|m|}(x') \mathrm{L}_{p'}^{|m'|}(x') \\ &\quad \times \mathrm{I}_{|\Delta m|}\left(2(xx')^{1/2}\varepsilon^2\right) \exp[-(1+\varepsilon^2)(x+x')], \end{aligned} \tag{2.4.9}$$

where $\Delta m = m' - m$ is the azimuthal mode separation. Further, if we consider only zero radial order LG modes, i.e. $p = 0$, the integrals of Eq. (2.4.9) can be solved analytically to yield

$$\frac{P_{(0,m)\to(0,m')}(z)}{P_{(0,m)}(0)} = \frac{\Gamma^2[\alpha]}{|m|!|m'|!|\Delta m|!}\frac{\varepsilon^{2|\Delta m|}}{\left(1+\varepsilon^2\right)^{2\alpha}}\,{}_2\mathrm{F}_1\left[\alpha,\alpha;|\Delta m|+1;\frac{\varepsilon^4}{\left(1+\varepsilon^2\right)^2}\right], \quad (2.4.10)$$

where $\alpha = (|m| + |m'| + |\Delta m|)/2 + 1$ is a mode order dependent term, $|\Delta m| = |m - m'|$ is the mode separation, and ${}_2\mathrm{F}_1$ is the Gaussian hypergeometric function. This is a remarkably tidy result for strong turbulence analysis.

2.4.2 Comparison to Simulations

Numerical simulations based on the split-step beam propagation method are used to test Eqs. (2.4.8) and (2.4.9). Details on how such simulations are performed are presented in Appendix A. We consider a collimated beam, initially in the (p,m) = (2,2) LG state with wavelength λ = 875 nm and zero-order spot size w = 33.25 mm (RMS spot size $W = \sqrt{2p+|m|+1}\,w$ = 88 mm) propagating 500 m in turbulent air. These parameters correspond to a propagation distance of ~13% of a Rayleigh length, such that the beam remains well collimated. The structure constant C_n^2 is presumed to be uniform throughout the propagation channel, and multiple simulation sets are performed for C_n^2 ranging from 5.1×10^{-15} to 6.4×10^{-13} $\mathrm{m}^{-2/3}$ to cover weak to strong turbulence. For each simulation, the beam is decomposed into LG modes per Eq. (2.4.1) every 50 meters. The mode basis considered includes p = 0 to 6 and m = –2 to 6 for a total of 63 modes.

The simulation results, along with the analytic predictions from Eqs. (2.4.8) and (2.4.9), are shown in Figs 2.6 – 2.8 where $P_{(2,2)\to(p',m')}(z) / P_{(2,2)}(0)$ is plotted as a function of $\varepsilon = w/\sqrt{2}\,\rho_0$. The results are separated out for specific values of p' and for $m' \le m$ and $m' \ge m$. The circles are the simulation results, the dashed lines Eq. (2.4.8) (without the quadratic approximation), and the solid lines Eq. (2.4.9) (with quadratic approximation). The parameter ε does not have a one-to-one relationship to the Rytov variance σ_R^2, but the parameters chosen with ε = 0.1 to 10 corresponds to $\sigma_R^2 = 3\times10^{-4}$ to 7 and thus represents very weak to strong turbulence.

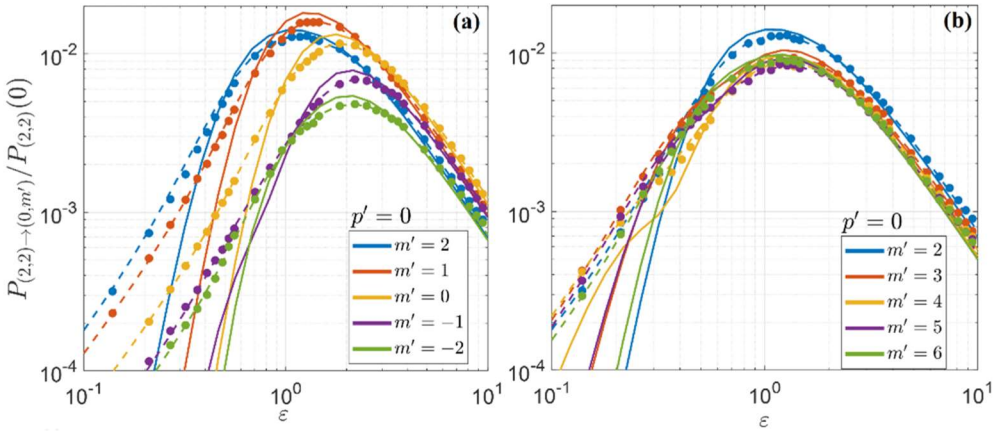


Figure 2.6: The fractional power transferred from LG mode (2,2) to modes (p',m') as a function of $\varepsilon = w/2^{1/2}\rho_0$, for p' = 0 and m' = –2 to 6. The filled circles represent the split-step simulation results, the dashed lines Eq. (2.4.8) (without quadratic approximation), and the solid lines Eq. (2.4.9) (with quadratic approximation). The left figures (*a*,*c*,*e*) correspond to $m' \le m$, and the right (*b*,*d*,*f*) to $m' \ge m$.

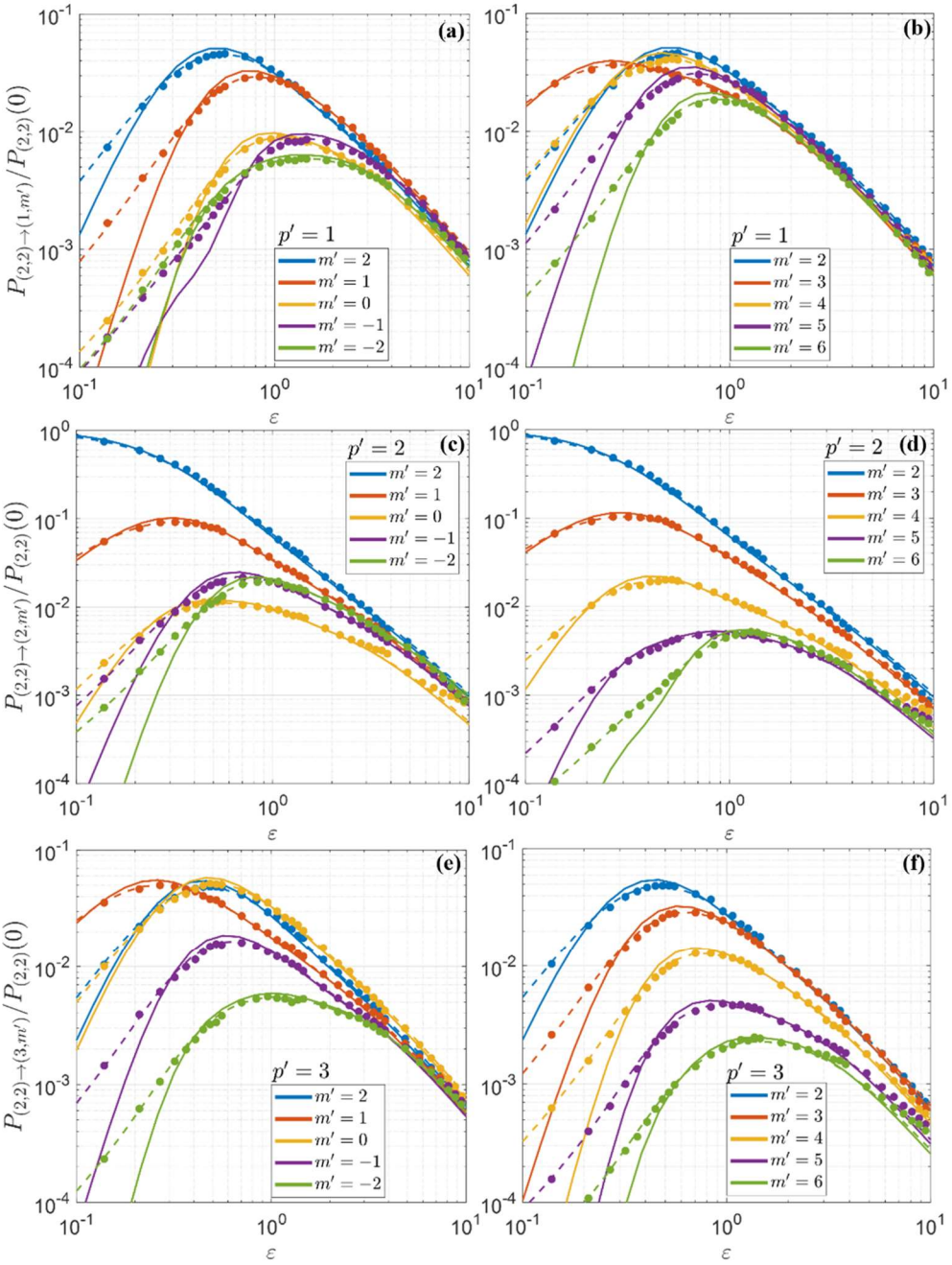


Figure 2.7: The fractional power transferred from LG mode (2,2) to modes (p',m') as a function of $\varepsilon = w/2^{1/2}\rho_0$, for p' = 1 to 3 and m' = –2 to 6. The filled circles represent the split-step simulation results, the dashed lines Eq. (2.4.8) (without quadratic approximation), and the solid lines Eq. (2.4.9) (with quadratic approximation). The left figures (a,c,e) correspond to $m' \le m$, and the right (b,d,f) to $m' \ge m$.

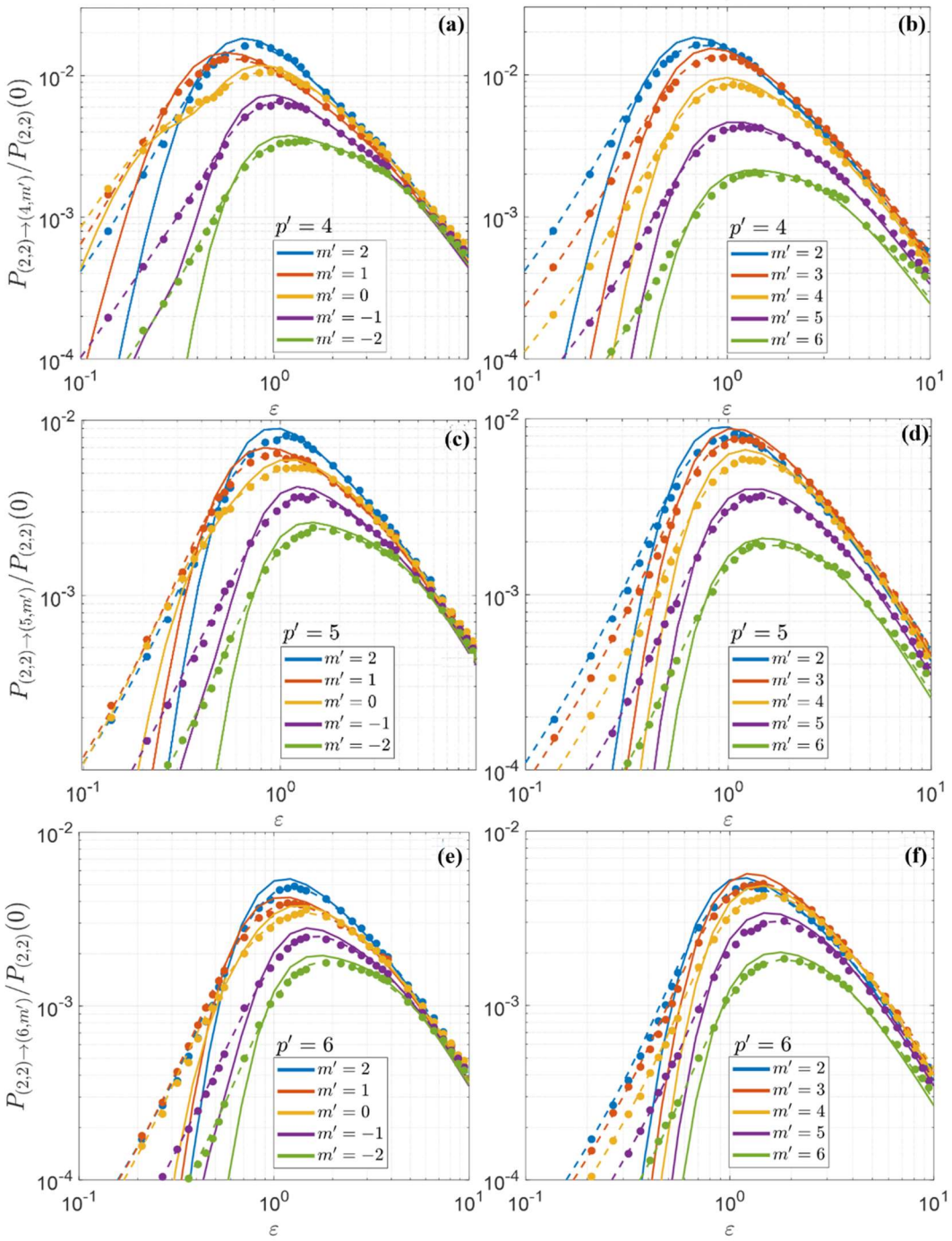


Figure 2.8: The fractional power transferred from LG mode (2,2) to modes (p',m') as a function of $\varepsilon = w/2^{1/2}\rho_0$, for p' = 4 to 6 and m' = –2 to 6. The filled circles represent the split-step simulation results, the dashed lines Eq. (2.4.8) (without quadratic approximation), and the solid lines Eq. (2.4.9) (with quadratic approximation). The left figures (a,c,e) correspond to $m' \leq m$, and the right (b,d,f) to $m' \geq m$.

We find that the analytic result without the quadratic approximation (Eq. (2.4.8)) is accurate for all turbulence strengths and decomposition modes tested. The analytic result with the quadratic approximation (Eq. (2.4.9)) is accurate for all decomposition modes tested and $\varepsilon \gtrsim 1$ but can lead to an underprediction of mode power when $\varepsilon < 1$. Note that for our parameter sets, $\varepsilon \approx 1$ corresponds to $\sigma_R^2 \approx 0.02$ to 0.1, i.e. weak turbulence. Some key exceptions are the input (2,2) mode, and the (2,1), (2,3), (1,3), and (3,1) modes, for which the quadratic approximation appears accurate throughout the tested turbulence range; this may be related to the fact that these are the modes "adjacent" to the pump, and that have the most power at $\varepsilon = 0.1$ out of the modes tested: all are above $0.01 \times P_{(2,2)}(0)$. The accuracy of the quadratic approximation in the moderate and strong turbulence regime is valuable, as Eq. (2.4.9) is less oscillatory and thus more readily evaluated numerically than Eq. (2.4.8).

It is quite unexpected that the MCF for LG beams, and notionally *any* transverse profile, can be determined using the *plane wave* structure function as long as the beam is well collimated. It is known that such behavior exists for Gaussian beams [18], which makes sense physically on the grounds that a collimated Gaussian beam has the form of a spatially-localized plane wave. But higher order LG modes do not have such behavior given the azimuthal phase factor $\exp[im\phi]$.

2.4.3 Impact of RMS Spot Size on Remaining Pump Mode Power

Patterson [20] observed that the likelihood a photon initially in the (p,m) LG mode maintains $m\hbar$ OAM (regardless of the final radial mode) is largely

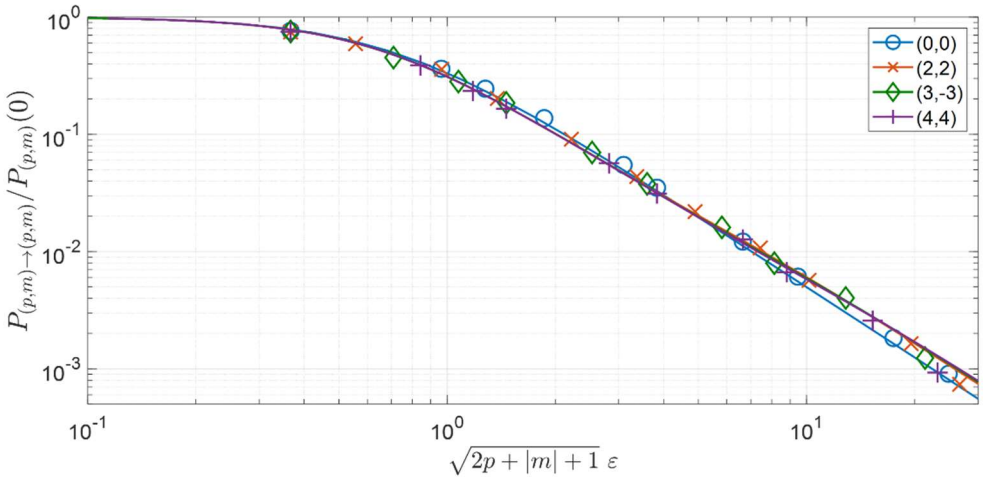


Figure 2.9: The fractional power remaining in various input LG mode as a function of $(2p+|m|+1)^{1/2}\varepsilon$, where $\varepsilon = w/2^{1/2}\rho_0$ and $W=(2p+|m|+1)^{1/2}w$ is the RMS spot size of the (p,m) LG mode. The different tick marks represent the split-step simulation results, and the solid lines Eq. (2.4.9).

dependent on the RMS spot size of the input beam. To investigate whether this behavior extends to the likelihood such a photon remains in the initial (p,m) LG mode, we performed additional simulations for beams initially in the (0,0), (3, –3), and (4,4) states with RMS spot size $W=(2p+|m|+1)^{1/2}w$ = 88 mm. All other simulation parameters are the same as described in section 2.4.2. The results are shown in Fig. 2.9 alongside the predictions based on Eq. (2.4.9). We find that the power remaining in the input (p,m) mode for collimated beams does indeed largely depend on the ratio of the RMS spot size to the plane wave coherence diameter, regardless of turbulence strength. Put another way, the topological charge only impacts the power remaining in the input mode insofar as it relates to

the RMS spot size. Note that the analytic curves for the (2,2), (3, –3), and (4,4) are very similar and are difficult to individually distinguish in the figure.

2.4.4 Comparison to Experiment

To validate our theory, we consider the experimental results obtained by Anguita *et al* [24]. In their experiment, a Gaussian beam is initially sent through a spatial light modulator (SLM) which imparts an exp[$im\varphi$] phase twist to the field profile. To good approximation, this twisted-Gaussian beam will rapidly diffract into a pure (0,m) LG mode. The beam is then propagated 400 m through atmospheric turbulence and is characterized by a receiver. The receiver consists of another SLM which imparts an exp[$-im'\varphi$] phase twist followed by a focusing lens, pinhole filter, and photodetector. Any light that maintains OAM after the receiver SLM will have a field null on-axis and will be blocked by the pinhole filter. Therefore, to reasonable approximation, the voltage generated by the photodetector will be proportional to the quantity $\sum_p P_{(0,m)\to(p,m')}(z) \Big/ P_{(0,m)}(0)$.

The experimental setup is depicted in Fig. 2.10 (a) and (b); the measured OAM spectrum for a beam initially in the (0,10) LG mode is given in (c), which is compared to the theoretical results in (d). As can be seen, the distributions is accurately predicted. The other model parameters are: wavelength λ = 660 nm, turbulence structure constant $C_n^2 = 10^{-14}$ m$^{-2/3}$, spot size parameter w = 4 cm. These values correspond to $\sigma_R^2 \approx 0.1$ and $\varepsilon = w/2^{1/2}\rho_0 \approx 1.2$.

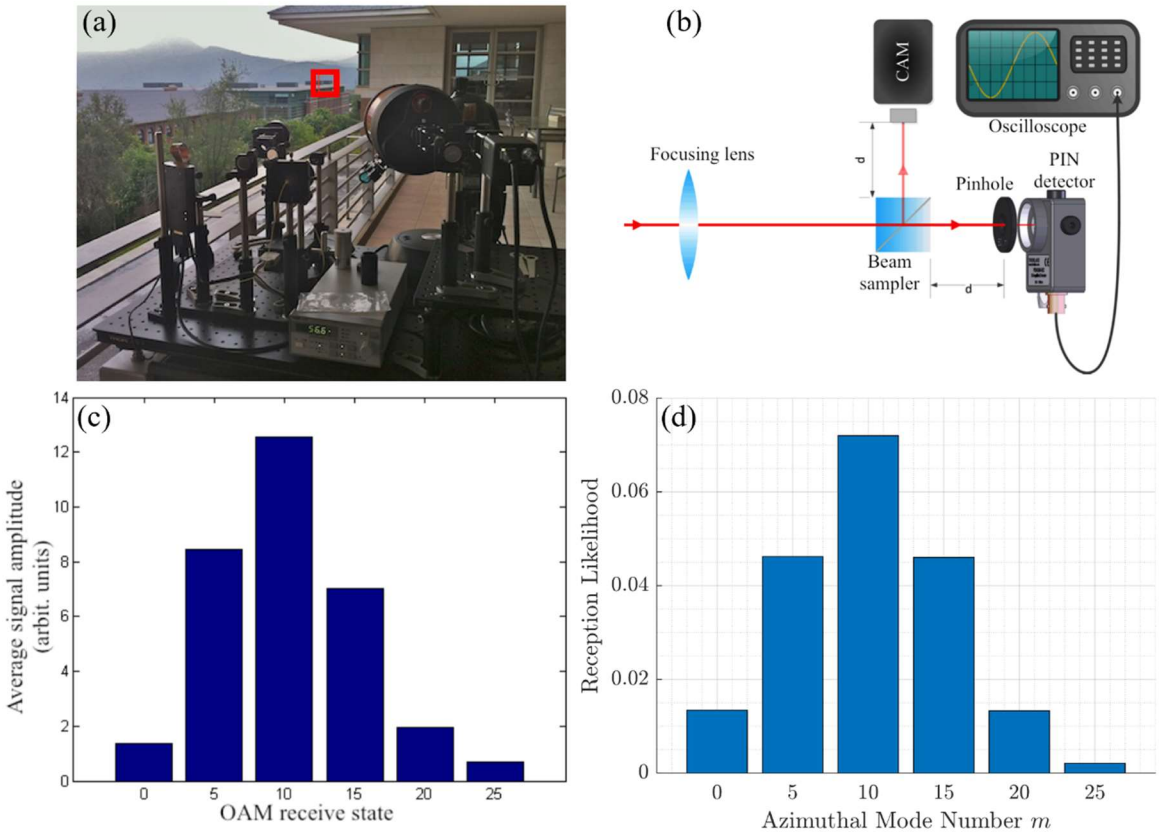


Figure 2.10: (a) Picture of the OAM transmitter and receiver systems. The light propagates 200 m and is reflected back by a flat mirror (red box). (b) Diagram of the receiver system, which characterizes the OAM content of the beam. (c) Measured OAM power spectrum. (d) Predicted OAM power spectrum, based on Eq. (2.4.8). (a–c) are reproduced from Ref. [24] with the permission of J. Anguita.

2.5 Summary

In this chapter, we covered the fundamentals of the Laguerre-Gauss (LG) OAM modes and optical turbulence. We then derived relations for the modal content of low intensity, continuous wave, collimated LG beams propagating through Kolmogorov turbulence and validated them against numerical split-step simulations. We found that:

- Our analytic relations are accurate into the strong turbulence regime (an often illusive goal).
- In weak turbulence, the quadratic approximation can lead to an underprediction of mixing for modes not adjacent to the pump.
- The mode orders p and m only impact the power remaining in the input mode insofar as it relates to the RMS spot size.

Our next step is to move from low intensity, CW beams to high power pulses. Such high power beams can undergo self-focusing, wherein the light effectively augments the refractive index of the medium such that the beam resist diffraction. We will show how self-focusing can be utilized to reduce some of the detrimental effects of turbulence observed in the chapter.

Chapter 3 High-Intensity, Orbital Angular Momentum Pulses in Turbulence

3.1 Chapter Overview

When a light beam has sufficiently high intensity, the nonlinearity of the medium's polarization response begins to affect propagation. There are numerous processes that result from this nonlinearity, one of which is self-phase modulation (SPM), wherein the light effectively augments the refractive index of the medium in a way that can cause a beam to undergo self-focusing [25]. The self-focusing phenomenon has recently been utilized to alleviate some of the deleterious effects of turbulence for Gaussian beams [26] – a principal inspiration for our query on whether this behavior extends to higher-order LG beams. To obtain sufficient intensities to observe self-focusing, one typically needs to use pulsed lasers – i.e. not CW beams like we considered in Chapter 2. This, along with the typical propagation distances of interest, means we also need to consider the effects of dispersion.

In this chapter, we explore how self-focusing of a high-power LG pulse can limit the turbulence-induced mode mixing observed in Chapter 2. This involves the intersection of four principal concepts: OAM light, turbulence, SPM, and dispersion; since this is a complicated merger, we take a fairly methodical approach. Section 3.2 provides a brief introduction to the nonlinear polarization and dispersion. In section 3.3 we derive the governing differential equation that describes light propagation under the combined effects of diffraction, dispersion, turbulence, and SPM. With a clearer understanding of the relevant phenomena, in section 3.4 we then detail the hypothesis of how one can reduce the effects of

turbulence for OAM light. In section 3.5 we develop an analytic model for how LG modes evolve under the combined effects of SPM and dispersion. This model then has turbulence introduced in section 3.6. Finally, section 3.7 discusses simulations which demonstrate the use of self-focusing to reduce the effects of optical turbulence for OAM light.

3.2 Dispersion and Nonlinear Polarization

3.2.1 Dispersion

A medium's linear relative permittivity $\varepsilon_r^{(1)}$ is a frequency dependence property, and thus the wavenumber of light takes the form $k(\omega) = \sqrt{\varepsilon_r^{(1)}(\omega)}\,\omega/c$. This relationship between k and ω is called dispersion. In Chapter 2 we considered CW light, wherein the electric field is assumed to take the form $\mathbf{E}(\mathbf{r},t) = \mathbf{U}(\mathbf{r})\exp\left[i(k_0 z - \omega_0 t)\right]/2 + \text{c.c.}$ with $k_0 = k(\omega_0)$; that is, the field only oscillates at one frequency ω_0, and thus has effectively been "turned on forever." But with pulsed light the field now carries multiple frequencies, and the frequency-dependence of k must be handled more carefully.

Dispersion is often characterized by the Taylor series of k about the carrier frequency ω_0,

$$k(\omega) = k_0 + k_1(\omega - \omega_0) + \frac{1}{2}k_2(\omega - \omega_0)^2 + \sum_{\nu>2}\frac{1}{\nu!}k_\nu(\omega - \omega_0)^\nu, \qquad (3.2.1)$$

where $k_\nu = \left(\partial^\nu k(\omega)/\partial\omega^\nu\right)_{\omega=\omega_0}$. The group velocity v_g, which describes the speed at which energy is conveyed along the wave, is related to the linear term via $v_g(\omega_0) = 1/k_1$. Group velocity dispersion (GVD), which describes how the pulse

length evolves during propagation, is given by the quadratic term k_2. Note that the GVD parameter is also often denoted as β; but in this dissertation β is reserved for the propagation constant introduced in Chapter 4.

Truncating the effects of dispersion at k_2, if a pulse is initially Gaussian in time with a chirp C, i.e. $\mathbf{E}(\mathbf{r}_\perp, z=0, t) = \mathbf{U}(\mathbf{r}_\perp)\exp\left[-(1+iC)t^2/\sigma^2(0)\right]\exp\left[i(k_0 t - \omega_0 t)\right]/2 + \text{c.c.}$, the RMS pulse length T will evolve as [13]

$$T^2(z) = \frac{4\int dt\, t^2 \left|\mathbf{E}(\mathbf{r},t)\right|^2}{\int dt \left|\mathbf{E}(\mathbf{r},t)\right|^2} = \sigma^2(0)\left[\left(1+\frac{2C_0 k_2 z}{\sigma^2(0)}\right)^2 + \left(\frac{2k_2 z}{\sigma^2(0)}\right)^2\right]. \tag{3.2.2}$$

While it may not be immediately obvious from the form of Eq. (3.2.2), chirp allows for the pulse to actually compress in time (before eventually elongating). This longitudinal behavior will be shown to couple into the pulse's transverse behavior via SPM.

3.2.2 Nonlinear Polarization

In Chapter 2, we assumed that the electric flux density **D**, electric field **E**, and induced polarization **P** were linearly related via $\mathbf{D} = \varepsilon_0 \mathbf{E} + \mathbf{P} = \varepsilon_0 \varepsilon_r^{(1)} \mathbf{E}$. We now relax this limitation and allow **P** to be nonlinear. Expanding it as a power series in frequency space

$$\tilde{\mathbf{P}} = \varepsilon_0\left[\chi^{(1)} \cdot \tilde{\mathbf{E}} + \chi^{(2)} : \tilde{\mathbf{E}}\tilde{\mathbf{E}} + \chi^{(3)} \vdots \tilde{\mathbf{E}}\tilde{\mathbf{E}}\tilde{\mathbf{E}} + \cdots\right], \tag{3.2.3}$$

where $\chi^{(j)}$ is the j'th order susceptibility tensor, and : and $\vdots$ denote tensor products. It is convenient to break **P** into linear and nonlinear parts, i.e.

$\tilde{\mathbf{P}}_{\mathrm{L}} = \varepsilon_0 \chi^{(1)} \cdot \tilde{\mathbf{E}}$ and $\tilde{\mathbf{P}}_{\mathrm{NL}} = \varepsilon_0 \left[\chi^{(2)} : \tilde{\mathbf{E}}\tilde{\mathbf{E}} + \chi^{(3)} \vdots \tilde{\mathbf{E}}\tilde{\mathbf{E}}\tilde{\mathbf{E}} \right]$, where we have truncated to third order.

In principle, $\chi^{(2)}$ and $\chi^{(3)}$ have 27 and 81 individual frequency-dependent elements, respectively. For this dissertation, we are working with light that is far from any resonances of the medium and can thus take advantage of Kleinman symmetry, which reduces the number of unique tensor elements to 10 and 15 frequency-independent values, respectively. In addition, we assume the medium is either gaseous or an amorphous liquid or glass, i.e. it is a centrosymmetric material (where the atomic arrangement is symmetric under spatial inversion $\mathbf{r} \to -\mathbf{r}$). In this case all even-order nonlinear susceptibilities are zero; further, $\chi^{(3)}$ drops down to having only three independent elements [25].

With the above stipulations, $\chi^{(3)}$'s tensor elements for the transverse coordinates are related via

$$\chi^{(3)}_{ijk\ell} = \chi^{(3)}_{xxyy}\delta_{ij}\delta_{k\ell} + \chi^{(3)}_{xyxy}\delta_{ik}\delta_{j\ell} + \chi^{(3)}_{xyyx}\delta_{i\ell}\delta_{jk}. \tag{3.2.4}$$

(We do not consider the elements related to the propagation direction *z*, since the electric field strength along that dimension will be relatively weak and thus contribute negligibly to nonlinear processes.) For example,

$$\chi^{(3)}_{xxxx} = \chi^{(3)}_{yyyy} = \chi^{(3)}_{xxyy} + \chi^{(3)}_{xyxy} + \chi^{(3)}_{xyyx}. \tag{3.2.5}$$

For our media, $\chi^{(3)}_{xxyy} \approx \chi^{(3)}_{xyxy} \approx \chi^{(3)}_{xyyx}$. Thus, for this dissertation, we can account for the nonlinear polarization with a single, frequency-independent value $\chi^{(3)}_{xxxx}$, which we will often simply label as $\chi^{(3)}$ [27].

The third order nonlinear susceptibility is responsible for phenomena such as self-phase modulation (SPM), cross-phase modulation (XPM), and four-wave mixing (FWM). Further, SPM can lead to self-focusing. To observe these phenomena one needs a sufficiently intense field: for air, $\chi^{(3)}_{xxxx} \approx 1.7\times10^{-25}$ m^2/V^2, whereas for SiO_2 and water $\chi^{(3)}_{xxxx} \approx 2.5\times10^{-22}$ m^2/V^2 [25]. Such field strengths are not trivial to obtain. For many applications, generating this level of field with a CW beam is infeasible – but it can be done with pulsed light.

3.3 Governing Equation for High-Intensity Pulse Propagation in Turbulence

With that brief introduction to dispersion and the nonlinear polarization, our next step is to derive a general governing differential equation for a light pulse under the combined effects of diffraction, dispersion, turbulence, and SPM. We start with the wave equation in frequency space, including the nonlinear polarization and a nonuniform linear permittivity,

$$\left[\nabla^2 + \varepsilon_r^{(1)}(\mathbf{r})\frac{\omega^2}{c^2}\right]\tilde{\mathbf{E}}(\mathbf{r},\omega) = -\mu_0\,\omega^2\,\tilde{\mathbf{P}}_{\mathrm{NL}}(\mathbf{r},\omega). \tag{3.3.1}$$

The variation in permittivity is assumed to be small such that $\varepsilon_r^{(1)}(\mathbf{r}) = \left(n_0 + \delta n(\mathbf{r})\right)^2 \approx n_0 + 2n_0\,\delta n(\mathbf{r})$. We also write the electric field as an envelope with carrier frequency ω_0 and polarization $\hat{\boldsymbol{\sigma}}_j$, i.e. $\mathbf{E}(\mathbf{r},t) = \hat{\boldsymbol{\sigma}}_j\,U(\mathbf{r},t)\exp\left[i\left(k_0 z - \omega_0 t\right)\right]/2 + \text{c.c.}$ where $k_0 = k(\omega_0) = n_0\omega_0/c$.

Fourier transforming **E** yields

$$\begin{aligned}\tilde{\mathbf{E}}(\mathbf{r},\omega) &= \frac{\hat{\boldsymbol{\sigma}}_j}{2}\left[\tilde{U}(\mathbf{r},\omega-\omega_0)\exp[ik_0 z]+\tilde{U}(\mathbf{r},\omega+\omega_0)\exp[-ik_0 z]\right] \\ &\simeq \frac{\hat{\boldsymbol{\sigma}}_j}{2}\tilde{U}(\mathbf{r},\omega-\omega_0)\exp[ik_0 z],\end{aligned} \tag{3.3.2}$$

where we assume the envelope is slowly varying, and thus the component oscillating at $\omega + \omega_0$ is negligible. The nonlinear polarization will also be entirely along the $\hat{\boldsymbol{\sigma}}_j$ direction, so

$$\begin{aligned}\left[\nabla_\perp^2+\partial_z^2+2ik_0\partial_z+\left(1+\frac{2\delta n(\mathbf{r})}{n_0}\right)k^2(\omega)-k_0^2\right]\tilde{U}(\mathbf{r},\omega-\omega_0) \\ = -2\mu_0\omega_0^2\tilde{P}_{\mathrm{NL}}(\mathbf{r},\omega)\exp[-ik_0 z].\end{aligned} \tag{3.3.3}$$

The next step is to expand $k(\omega)$ as a Taylor series about ω_0 and truncate to the GVD term,

$$k^2(\omega)\approx k_0^2+2(\omega-\omega_0)k_0k_1+(\omega-\omega_0)^2\left(k_1^2+k_0k_2\right). \tag{3.3.4}$$

Inserting Eq. (3.3.4) into Eq. (3.3.3), multiplying both sides by $\exp\left[-i(\omega-\omega_0)t\right]$ and integrating over $(\omega-\omega_0)$ yields

$$\begin{aligned}\left[\nabla_\perp^2+\partial_z^2+2ik_0\partial_z+\frac{2\delta n(\mathbf{r})}{n_0}k_0^2+\left(1+\frac{2\delta n(\mathbf{r})}{n_0}\right)\left[2ik_0k_1\partial_t-\left(k_1^2+k_0k_2\right)\partial_t^2\right]\right]U(\mathbf{r},t) \\ = 2\mu_0\partial_t^2P_{\mathrm{NL}}(\mathbf{r},t)\exp[-i(k_0z-\omega_0t)].\end{aligned} \tag{3.3.5}$$

We then move to the so-called retarded time reference frame, which is defined by the coordinate transforms

$$\begin{aligned}\eta = z,\ \ \tau = t-k_1z, \\ \partial_z=\partial_\eta-k_1\partial_\tau,\ \ \partial_t=\partial_\tau.\end{aligned} \tag{3.3.6}$$

In addition, we write the nonlinear polarization as an envelope equation similar to the electric field $P_{\mathrm{NL}}(\mathbf{r},t) = p_{\mathrm{NL}}(\mathbf{r},t)\exp\left[i\left(k_0 z - \omega_0 t\right)\right]/2 + \text{c.c.}$. Doing so produces

$$\begin{aligned}\left\{\nabla_\perp^2 + \partial_\eta^2 + 2ik_0\partial_\eta - 2k_1\partial_\eta\partial_\tau - k_0k_2\partial_\tau^2\right. \\ \left. + \frac{2\delta n(\mathbf{r})}{n_0}\left[k_0^2 + 2ik_0k_1\partial_\tau - \left(k_1^2 + k_0k_2\right)\partial_\tau^2\right]\right\} U(\mathbf{r}_\perp,\eta,\tau) \\ = -\mu_0\omega_0^2\left[1 + \frac{i}{\omega_0}\partial_\tau\right]^2 p_{\mathrm{NL}}(\mathbf{r}_\perp,\eta,\tau).\end{aligned} \tag{3.3.7}$$

We have found that, for pulses down to ~100 fs in length, to good approximation $\frac{2\delta n(\mathbf{r})}{n_0}\left[k_0^2 + 2ik_0k_1\partial_\tau - \left(k_1^2 + k_0k_2\right)\partial_\tau^2\right]U \approx k_0^2\frac{2\delta n(\mathbf{r})}{n_0}U$. We also enforce the slowly-varying envelope approximation (again) by assuming that the wave is principally propagating in the z direction and the envelope evolves such that $\left|\partial_\eta^2 U\right| \ll \left|k_0\partial_\eta U\right|$, the space-time term $2k_1\partial_\eta\partial_\tau$ is negligible, and $[1 + \frac{i}{\omega_0}\partial_\tau]^2 p_{\mathrm{NL}} \approx p_{\mathrm{NL}}$. We therefore arrive at

$$\left[\nabla_\perp^2 + 2ik_0\partial_\eta - k_0k_2\partial_\tau^2 + 2k_0^2\frac{\delta n(\mathbf{r})}{n_0}\right]U(\mathbf{r}_\perp,\eta,\tau) = -\mu_0\omega_0^2 p_{\mathrm{NL}}(\mathbf{r}_\perp,\eta,\tau). \tag{3.3.8}$$

To determine the appropriate form for p_{NL}, we evaluate $P_{\mathrm{NL}} = \varepsilon_0\chi^{(3)}E^3$,

$$P_{\mathrm{NL}} = \frac{1}{8}\varepsilon_0\chi^{(3)}\left\{3|U|U\exp\left[i\left(k_0 z - \omega_0 t\right)\right] + U^3\exp\left[3i\left(k_0 z - \omega_0 t\right)\right]\right\} + \text{c.c.} \tag{3.3.9}$$

The second term in Eq. (3.3.9) corresponds to third harmonic generation (THG); for this effect to have a meaningful impact the dispersion of the medium has to

satisfy the phase matching condition $3k(\omega_0) \simeq k(3\omega_0)$. Third order harmonics are neglected and the nonlinear polarization field is $p_{\mathrm{NL}} = \frac{3}{4}\varepsilon_0 \chi^{(3)} |U|^2 U$, leading to

$$\partial_\eta U(\mathbf{r}_\perp, \eta, \tau) = \left[\frac{i}{2k_0} \nabla_\perp^2 - \frac{ik_2}{2} \partial_\tau^2 + ik_0 \frac{\delta n(\mathbf{r})}{n_0} + \frac{3ik_0 \chi^{(3)}}{8n_0^2} |U|^2 \right] U(\mathbf{r}_\perp, \eta, \tau). \quad (3.3.10)$$

The term $\sim 3ik_0 \chi^{(3)} |U|^2 / 8n_0^2$ is called self-phase modulation (SPM), since the beam is effectively producing an intensity-dependent phase adjustment upon itself. With Eq. (3.3.10) we are now in a position to explore the relevant features of self-focusing, dispersion, and OAM light. Details on numerical simulations of Eq. (3.3.10) are provided in Appendix B.

3.4 Self-Focusing to Mitigate Turbulence

The intersection of OAM, dispersion, and SPM – even without the consideration of turbulence – is ripe for investigation. The key features are enumerated here for the sake of succinctness:

1. For a CW, Gaussian beam, there is a so-called critical power $P_{\mathrm{cr}}^{(0,0)} \simeq 0.2012 \varepsilon_0 c n_0 \lambda^2 / \chi^{(3)}$ for which diffraction and SPM exactly balance. In principle, this allows such a beam to travel indefinitely with an arbitrary spot size.
2. This balance is unstable. For a power $P_0 < P_{\mathrm{cr}}^{(0,0)}$, diffraction dominates and the beam will spread after a certain distance. On the other hand, for $P_0 > P_{\mathrm{cr}}^{(0,0)}$, SPM dominates and the beam will collapse. Physically, the collapse is eventually arrested by other nonlinear processes not considered

in Eq. (3.3.10) such as multi-photon ionization and plasma defocusing [25] [28].

3. The critical power depends on the initial beam profile. For the zero-radial order LG modes, the critical power scales as $P_{\mathrm{cr}}^{(0,m)} = P_{\mathrm{cr}}^{(0,0)}\ 4^{|m|}\,|m|!\big(|m|+1\big)!\big/\big(2|m|\big)!$. For example, $P_{\mathrm{cr}}^{(0,1)} = 4\,P_{\mathrm{cr}}^{(0,0)}$ and $P_{\mathrm{cr}}^{(0,2)} = 8\,P_{\mathrm{cr}}^{(0,0)}$. These high critical powers strain the balancing act for achieving stable self-focusing and avoiding collapse [29] [30].
4. In a dispersive medium, even if the peak power of a pulse is initially equal to the critical power, dispersion can cause the beam to temporally diffuse and lose its self-focusing effect. An appropriately applied chirp to the pulse can partially counteract this issue [26].

Given the above, we now elaborate on how self-focusing can limit the detrimental effects of turbulence. As discussed in Chapters 2, atmospheric turbulence has an inherent inner scale length ℓ_0, which characterizes the cutoff transverse wavenumber where the refractive index power spectral density rapidly decays. This can be observed in the sample phase screen shown in Fig. 3.1. Details on phase screens are presented in Appendix A but, in short, they are statistically accurate phase perturbations on a beam propagating through turbulence. That is, they represent $\Psi(\mathbf{r}_\perp)$ for $U(\mathbf{r}_\perp, z) = U_0(\mathbf{r}_\perp, z)\exp\big[\Psi(\mathbf{r}_\perp)\big]$, where U and U_0 are the beam after propagating a distance z with and without turbulence, respectively.

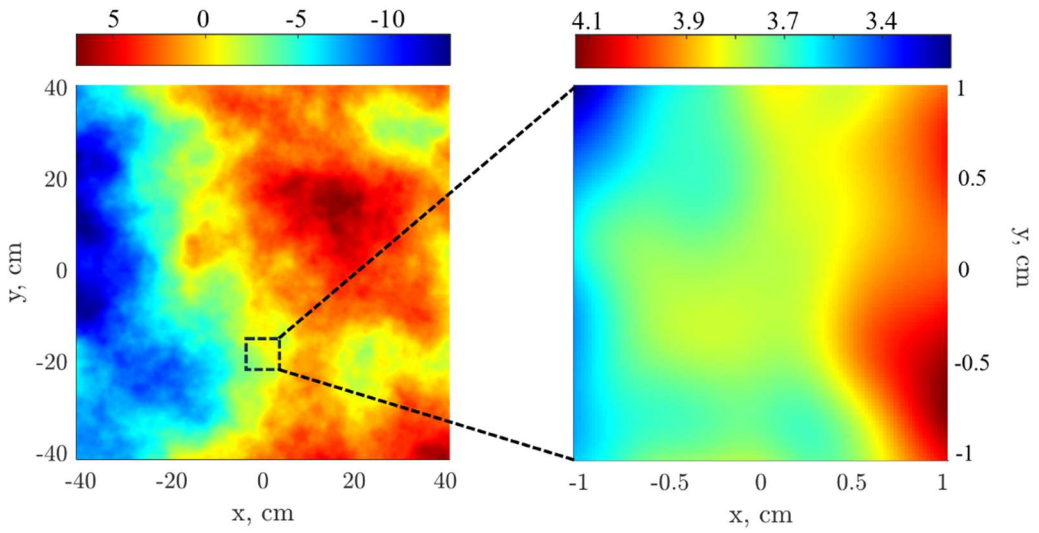


Figure 3.1: A sample phase screen for MVK turbulence with parameters: wavelength λ = 875 nm, propagation distance z = 1 km, structure constant $C_n^2 = 3\times10^{-15}$ m$^{-2/3}$, inner scale length ℓ_0 = 1 cm, and outer scale length L_0 = 20 m. The left figure shows the phase perturbations for a 40 × 40 cm aperture, while the right figure is focused down to a 1 × 1 cm aperture. The colorbars indicate the phase perturbation in radians.

As can be seen, with an inner scale length ℓ_0 = 1 cm, the phase variance that would be imparted on a beam is significantly reduced if the beam's size is $\lesssim \ell_0$. The trouble is that, for the ranges of interest for atmospheric applications ($\gtrsim$ 1 km) and the typical values of ℓ_0 (1–20 mm), a beam with a sufficiently small RMS spot size will propagate multiple Rayleigh lengths and thus diffractively spread above ℓ_0 and lose its turbulence-resistance.

The ability to utilize self-focusing to maintain a spot size under ℓ_0 for long distances for a Gaussian beam profile was recently demonstrated by Helle *et al.* [26]. They propagated a high-peak-power pulse 6 Rayleigh lengths through a controlled turbulent channel with Rytov variances σ_R^2 from 0.23 to 7.4, i.e. weak to strong turbulence. By carefully balancing the laser's output power, spot size,

pulse length, and chirp, the pulses' peak powers were maintained to be $\sim P_{\mathrm{cr}}^{(0,0)}$ with RMS spot size $W < \ell_0 \approx 2$ cm. These high-power pulses had significantly reduced scintillation and short-term spreading compared to low power pulses. This experiment leads to the question: can the same technique be applied to beams that carry OAM?

3.5 Dynamics of Short, High-Power Laguerre-Gauss Pulses Without Turbulence

Full, quantitative descriptions of the evolution of high-power laser pulses in turbulence generally require Monte Carlo simulations. While physically accurate, the large-scale calculations necessitate considerable computational resources. Thus, reduced models that capture the relevant physics are desirable. In this section we present one such reduced model that describes the evolution of spot size and pulse length for LG pulses under the effects of SPM and dispersion. Turbulence is later introduced by augmenting a term in the derived coupled equations that corresponds to diffraction with a turbulence-induced beam quality factor.

3.5.1 Analytic Expression for the Spot Size and Pulse Length

To begin, we write Eq. (3.3.10) with $\delta n(\mathbf{r}) = 0$ and an arbitrary nonlinear term S,

$$\left[2ik_0\partial_\eta + \nabla_\perp^2 - \frac{ik_2}{2}\partial_\tau^2\right]U(\mathbf{r}_\perp,\eta,\tau) = S(U,\mathbf{r}_\perp,\eta,\tau). \tag{3.5.1}$$

(The temporary use of S is to keep the following equations somewhat more tractable). Utilizing the source-dependent expansion technique [28] [31], we

represent the field U as a sum of Laguerre-Gauss modes in the transverse direction and Hermite-Gauss modes in the temporal direction, i.e.

$$\begin{aligned} U(\mathbf{r}_\perp,\eta,\tau) &= \exp\left[-\left(1+i\alpha(\eta)\right)r^2/w^2(\eta)\right]\exp\left[-\left(1+iC(\eta)\right)\tau^2/\sigma^2(\eta)\right] \\ &\quad\times\sum_{p,m,q} B_{(p,m,q)}(\eta)\left(\frac{\sqrt{2}\,r}{w(\eta)}\right)^{|m|} \mathrm{L}_p^{|m|}\left[\frac{2r^2}{w^2(\eta)}\right]\mathrm{H}_q\left[\frac{\sqrt{2}\,\tau}{\sigma(\eta)}\right]\exp\left[-im\phi\right], \end{aligned} \tag{3.5.2}$$

where α captures the curvature of the phase fronts, C the chirp, w and σ are the spot-size and pulse length parameters, and B the amplitudes. α is related to the traditional phase curvature term f via $\alpha = -k_0/2f$. Substituting Eq. (3.5.2) into Eq. (3.5.1) and using various recurrence relations between the special functions, one can arrive at

$$\begin{aligned} &G_{(p,m,q)}(\eta)B_{(p,m,q)}(\eta) - pD(\eta)B_{(p-1,m,q)}(\eta) - \left(p+|m|+1\right)D^*(\eta)B_{(p+1,m,q)}(\eta) \\ &\qquad + \frac{1}{2}F(\eta)B_{(p,m,q-2)}(\eta) + 2(q+2)(q+1)F^*(\eta)B_{(p,m,q+2)}(\eta) \\ &= \frac{1}{2^{q+1}\pi^{3/2}}\frac{p!}{q!\left(p+|m|\right)!}\int_0^\infty d\xi\int_0^{2\pi} d\phi\int_{-\infty}^{\infty} d\nu\, S\,\xi^{|m|/2}L_p^{|m|}(\xi)H_q(\nu) \\ &\qquad\qquad \times\exp\left[(-1+iC)\nu^2/2 + (-1+i\alpha)\xi/2 + im\phi\right], \end{aligned} \tag{3.5.3}$$

where G, D, and F are defined as

$$\begin{aligned} G_{(p,m,q)}(\eta) &= \frac{-2}{w^2}(2p+m+1)\left(1+\alpha^2\right) + 2ik_0\left[\frac{B'_{(p,m,q)}}{B_{(p,m,q)}} + \left(\frac{1}{2}+\left(q+\frac{1}{2}\right)iC\right)\frac{\sigma'}{\sigma}\right. \\ &\qquad \left. -\left(q+\frac{1}{2}\right)\frac{i}{2}C' + \left(1+(2p+m+1)i\alpha\right)\frac{w'}{w} - (2p+m+1)\frac{i}{2}\alpha'\right], \\ D(\eta) &= \frac{2}{w^2}(1+i\alpha)^2 + 2ik_0\left[(1+i\alpha)\frac{w'}{w} - \frac{i}{2}\alpha'\right], \\ F(\eta) &= k_0\left[(1+iC)\frac{i\sigma'}{\sigma} + \frac{1}{2}\beta' - (1+iC)^2\frac{k_2}{\sigma^2}\right], \end{aligned} \tag{3.5.4}$$

and the primes indicate derivation with respect to the longitudinal coordinate η. Next, we specify S as corresponding to Kerr focusing, i.e.

$S = -3k_0^2\chi^{(3)}|U|^2 U/4n_0^2$. It can be observed that, if the pulse is in an initial state with azimuthal mode *m*, then Eqs. (3.5.3) and (3.5.4) indicate that SPM will not cause the pulse to mix into other azimuthal states; on the other hand, radial and temporal modes will be mixed by SPM. That said, the Assuming a self-similar evolution of the (0,*m*,0) mode, one can produce the following dynamics equations for the spot size parameter *w* and pulse length parameter *σ*,

$$\begin{aligned} \partial_\eta^2 w(\eta) &= \frac{4}{k_0^2 w^3(\eta)}\left[1-\gamma k_0 \frac{E_0}{\sigma(\eta)}\right], \quad \partial_\eta w(0) = \frac{-2\alpha(0)}{k_0 w(0)} \\ \partial_\eta^2 \sigma(\eta) &= \frac{4k_2^2}{\sigma^3(\eta)}\left[1+(|m|+1)\frac{\gamma}{k_2}\frac{E_0\sigma(\eta)}{w^2(\eta)}\right], \quad \partial_\eta \sigma(0) = \frac{2k_2 C(0)}{\sigma(0)} \end{aligned} \tag{3.5.5}$$

where $\gamma = 3\Gamma(|m|+1/2)k_0\chi^{(3)}/8\pi^2\Gamma(|m|+2)n_0^3\varepsilon_0 c$ is a nonlinear coupling term and $E_0 = \pi^{3/2}n_0\varepsilon_0 c\Gamma(|m|+1)|B_{(0,m,0)}(0)|^2 w^2(0)\sigma(0)/2^{5/2}$ is the pulse energy, which is conserved. Thus, the $\chi^{(3)}$ nonlinearity effectively couples the evolution of the transverse and longitudinal profiles of the pulse. At low energies the second terms in the brackets are negligible and the equations uncouple.

3.5.2 Comparison to Simulations

To test Eq. (3.5.5), we perform nonlinear beam propagation simulations for collimated, unchirped pulses initially with (0,1) LG transverse profiles and Gaussian temporal profiles propagating through air. Details on the nonlinear simulation procedure are given in Appendix B. The peak power is varied while the remaining parameters are fixed: the initial carrier wavelength λ = 875 nm, spot size parameter $w(0)$ = 25 mm, phase curvature $f(0) = \infty$, pulse length parameter

$\sigma(0)$ = 600 fs, and chirp $C(0) = 0$. The medium is air with refractive index $n_0 \cong 1$ and nonlinear susceptibility $\chi^{(3)} = 1.7\times10^{-25}$ m^2/V^2. The simulation results, compared to Eq. (3.5.5), are shown in Fig. 3.2. We observe that the theory accurately predicts the amount of diffraction-resistance in the spot size, as well as the increased rate of pulse elongation. In addition, our model accurately accounts for GVD increasing the necessary power to cause collapse, since the $P_0 = 1.10\times P_{\mathrm{cr}}^{(0,1)}$ case diffracts rather than collapses.

We also simulated a focused, chirped pulse with $f(0)$ = 2 km and $C(0)$= –3. The initial peak power was $0.5\times P_{\mathrm{cr}}^{(0,1)}$, while the other parameters remained the same as the collimated case. The simulation results, compared to Eq. (3.5.5), are shown in Fig. 3.3. Again, we observe that the theory accurately predicts the

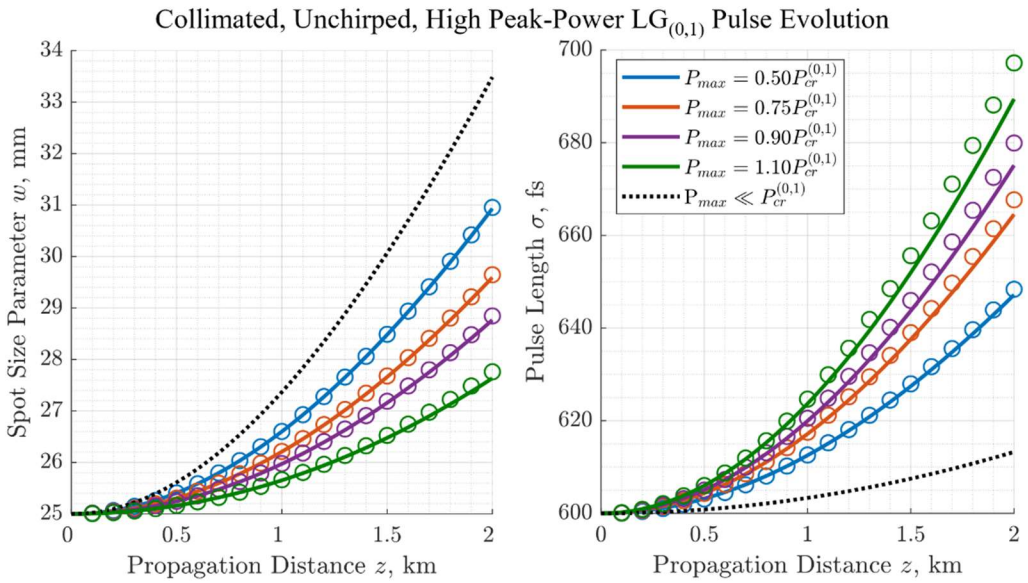


Figure 3.2: Comparison between simulations (circles) and Eq. (3.5.5) (lines) for the spot size and pulse length parameters of short, high-peak-power, collimated and unchirped (0,1) LG pulses. The dotted black line corresponds to low power (linear) propagation. The pulses initially have (0,1) LG transverse profiles and Gaussian temporal profiles.

adjusted beam waist for the spot size evolution, as well as the increased temporal spreading – both caused by self-focusing.

In certain circumstances the model breaks down. For example, we repeated the collimated, unchirped pulse simulations but for an initial (0,5) LG mode transverse profile. Inspecting the simulation results in detail, we found that the discrepancies can be traced to the self-similar evolution assumption made in the derivation. In addition to the transverse profile mixing, pulse splitting can be observed in the temporal domain, as shown in Fig. 3.4 for a $1.10\times P_{\mathrm{cr}}^{(0,5)}$ case.

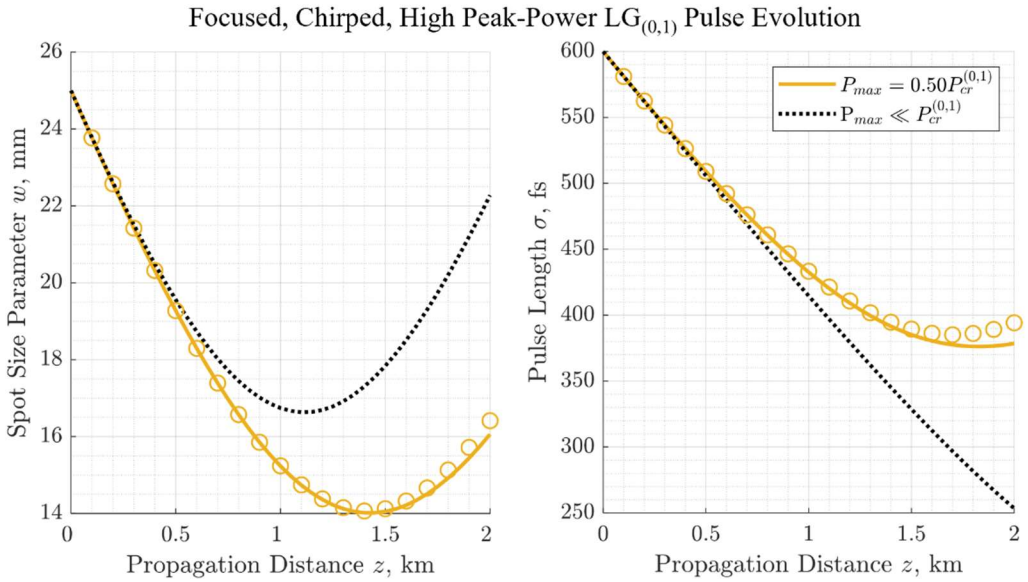


Figure 3.3: Comparison between simulations (circles) and Eq. (3.5.5) (lines) for the spot size and pulse length parameters of short, high-peak-power, focused and chirped (0,1) LG pulses. The dotted black line corresponds to low power (linear) propagation. The pulse initially has a (0,1) LG transverse profiles, Gaussian temporal profiles.

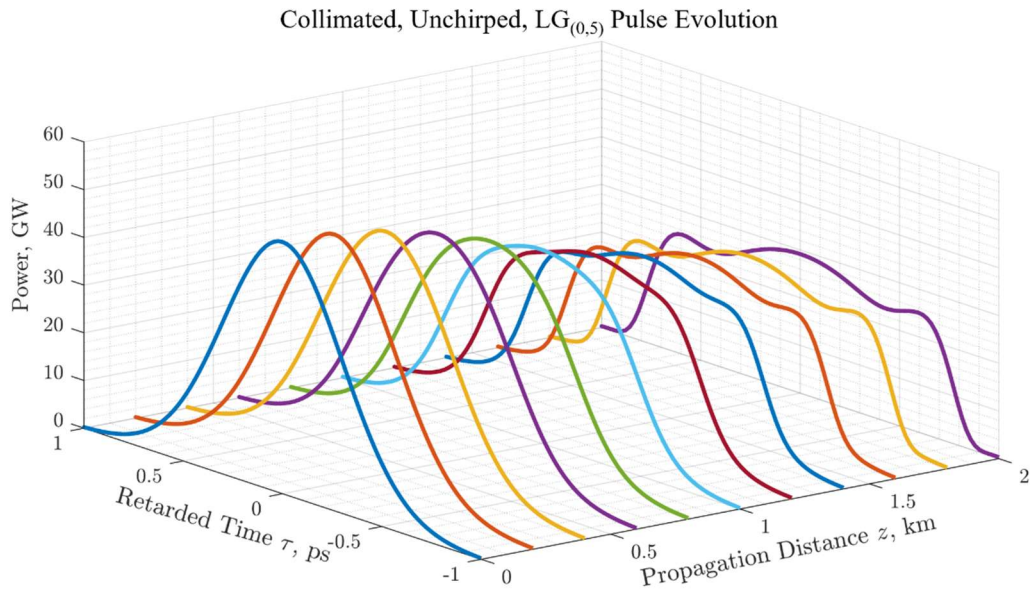


Figure 3.4: Evolution of the temporal profile for a short, high-peak-power OAM pulse. The pulse initially has a (0,5) LG mode transverse profile, Gaussian temporal profile, and $1.10\times P_{\mathrm{cr}}^{(0,5)}$ peak power. Remaining parameters are the same as for Fig. 3.2. Pulse splitting can be observed, breaking the self-similar evolution assumption used for our analytic theory.

3.6 Dynamics of Short, High Power Gaussian Pulses in Turbulence

Now we insert turbulence into our model for the spot size and pulse length of OAM pulses, including SPM and GVD, Eq. (3.5.5).

3.6.1 Analytic Expression for the Spot Size and Pulse Length

In an analysis performed by Hafizi *et al.* [32], it was shown that the effects of turbulence on the RMS spot size W for a CW Gaussian beam can be cast as a beam-quality factor M_T^2,

$$W(z)=w(0)\sqrt{\left(1-\frac{z}{f(0)}\right)^2+\left(1+M_T^4(z)\right)\left(\frac{2z}{k_0 w^2(0)}\right)^2}. \qquad (3.6.1)$$

The values for M_T^2 are split into weak and strong turbulence cases,

$$M_T^4(z)=\begin{cases}0.69k_0^{12/5}w_0^2C_n^{12/5}z^{6/5}/n_0^2, & k_0^2C_n^2\ell_0^{5/3}z\ll 1\\ 1.1k_0^2w_0^2C_n^2z/\ell_0^{1/3}n_0^2, & k_0^2C_n^2\ell_0^{5/3}z\gg 1\end{cases}. \tag{3.6.2}$$

Transforming to the retarded time reference frame and taking the second derivative of Eq. (3.6.1) with respect to η yields,

$$\frac{\partial^2 w(\eta)}{\partial\eta^2}=\frac{4}{k_0^2w^3(\eta)}\tilde{M}_T^4(\eta), \tag{3.6.3}$$

where

$$\begin{aligned}\tilde{M}_T^4(\eta)=&\left(1+M_T^4(\eta)\right)\left[1+\frac{2\eta^3}{k_0^2w^4(0)}\left(2M_T^{4\prime}(\eta)+\eta M_T^{4\prime\prime}(\eta)\right)\right]\\&+\eta\left(1-\frac{\eta}{f(0)}\right)\left(2-\frac{\eta}{f(0)}\right)M_T^{4\prime}(\eta)\\&-\frac{\eta^4}{k_0^2w^4(0)}\left(M_T^{4\prime}(\eta)\right)^2+\frac{\eta^2}{2}\left(1-\frac{\eta}{f(0)}\right)^2M_T^{4\prime\prime}(\eta)\end{aligned} \tag{3.6.4}$$

and the primes indicate derivatives with respect to η. Note that $\tilde{M}_T^4(\eta)=1$ when $C_n^2=0$. Observing the similar forms of Eqs. (3.5.5) and (3.6.3), we merge them to yield[1]

$$\begin{aligned}\partial_\eta^2 w(\eta)&=\frac{4}{k_0^2w^3(\eta)}\left[\tilde{M}_T^4-\gamma k_0\frac{E_0}{\sigma(\eta)}\right],\quad \partial_\eta w(0)=\frac{-2\alpha(0)}{k_0w(0)}\\ \partial_\eta^2\sigma(\eta)&=\frac{4k_2^2}{\sigma^3(\eta)}\left[1+(|m|+1)\frac{\gamma}{k_2}\frac{E_0\sigma(\eta)}{w^2(\eta)}\right],\quad \partial_\eta\sigma(0)=\frac{2k_2C(0)}{\sigma(0)}\end{aligned} \tag{3.6.5}$$

[1] While Eqn. (3.6.5) is presented as an analytic description for LG modes undergoing the effects of Kerr focusing, GVD, and turbulence, we emphasize that we only find it to be reasonably accurate for Gaussian beams – i.e. when the initial transverse profile is in the (0,0) LG mode.

where, again, $\gamma = 3\Gamma\left(|m|+1/2\right)k_0\chi^{(3)}\big/8\pi^2\,\Gamma\left(|m|+2\right)n_0^3\varepsilon_0 c$ is a nonlinear coupling term and $E_0 = \pi^{3/2}n_0\varepsilon_0 c\Gamma\left(|m|+1\right)\left|B_{(0,m,0)}(0)\right|^2 w^2(0)\sigma(0)\big/2^{5/2}$ is the conserved pulse energy.

3.6.2 Comparison to Simulations

We first test Eqn. (3.6.5) for a Gaussian pulse. We consider two configurations: collimated pulses with various chirps shown in Fig. 3.5, and focused unchirped pulses shown in Fig. 3.6. Some of the simulation parameters are given in Table 1. The pulses have peak powers of $2.1\times P_{\rm cr}^{(0,0)}$ and $4.8\times P_{\rm cr}^{(0,0)}$ for the collimated and focused cases, respectively. The pulses initially have carrier wavelengths λ = 875 nm, the propagation medium is air, the turbulence inner and outer scale lengths ℓ_0 = 1 cm and L_0 = 40 m, and the turbulence structure constant $C_n^2 =$ 1×10^{-14}, 5×10^{-14}, and 1×10^{-13} $\mathrm{m}^{-2/3}$ to cover weak to strong turbulence ($\sigma_R^2 \simeq$ 0.4, 2, and 4, respectively).

Table 1: Select parameters for testing Gaussian beam dynamics under SPM, GVD, and turbulence.

Simulation Regimes	$w(0)$, cm	$\sigma(0)$, fs	$C(0)$	$\sigma_R^2(1\mathrm{km})$	P_0, GW	Figure
Collimated, Weak Turb.	3.5	400	–2	0.4	5.1	Figure 3.5
Collimated, Mod. Turb.	3.5	400	–1	2.0	5.1	
Collimated, Strong Turb.	3.5	400	0	4.0	5.1	
Focused, Weak Turb.	5.0	250	0	0.4	11.5	Figure 3.6
Focused, Mod. Turb.	5.0	250	0	2.0	11.5	
Focused, Strong Turb.	5.0	250	0	4.0	11.5	

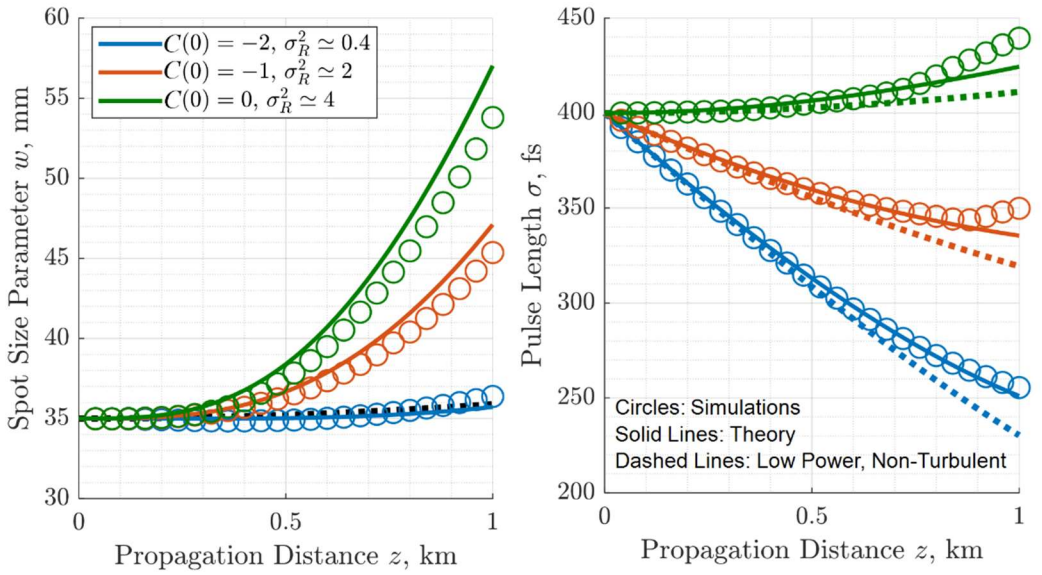


Figure 3.5: Comparison between simulations (circles) and Eq. (3.6.5) (lines) for the ensemble average spot size and pulse length parameters of short, collimated, chirped, high-peak-power Gaussian pulses in turbulence. The initial peak powers are $P_0 = 2.1 \times P_{\mathrm{cr}}^{(0,0)} = 5.1$ GW. The dotted lines correspond to low power (linear), nonturbulent propagation. Note that the low power spot size evolution is the same for all three cases.

We find that the spot size matches the theories well for all configurations tested, except near and past the beam waist minimum for the focused, weak turbulence case. As is expected, the final spot size increases with increasing turbulence; and for the focused beams, the waist minimum is increased and pushed earlier. The pulse lengths for the collimated, chirped cases are accurately predicted; but the theory and simulations deviate for the focused, unchirped cases beyond the beam waists. These errors are attributed to pulse splitting that begins near the beam waists, which breaks the self-similar evolution assumption.

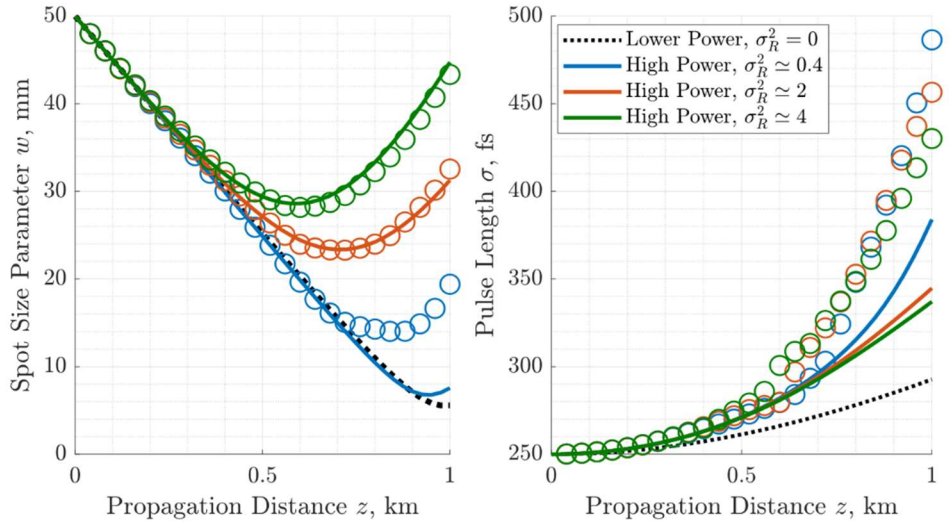


Figure 3.6: Comparison between simulations (circles) and Eq. (3.6.5) (lines) for the ensemble average spot size and pulse length parameters of short, focused, unchirped, high-peak-power Gaussian pulses in turbulence. The initial peak powers are $P_0 = 4.8 \times P_{\mathrm{cr}}^{(0,0)} = 11.5\,\mathrm{GW}$. The dotted lines correspond to low power (linear), nonturbulent propagation.

3.6.3 Comparison to Experiment

The theory is also compared to the experimental results obtained by Helle *et al* [26]. The spot size W at the end of the 825 m propagation channel is plotted as a function of turbulence strength, represented by scintillation index, in Fig. 3.7. The pulses have carrier wavelength λ = 800 nm, spot size w = 5 mm, pulse length σ = 2 ps, and peak power $P_0 = P_{\mathrm{cr}}^{(0,0)} \simeq 2.4$ GW. The pulses are initially collimated and are chirped with β = –100 to counteract dispersion and maintain a critical power at the center of the pulse. The turbulence has inner and outer scale lengths ℓ_0 = 2 cm and L_0 = 1.5 m and structure constant C_n^2 = 1.8×10^{-14} to 1.4×10^{-12} $\mathrm{m}^{-2/3}$.

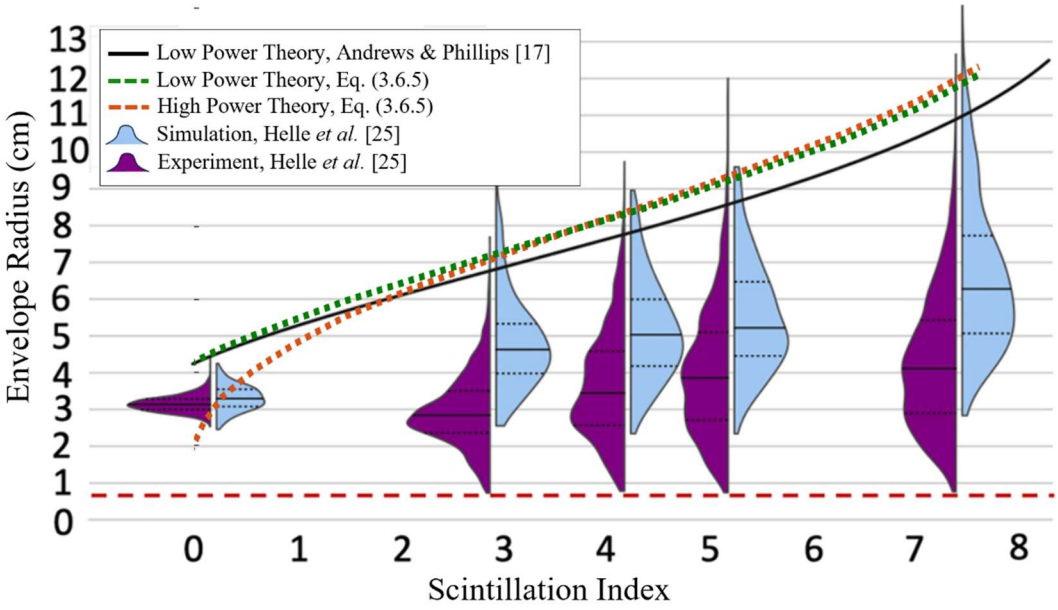


Figure 3.7: The RMS spot size for a Gaussian beam in turbulence. The distributions are experimental and numerical simulation results. The black curve is the low power CW theory from Andrews and Phillips [17]. The red dashed line is our theory, and the green dashed line is also our theory but in the low power CW limit. Part of this figure is reproduced from Ref. [25] with the permission of M. Helle.

The red dashed curve represents the theory Eq. (3.6.5), while the distributions are experimental and simulation values. We find that while the theory is accurate for the weak turbulence case ($\sigma_I^2 \simeq 0.25$), it is inaccurate beyond that. This behavior matches other testing against simulations when the initial spot size is smaller than the turbulence inner scale length, $w(0) < \ell_0$. For comparison, Figure 3.7 also shows the theoretical behavior for low power beams; black represents an expression from Andrews and Phillips [18], whereas the dashed green is Eq. (3.6.5) for low power.

3.7 Mitigating Optical Turbulence With Kerr Focusing for OAM Light

The theory Eq. (3.6.5) was also tested for pulses carrying OAM – principally the (0,1) LG mode. When the initial RMS spot size was greater than the turbulence inner scale length, $W(0) > \ell_0$, simulations would often result in beam collapse. Recall that the critical powers for CW Gaussian and (0,1) LG beams are related via $P_{\mathrm{cr}}^{(0,1)} = 4\,P_{\mathrm{cr}}^{(0,0)}$; thus the turbulence-induced scintillations would readily produce filaments. When $W(0) < \ell_0$, while the beams would collapse less often, the theory was still not accurate. Regardless, there is significant insight to be gained from the simulation results themselves. In this section, we study such simulations in detail to observe how self-focusing to maintain a small spot size in atmospheric turbulence affects OAM light.

We performed pulse propagation simulations in air ($n_0 = 1$, $k_2 = 19$ fs^2/m, $\chi^{(3)} = 1.7\times10^{-25}$ m^2/V^2), and turbulence with an MVK spectrum with $C_n^2 = 7.5\times10^{-14}$ m$^{-2/3}$, $\ell_0 = 3$ cm, and $L_0 = 20$ m. The propagation distance is 500 m, and thus $\sigma_R^2(500\,\mathrm{m}) \approx 0.8$ and corresponds to moderate turbulence. Three input pulse configurations were used: a low-power baseline case with RMS spot size 4.5 cm ($W(0) > \ell_0$); another low-power case but with RMS spot size 1.5 cm ($W(0) < \ell_0$); and a high power case with peak power $P_0 = P_{\mathrm{cr}}^{(0,1)} = 4\times P_{\mathrm{cr}}^{(0,0)} = 9.6\,\mathrm{GW}$ and RMS spot size 1.5 cm ($W(0) < \ell_0$). For each configuration the pulses initially have a (0,1) LG transverse mode profile and a Gaussian temporal profile, carrier wavelength $\lambda = 875$ nm, and pulse length $\sigma(0) = 250$ ps.

One caveat of our simulation routine is that it lacks any high intensity defocusing effects such as multi-photon ionization or plasma defocusing. While this is not a concern for the lower-power cases, the high-power case does occasionally break down: turbulence-induced scintillations can cause collapsing parts of the beam which grow beyond the resolution of the discrete sampling grid. Simulations that result in such singularities can be readily identified by tracking the energy in the pulse throughout the simulation. Due to how the propagation procedure handles boundary conditions at the aperture edges, cases that numerically collapse lead to a significant, non-physical loss of energy. By discarding simulations that do not conserve energy, we can only consider cases where the beam does not undergo collapse. This procedure led to 28% (445/1600) of the high-power test cases being discarded.

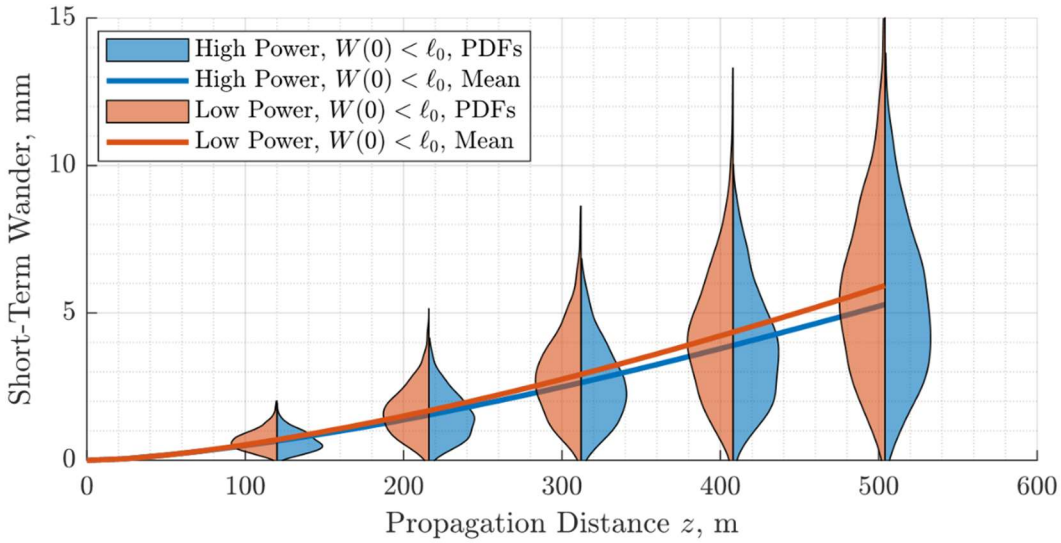


Figure 3.8: Probability distributions and ensemble averages of the short-term centroid wander for high- and low-power OAM pulses in MVK turbulence, with initial RMS spot size $W(0)$ smaller than the turbulence inner scale length ℓ_0. The two cases largely behave similarly, which is consistent with the Gaussian pulse results presented by Helle *et al*. [25].

First, we consider the beam centroid wander shown in Fig. 3.8. The filled areas show the evolution of the probability distributions for the centroid wander for the $W(0) < \ell_0$ configurations, blue for high-power and red for low-power. The solid lines trace out the ensemble average values. Since centroid wander is largely dictated by turbulent eddies with scale sizes larger than the instantaneous spot size, it is not surprising that the high- and low-power results are so similar. This behavior is consistent with the Gaussian case observed by Helle *et al.* [26].

The evolution of the short-term hot-spot size is shown in Fig. 3.9. The hot-spot is defined as the portion of the pulse that remains after applying a 50% intensity threshold; that is, only parts of the pulse that have intensities above half the peak intensity are used. This technique limits the impacts of the sub-critical

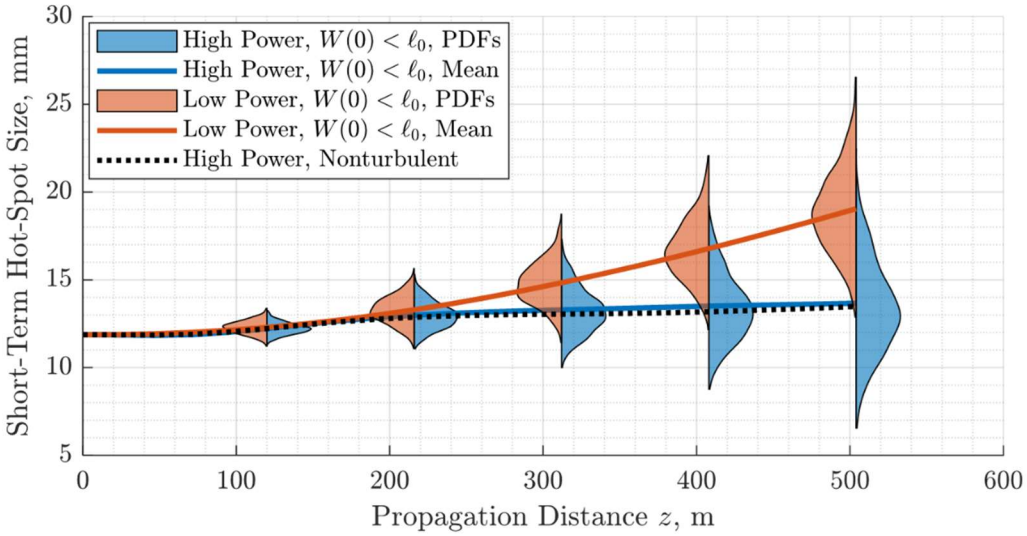


Figure 3.9: Probability distributions and ensemble averages of the short-term hot-spot sizes for high- and low-power OAM pulses in MVK turbulence, with initial RMS spot size $W(0)$ smaller than the turbulence inner scale length ℓ_0. The self-focused pulses maintain a much higher power density, which is consistent with the Gaussian pulse results presented by Helle *et al*. [25].

"tails" of the pulse (front and back), which will largely evolve equivalently to the low-power cases. We can see that the self-focused beam suffers much less from short-term beam spreading compared to the low-power case. In fact, the ensemble average very nearly matches the non-turbulent propagation case.

Finally, we consider the OAM mode makeup of the pulse as it propagates. The weights of the input (0,1) LG mode over propagation distance for the three cases are shown in Fig. 3.10. We can observe that the two configurations that start with RMS spot sizes smaller than the inner scale length, $W(0) < \ell_0$, remain in the (0,1) LG state much longer than the low power, $W(0) > \ell_0$ case. Between the two $W(0) < \ell_0$ cases, the self-focused case does perform better, but only slightly. This

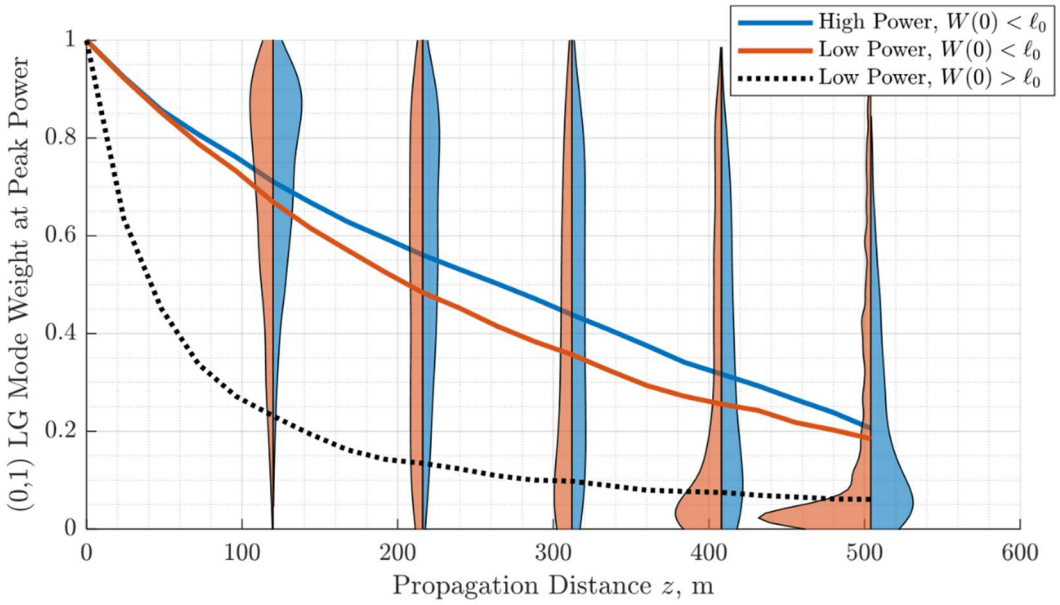


Figure 3.10: Probability distributions and ensemble averages of the (0,1) mode weight of the peak-power segment for high- and low-power OAM pulses in MVK turbulence. The cases with initial RMS spot size $W(0)$ smaller than the turbulence inner scale length ℓ_0, both high- and low-power, stay in the (0,1) mode much longer than the $W(0) > \ell_0$.

is somewhat surprising given the comparatively clear difference in RMS hot-spot size. Though we do note that the Rayleigh length for our test configuration is $z_R \simeq 400$ m, and thus the diffraction-based RMS spot size for the $W(0) < \ell_0$ cases will be ~2.4 cm at 500 m, which is still less than ℓ_0 (3 cm). A simulation regime that involves propagation over multiple Rayleigh lengths, such that the diffractive spot size grows beyond the inner scale length, would be highly desirable. Unfortunately we were unable to perform such simulations to our satisfaction due to excessive beam collapse.

3.8 Conclusions

In this chapter, we extended our study of OAM beams in turbulence to include the effects of self-phase modulation and dispersion:

- We derived and tested dynamics equations that describe the spot size and pulse length of high-power OAM pulses under the effects of SPM and GVD.
- We extended this model to include turbulence. It compared well against simulations for Gaussian pulses when $w(0) > \ell_0$. Comparison to experimental results and simulations for $w(0) < \ell_0$ indicated it was only accurate for weak turbulence. It did not prove accurate for LG pulses in any configuration.
- Nevertheless, we did find that Kerr focusing can reduce the short-term beam spreading and OAM mode mixing caused by turbulence, at the expense of occasional filamentation.

This concludes our investigation of OAM light in turbulence. We now change our focus: rather than see how OAM beams decay in turbulence, we now consider how we can generate OAM beams in the first place.

Chapter 4 High-Power Orbital Angular Momentum Beams in Waveguides

4.1 Chapter Overview

Chapters 2 and 3 discussed OAM propagating in bulk media. Now we investigate the nonlinear interactions of OAM beams in waveguides. In such waveguides the OAM modes are vector modes. That is, we cannot define a scalar mode profile F_q and assign an arbitrary polarization to it as before. Rather, the mode profile is a vector quantity $\mathbf{F}_q$. In addition, for bulk propagation, all modes have the same dispersion characteristics dictated by $k(\omega)$. In waveguides each mode can have a unique propagation constant, typically denoted $\beta_q(\omega)$. We will find that these features result in certain rules regarding which modes can interact with each other in nonlinear processes – specifically, selection rules for parametric amplification of new modes. A typical experimental configuration for observing processes was depicted in Fig. 1.4.

This chapter is organized as follows. First, in section 4.2, we give a brief overview of so-called Spin-Orbit (SO) that exist in azimuthally symmetric fibers. In section 4.3 we use the Multimode Generalized Nonlinear Schrödinger's Wave Equation (MM-GNLSE) to derive selection rules and growth rates for the generation of new SO modes via four-wave mixing (FWM). We test these results by comparing the predictions to simulations for the cases where the generated signals are in the same SO mode(s) as the pump(s) in section 4.4. Finally, in section 4.5, we consider signals generated in SO modes different from the pump(s).

4.2 Spin-Orbit Modes in Waveguides

We limit our analysis to waveguides which have the properties: no free charges or current, nonmagnetic media, and a *z*-independent and azimuthally symmetric permittivity $\varepsilon_r^{(1)}(r)$. A generic refractive index profile $n(r)$ for such a fiber is depicted in Figure 4.1. The modes of the fiber satisfy the linear vector wave equations for the electric and magnetic fields, which can be derived from Maxwell's equations:

$$\begin{aligned}\left(\nabla^2+\frac{\varepsilon_0^{(1)}(r)\omega^2}{c^2}\right)\tilde{\mathbf{E}}(\mathbf{r},\omega)+\nabla\left(\tilde{\mathbf{E}}(\mathbf{r},\omega)\cdot\nabla_\perp\log\varepsilon_0^{(1)}(r)\right)=0,\\ \left(\nabla^2+\frac{\varepsilon_0^{(1)}(r)\omega^2}{c^2}\right)\tilde{\mathbf{H}}(\mathbf{r},\omega)-\left(\nabla\times\tilde{\mathbf{H}}(\mathbf{r},\omega)\right)\times\nabla_\perp\log\varepsilon_0^{(1)}(r)=0.\end{aligned} \tag{4.2.1}$$

The modes also satisfy the boundary conditions

$$\begin{aligned}\hat{\mathbf{n}}_{12}\times(\mathbf{E}_2-\mathbf{E}_1)=0,\\ \hat{\mathbf{n}}_{12}\cdot(\mathbf{D}_2-\mathbf{D}_1)=0,\\ \mathbf{H}_2-\mathbf{H}_1=0,\end{aligned} \tag{4.2.2}$$

where $\hat{\mathbf{n}}_{12}$ is the unit vector pointing from medium 1 to medium 2 [1] [33]. Unlike the atmospheric case, for waveguides we do not make the approximation $\nabla_\perp\log\varepsilon_0^{(1)}(r)\simeq 0$. We write the q mode in the form

$$\begin{aligned}\tilde{\mathbf{E}}_q(\mathbf{r},\omega)=\frac{\tilde{\mathbf{F}}_q(\mathbf{r}_\perp,\omega)}{N_q(\omega)}\exp\left[i\beta_q(\omega)z\right],\\ \tilde{\mathbf{H}}_q(\mathbf{r},\omega)=\frac{\tilde{\mathbf{G}}_q(\mathbf{r}_\perp,\omega)}{N_q(\omega)}\exp\left[i\beta_q(\omega)z\right],\end{aligned} \tag{4.2.3}$$

where $\tilde{\mathbf{F}}_q$ and $\tilde{\mathbf{G}}_q$ are the z-invariant field profiles, β_q is the propagation constant, and N is a normalization and mode orthogonality relationship given by

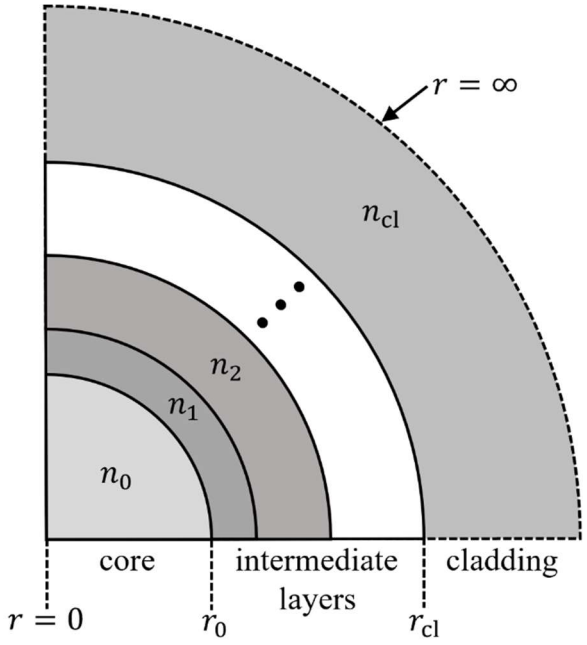


Figure 4.1: A generic refractive index profile for an azimuthally symmetric fiber, which supports SO modes. Analytically, the cladding is often taken to extend to infinity. The *z*-axis points in or out of the page.

$$4\delta_{q,q'}N_q^2(\omega) = \int d^2r\ \hat{\mathbf{z}}\cdot\left(\tilde{\mathbf{F}}_q(\mathbf{r}_\perp,\omega)\times\tilde{\mathbf{G}}_{q'}^*(\mathbf{r}_\perp,\omega) - \tilde{\mathbf{G}}_q(\mathbf{r}_\perp,\omega)\times\tilde{\mathbf{F}}_{q'}^*(\mathbf{r}_\perp,\omega)\right). \tag{4.2.4}$$

The calculation of the modes, i.e. $\tilde{\mathbf{F}}_q(\mathbf{r}_\perp,\omega)$, $\tilde{\mathbf{G}}_q(\mathbf{r}_\perp,\omega)$, and $\beta_q(\omega)$, typically requires numerical methods for all but the simplest waveguide profiles. In this dissertation we utilize the transfer matrix method [34] [35] which is well-posed for azimuthally symmetric waveguides. While we did construct our own mode solving program, open-source libraries are available; in particular, the author recommends the resources provided by Hammond [36].

Skipping to the salient features of the modes, it can be shown that the electric and magnetic field mode profiles have the forms

$$\begin{aligned}\tilde{\mathbf{F}}_q(\mathbf{r}_\perp,\omega) &= \left[\hat{\mathbf{r}}\,\tilde{F}_q^r(r,\omega)+\hat{\boldsymbol{\varphi}}\tilde{F}_q^\phi(r,\omega)+\hat{\mathbf{z}}\,\tilde{F}_q^z(r,\omega)\right]\exp\left[iJ\varphi\right],\\ \tilde{\mathbf{G}}_q(\mathbf{r}_\perp,\omega) &= \left[\hat{\mathbf{r}}\,\tilde{G}_q^r(r,\omega)+\hat{\boldsymbol{\varphi}}\tilde{G}_q^\phi(r,\omega)+\hat{\mathbf{z}}\,\tilde{G}_q^z(r,\omega)\right]\exp\left[iJ\varphi\right].\end{aligned} \tag{4.2.5}$$

J denotes the total angular momentum (TAM). That is, each photon in the mode carries $J\hbar\hat{\mathbf{z}}$ angular momentum. An equivalent representation of the mode profiles is produced by transforming to the circular polarization basis, e.g.

$$\begin{aligned}\tilde{\mathbf{F}}_q(\mathbf{r}_\perp,\omega) &= \hat{\boldsymbol{\sigma}}_+\,\tilde{F}_q^+(r,\omega)\exp\left[i\left(J-1\right)\varphi\right]\\ &\quad+\hat{\boldsymbol{\sigma}}_-\,\tilde{F}_q^-(r,\omega)\exp\left[i\left(J+1\right)\varphi\right]\\ &\quad+\hat{\mathbf{z}}\,\tilde{F}_q^z(r,\omega)\exp\left[iJ\varphi\right],\\ \tilde{\mathbf{G}}_q(\mathbf{r}_\perp,\omega) &= \hat{\boldsymbol{\sigma}}_+\,\tilde{G}_q^+(r,\omega)\exp\left[i\left(J-1\right)\varphi\right]\\ &\quad+\hat{\boldsymbol{\sigma}}_-\,\tilde{G}_q^-(r,\omega)\exp\left[i\left(J+1\right)\varphi\right]\\ &\quad+\hat{\mathbf{z}}\,\tilde{G}_q^z(r,\omega)\exp\left[iJ\varphi\right],\end{aligned} \tag{4.2.6}$$

where $\hat{\boldsymbol{\sigma}}_+=\hat{\mathbf{x}}+i\hat{\mathbf{y}}$ denotes LCP and $\hat{\boldsymbol{\sigma}}_-=\hat{\mathbf{x}}-i\hat{\mathbf{y}}$ denotes RCP [37] [38]. Transverse electric (TE) modes correspond to J = 0, $\tilde{F}_q^-=-\tilde{F}_q^+$, $\tilde{F}_q^z=0$, and $\tilde{G}_q^-=\tilde{G}_q^+$, and can be written as

$$\begin{aligned}\tilde{\mathbf{F}}_{(p,\mathrm{TE})}(\mathbf{r}_\perp,\omega) &= \tilde{F}_{(p,\mathrm{TE})}^\perp(r,\omega)\left(\hat{\boldsymbol{\sigma}}_+\exp\left[-i\varphi\right]-\hat{\boldsymbol{\sigma}}_-\exp\left[i\varphi\right]\right),\\ \tilde{\mathbf{G}}_{(p,\mathrm{TE})}(\mathbf{r}_\perp,\omega) &= \tilde{G}_{(p,\mathrm{TE})}^\perp(r,\omega)\left(\hat{\boldsymbol{\sigma}}_+\exp\left[-i\varphi\right]+\hat{\boldsymbol{\sigma}}_-\exp\left[i\varphi\right]\right)+\hat{\mathbf{z}}\,\tilde{G}_{(p,\mathrm{TE})}^z(r,\omega),\end{aligned} \tag{4.2.7}$$

where p is the radial order of the mode. In other words, $\tilde{F}_{(p,\mathrm{TE})}^\perp$ and $\tilde{G}_{(p,\mathrm{TE})}^\perp$ have p zero-crossings in r. In a similar fashion, transverse magnetic (TM) modes have $J=0$, $\tilde{F}_q^+=\tilde{F}_q^-$, $\tilde{G}_q^+=-\tilde{G}_q^-$, and $\tilde{G}_q^z=0$, and take the form

$$\begin{aligned}\tilde{\mathbf{F}}_{(p,\mathrm{TM})}(\mathbf{r}_\perp,\omega) &= \tilde{F}_{(p,\mathrm{TM})}^\perp(r,\omega)\left(\hat{\boldsymbol{\sigma}}_+\exp\left[-i\varphi\right]+\hat{\boldsymbol{\sigma}}_-\exp\left[i\varphi\right]\right)+\hat{\mathbf{z}}\,\tilde{F}_{(p,\mathrm{TM})}^z(r,\omega),\\ \tilde{\mathbf{G}}_{(p,\mathrm{TM})}(\mathbf{r}_\perp,\omega) &= \tilde{G}_{(p,\mathrm{TM})}^\perp(r,\omega)\left(\hat{\boldsymbol{\sigma}}_+\exp\left[-i\varphi\right]-\hat{\boldsymbol{\sigma}}_-\exp\left[i\varphi\right]\right).\end{aligned} \tag{4.2.8}$$

Since TE and TM modes both have J = 0, they do not carry a net TAM. The modes that do carry a net TAM will not have any vanishing components; in

addition, one spin component will be dominant in the sense that, e.g., $\int d^2r\left|\tilde{F}_q^{\pm}\right|^2 > \int d^2r\left|\tilde{F}_q^{\mp}\right|^2$. It is common to express such spatial modes in terms of the OAM quanta m carried by the dominant spin component rather than J, e.g. for a LCP-dominant mode

$$\begin{aligned}
\tilde{\mathbf{F}}_{(p,+,m)}(\mathbf{r}_\perp,\omega) &= \hat{\boldsymbol{\sigma}}_+ \tilde{F}^+_{(p,+,m)}(r,\omega)\exp[im\varphi] \\
&\quad + \hat{\boldsymbol{\sigma}}_- \tilde{F}^-_{(p,+,m)}(r,\omega)\exp\left[i(m+2)\varphi\right] \\
&\quad + \hat{\mathbf{z}}\ \tilde{F}^z_{(p,+,m)}(r,\omega)\exp\left[i(m+1)\varphi\right], \\
\tilde{\mathbf{G}}_{(p,+,m)}(\mathbf{r}_\perp,\omega) &= \hat{\boldsymbol{\sigma}}_+ \tilde{G}^+_{(p,+,m)}(r,\omega)\exp[im\varphi] \\
&\quad + \hat{\boldsymbol{\sigma}}_- \tilde{G}^-_{(p,+,m)}(r,\omega)\exp\left[i(m+2)\varphi\right] \\
&\quad + \hat{\mathbf{z}}\ \tilde{G}^z_{(p,+,m)}(r,\omega)\exp\left[i(m+1)\varphi\right],
\end{aligned} \tag{4.2.9}$$

where $m = J - 1$. Similarly, for a RCP-dominant mode,

$$\begin{aligned}
\tilde{\mathbf{F}}_{(p,-,m)}(\mathbf{r}_\perp,\omega) &= \hat{\boldsymbol{\sigma}}_+ \tilde{F}^+_{(p,-,m)}(r,\omega)\exp\left[i(m-2)\varphi\right] \\
&\quad + \hat{\boldsymbol{\sigma}}_- \tilde{F}^-_{(p,-,m)}(r,\omega)\exp[im\varphi] \\
&\quad + \hat{\mathbf{z}}\ \tilde{F}^z_{(p,-,m)}(r,\omega)\exp\left[i(m-1)\varphi\right], \\
\tilde{\mathbf{G}}_{(p,-,m)}(\mathbf{r}_\perp,\omega) &= \hat{\boldsymbol{\sigma}}_+ \tilde{G}^+_{(p,-,m)}(r,\omega)\exp\left[i(m-2)\varphi\right] \\
&\quad + \hat{\boldsymbol{\sigma}}_- \tilde{G}^-_{(p,-,m)}(r,\omega)\exp[im\varphi] \\
&\quad + \hat{\mathbf{z}}\ \tilde{G}^z_{(p,-,m)}(r,\omega)\exp\left[i(m-1)\varphi\right],
\end{aligned} \tag{4.2.10}$$

where $m = J + 1$. In either case, the TAM for the $(p,\pm,m)$ mode can be recovered via $J = s + m$, where $s = +1$ for LCP-dominant modes and $s = -1$ for RCP-dominant modes.

Depending on the design of the waveguide and the values of m under consideration, the "recessive" spin and longitudinal components of the modes may be sufficiently small such that an approximate representation, e.g. $\tilde{\mathbf{F}}_{(p,\pm,m)}(\mathbf{r}_\perp,\omega) \simeq \hat{\boldsymbol{\sigma}}_\pm F_{(p,\pm,m)}(r,\omega)\exp[im\varphi]$ is well justified. However, this is not

generally valid, and there are important ramifications regarding selection rules for FWM processes that we consider.

4.3 Four-Wave Mixing of Spin-Orbit Modes: Theory

We now consider how these SO modes interact in FWM processes. The derivation of the governing equations is based on the generalized multimode nonlinear Schrödinger equation MM-GNLSE as described by Poletti and Horak [39]. Take the electric and magnetic fields inside the fiber as the sum of spatial modes q, each at a frequency ω_q which are in the vicinity of a common carrier frequency ω_0,

$$\begin{aligned}\mathbf{E}(\mathbf{r},t) &= \sum_q A_q(z)\frac{\tilde{\mathbf{F}}_q(\mathbf{r}_\perp,\omega_0)}{N_q(\omega_0)}\exp\left[i\left(\beta_q(\omega_q)z-\omega_q t\right)\right],\\ \mathbf{H}(\mathbf{r},t) &= \sum_q A_q(z)\frac{\tilde{\mathbf{G}}_q(\mathbf{r}_\perp,\omega_0)}{N_q(\omega_0)}\exp\left[i\left(\beta_q(\omega_q)z-\omega_q t\right)\right],\end{aligned} \tag{4.3.1}$$

where $\left|\omega_0-\omega_q\right| \ll \omega_0$, $\omega_q > 0$, and A_q is the longitudinal envelope. Note that, by requiring the envelopes to have the form $A_q(z)$, we are assuming continuous wave (CW) signals; we will lift this assumption later to allow for temporal variations in the envelopes. Proceeding with the standard derivation of the MM-GNLSE [38] [39] we arrive at

$$\partial_z A_q(z) = \frac{-1}{4N_q(\omega_0)}\exp\left[-i\left(\beta_q(\omega_q)z-\omega_q t\right)\right]\int d^2r\ \tilde{\mathbf{F}}_q^*(\omega_0)\cdot\partial_t\mathbf{P}_{\mathrm{NL}}(\mathbf{r},t). \tag{4.3.2}$$

In this chapter, we are concerned with FWM processes driven by the instantaneous third-order nonlinear susceptibility. Thus the nonlinear polarization $\mathbf{P}_{\mathrm{NL}}$ is given by

$$\mathbf{P}_{\mathrm{NL}} = \frac{\varepsilon_0 \chi^{(3)}}{4}\left[2\left|\mathbf{E}\right|^2 \mathbf{E} + \left(\mathbf{E}\cdot\mathbf{E}\right)\mathbf{E}^*\right]\exp\left[-i\omega_0 t\right], \tag{4.3.3}$$

where, just as in the free-space case, we have discarded the third-harmonic term. We consider the case where the fields are composed of two pumps, labeled as modes 1 and 2, and an arbitrary collection of smaller amplitude signals S. Expanding Eq. (4.3.3), inserting it into Eq. (4.3.2), and assuming $\beta_1(\omega_1) \neq \beta_2(\omega_2)$, the leading order terms for modes 1 and 2 are

$$\begin{aligned} \partial_z A_1 &= i\alpha_1\left[Q_1^{(\mathrm{SPM})}\left|A_1\right|^2 + Q_{1,2}^{(\mathrm{XPM})}\left|A_2\right|^2\right]A_1, \\ \partial_z A_2 &= i\alpha_2\left[Q_{2,1}^{(\mathrm{XPM})}\left|A_1\right|^2 + Q_2^{(\mathrm{SPM})}\left|A_2\right|^2\right]A_2. \end{aligned} \tag{4.3.4}$$

where $\alpha_q = \varepsilon_0\chi^{(3)}\omega_q/8$ and the Q terms are overlap integrals for self-phase modulation (SPM) and cross-phase modulation (XPM) processes,

$$\begin{aligned} Q_q^{(\mathrm{SPM})} &= \frac{1}{N_q^4}\int d^2r\left[\left|\tilde{\mathbf{F}}_q\right|^4 + \frac{1}{2}\left(\tilde{\mathbf{F}}_q\cdot\tilde{\mathbf{F}}_q\right)\left(\tilde{\mathbf{F}}_q^*\cdot\tilde{\mathbf{F}}_q^*\right)\right], \\ Q_{q,j}^{(\mathrm{XPM})} &= \frac{1}{N_q^2 N_j^2}\int d^2r\left[\left|\tilde{\mathbf{F}}_q\right|^2\left|\tilde{\mathbf{F}}_j\right|^2 + \left(\tilde{\mathbf{F}}_q\cdot\tilde{\mathbf{F}}_j\right)\left(\tilde{\mathbf{F}}_q^*\cdot\tilde{\mathbf{F}}_j^*\right) + \left(\tilde{\mathbf{F}}_q^*\cdot\tilde{\mathbf{F}}_j\right)\left(\tilde{\mathbf{F}}_q\cdot\tilde{\mathbf{F}}_j^*\right)\right]. \end{aligned} \tag{4.3.5}$$

Since $Q_q^{(\mathrm{SPM})}$ and $Q_{q,j}^{(\mathrm{XPM})}$ are real-valued, $|A_1(z)|^2$ and $|A_2(z)|^2$ are z-invariant and Eqs. (4.3.4) can be solved directly even though they form a coupled nonlinear system. The equation for an arbitrary signal S, to leading order, will include cross phase modulation by the two pumps and numerous other nonlinear terms. If we only consider signals that can undergo amplification, even from noise, one obtains

$$\begin{aligned} \partial_z A_{\mathrm{S}} = i\alpha_{\mathrm{S}}\Big[&\left(Q_{\mathrm{S},1}^{(\mathrm{XPM})}\left|A_1\right|^2 + Q_{\mathrm{S},2}^{(\mathrm{XPM})}\left|A_2\right|^2\right)A_{\mathrm{S}} \\ &+ \sum_{\mathrm{A}} Q_{\mathrm{S,A}}^{(\mathrm{FWM1})} A_1^2 A_{\mathrm{A}}^* \exp\left[i\left(2\beta_1 - \beta_{\mathrm{A}} - \beta_{\mathrm{S}}\right)z\right]\delta\left(2\omega_1 - \omega_{\mathrm{A}} - \omega_{\mathrm{S}}\right) \\ &\quad + Q_{\mathrm{S,A}}^{(\mathrm{FWM2})} A_2^2 A_{\mathrm{A}}^* \exp\left[i\left(2\beta_2 - \beta_{\mathrm{A}} - \beta_{\mathrm{S}}\right)z\right]\delta\left(2\omega_2 - \omega_{\mathrm{A}} - \omega_{\mathrm{S}}\right) \\ &\quad + Q_{\mathrm{S,A}}^{(\mathrm{FWM3})} A_1 A_2 A_{\mathrm{A}}^* \exp\left[i\left(\beta_1 + \beta_2 - \beta_{\mathrm{A}} - \beta_{\mathrm{S}}\right)z\right]\delta\left(\omega_1 + \omega_2 - \omega_{\mathrm{A}} - \omega_{\mathrm{S}}\right)\Big], \end{aligned} \tag{4.3.6}$$

where the mode A is another mode generated along with mode S, and the overlap integrals for the different FWM processes are given by

$$
\begin{aligned}
Q_{\mathrm{S,A}}^{(\mathrm{FWM1})} &= \frac{1}{N_1^2 N_{\mathrm{S}} N_{\mathrm{A}}} \int d^2 r \left[\left(\tilde{\mathbf{F}}_1 \cdot \tilde{\mathbf{F}}_{\mathrm{S}}^* \right) \left(\tilde{\mathbf{F}}_1 \cdot \tilde{\mathbf{F}}_{\mathrm{A}}^* \right) + \frac{1}{2} \left(\tilde{\mathbf{F}}_1 \cdot \tilde{\mathbf{F}}_1 \right) \left(\tilde{\mathbf{F}}_{\mathrm{S}}^* \cdot \tilde{\mathbf{F}}_{\mathrm{A}}^* \right) \right], \\
Q_{\mathrm{S,A}}^{(\mathrm{FWM2})} &= \frac{1}{N_2^2 N_{\mathrm{S}} N_{\mathrm{A}}} \int d^2 r \left[\left(\tilde{\mathbf{F}}_2 \cdot \tilde{\mathbf{F}}_{\mathrm{S}}^* \right) \left(\tilde{\mathbf{F}}_2 \cdot \tilde{\mathbf{F}}_{\mathrm{A}}^* \right) + \frac{1}{2} \left(\tilde{\mathbf{F}}_2 \cdot \tilde{\mathbf{F}}_2 \right) \left(\tilde{\mathbf{F}}_{\mathrm{S}}^* \cdot \tilde{\mathbf{F}}_{\mathrm{A}}^* \right) \right], \\
Q_{\mathrm{S,A}}^{(\mathrm{FWM3})} &= \frac{1}{N_1 N_2 N_{\mathrm{S}} N_{\mathrm{A}}} \int d^2 r \left[\left(\tilde{\mathbf{F}}_1 \cdot \tilde{\mathbf{F}}_{\mathrm{S}}^* \right) \left(\tilde{\mathbf{F}}_2 \cdot \tilde{\mathbf{F}}_{\mathrm{A}}^* \right) + \left(\tilde{\mathbf{F}}_2 \cdot \tilde{\mathbf{F}}_{\mathrm{S}}^* \right) \left(\tilde{\mathbf{F}}_1 \cdot \tilde{\mathbf{F}}_{\mathrm{A}}^* \right) \right. \\
&\qquad \left. + \left(\tilde{\mathbf{F}}_1 \cdot \tilde{\mathbf{F}}_2 \right) \left(\tilde{\mathbf{F}}_{\mathrm{S}}^* \cdot \tilde{\mathbf{F}}_{\mathrm{A}}^* \right) \right].
\end{aligned}
\tag{4.3.7}
$$

With $\omega_{\mathrm{S}} < \omega_{\mathrm{A}}$, S can naturally be identified as the Stokes mode and A the anti-Stokes mode. The governing equation for mode A is obtained by the substitution S $\leftrightarrow$ A. In addition, we can identify FWM1(2) as corresponding to degenerate FWM from pump 1(2), and FWM3 to nondegenerate FWM.

Angular momentum selection rules, which are embedded within the overlap integrals Q, dictate the SO modes that interact via FWM. This is most obvious by considering the forms of the spatial modes provided in Eqs. (4.2.5). For example, the azimuthal integration for $Q_{\mathrm{S,A}}^{(\mathrm{FWM1})}$ is nonzero only if $2J_1 = J_{\mathrm{S}} + J_{\mathrm{A}}$. Similarly, $Q_{\mathrm{S,A}}^{(\mathrm{FWM2})}$ requires $2J_2 = J_{\mathrm{S}} + J_{\mathrm{A}}$, and $Q_{\mathrm{S,A}}^{(\mathrm{FWM3})}$ requires $J_1 + J_2 = J_{\mathrm{S}} + J_{\mathrm{A}}$. Since J quantizes the TAM of the mode, one can say the TAM of the light is conserved during the FWM processes.

When the modes involved in a particular FWM process carry nonzero TAM and have negligibly small recessive spin components such that the approximation $\tilde{\mathbf{F}}_{(p,\pm,m)}(\mathbf{r}_\perp, \omega_0) \simeq \hat{\boldsymbol{\sigma}}_\pm \tilde{F}_{(p,\pm,m)}(r, \omega_0) \exp[im\varphi]$ is accurate, the overlap integrals are nonzero only when OAM and SAM are conserved

independently. For example, in this regime, $Q^{(\mathrm{FWM3})} \neq 0$ only when $m_1 + m_2 = m_\mathrm{S} + m_\mathrm{A}$ and $s_1 + s_2 = s_\mathrm{S} + s_\mathrm{A}$, where $s = +1$ for LCP-dominant modes and $s = -1$ for RCP-dominant modes. This restricted case was observed experimentally by Liu *et al.* [41].

Assuming the frequency matching conditions (delta functions in Eq. (4.3.6)) are satisfied, and that the pumps carry powers P_1 and P_2, one finds that each FWM term can lead to the growth of new SO modes. The growth rates for each FWM process are

$$\begin{aligned}
g^{(\mathrm{FWM1})} &= \sqrt{4\alpha_\mathrm{S}\alpha_\mathrm{A}\, Q_{\mathrm{S,A}}^{(\mathrm{FWM1})2} P_1^2 - \kappa^{(\mathrm{FWM1})2}}\,, \\
\kappa^{(\mathrm{FWM1})} &= 2\beta_1(\omega_1) - \beta_\mathrm{S}(\omega_\mathrm{S}) - \beta_\mathrm{A}(\omega_\mathrm{A}) + 2\theta_1 - \theta_\mathrm{S} - \theta_\mathrm{A}\,, \\
g^{(\mathrm{FWM2})} &= \sqrt{4\alpha_\mathrm{S}\alpha_\mathrm{A}\, Q_{\mathrm{S,A}}^{(\mathrm{FWM2})2} P_2^2 - \kappa^{(\mathrm{FWM2})2}}\,, \\
\kappa^{(\mathrm{FWM2})} &= 2\beta_2(\omega_2) - \beta_\mathrm{S}(\omega_\mathrm{S}) - \beta_\mathrm{A}(\omega_\mathrm{A}) + 2\theta_2 - \theta_\mathrm{S} - \theta_\mathrm{A}\,, \\
g^{(\mathrm{FWM3})} &= \sqrt{4\alpha_\mathrm{S}\alpha_\mathrm{A}\, Q_{\mathrm{S,A}}^{(\mathrm{FWM3})2} P_1 P_2 - \kappa^{(\mathrm{FWM3})2}}\,, \\
\kappa^{(\mathrm{FWM3})} &= \beta_1(\omega_1) + \beta_2(\omega_2) - \beta_\mathrm{S}(\omega_\mathrm{S}) - \beta_\mathrm{A}(\omega_\mathrm{A}) + \theta_1 + \theta_2 - \theta_\mathrm{S} - \theta_\mathrm{A}\,,
\end{aligned} \tag{4.3.8}$$

where each θ is a nonlinear phase shift

$$\begin{aligned}
\theta_1 &= \alpha_1\left(Q_1^{(\mathrm{SPM})} P_1 + Q_{1,2}^{(\mathrm{XPM})} P_2\right), \\
\theta_2 &= \alpha_2\left(Q_{2,1}^{(\mathrm{XPM})} P_1 + Q_2^{(\mathrm{SPM})} P_2\right), \\
\theta_\mathrm{S} &= \alpha_\mathrm{S}\left(Q_{\mathrm{S},1}^{(\mathrm{XPM})} P_1 + Q_{\mathrm{S},2}^{(\mathrm{XPM})} P_2\right), \\
\theta_\mathrm{A} &= \alpha_\mathrm{A}\left(Q_{\mathrm{A},1}^{(\mathrm{XPM})} P_1 + Q_{\mathrm{A},2}^{(\mathrm{XPM})} P_2\right).
\end{aligned} \tag{4.3.9}$$

The growth rate of a particular mode is maximized when the phase matching condition $\kappa = 0$ is satisfied, and larger pump powers will increase the bandwidth over which the mode will grow. For SO modes, further mode selectivity is

achieved by the constraint of conservation of TAM. Note that the growth rates provided are the power e-folding lengths, e.g. $P_S(z)=P_S(0)\exp[gz]$.

4.4 Comparison To Simulations

4.4.1 Simulation Overview

We now wish to validate our results for the growth of new modes. Directly solving Eqs. (4.3.4) and (4.3.6) would require construction of a $N_m \times N_\omega$ system of equations, where N_m is the number of modes and N_ω the number of discrete frequency bins. One can reduce this to a N_m system by allowing the mode envelopes to have a time dependence, i.e. $A_q(z) \rightarrow A_q(z,t)$. Doing so and rederiving Eqs. (4.3.4) and (4.3.6) yields

$$\begin{aligned}\partial_z A_1(z,t) &= \left[\sum_{\nu>0}\frac{i^{\nu+1}}{\nu!}\beta_{\nu,1}\partial_t^\nu + i\alpha_1\left(Q_1^{(\mathrm{SPM})}\left|A_1\right|^2 + Q_{1,2}^{(\mathrm{XPM})}\left|A_2\right|^2\right)\right]A_1,\\ \partial_z A_2(z,t) &= \left[\sum_{\nu>0}\frac{i^{\nu+1}}{\nu!}\beta_{\nu,2}\partial_t^\nu + i\alpha_2\left(Q_{2,1}^{(\mathrm{XPM})}\left|A_1\right|^2 + Q_2^{(\mathrm{SPM})}\left|A_2\right|^2\right)\right]A_2,\end{aligned} \tag{4.4.1}$$

$$\begin{aligned}\partial_z A_S(z,t) &= \left[\sum_{\nu>0}\frac{i^{\nu+1}}{\nu!}\beta_{\nu,S}\partial_t^\nu + i\alpha_S\left(Q_{S,1}^{(\mathrm{XPM})}\left|A_1\right|^2 + Q_{S,2}^{(\mathrm{XPM})}\left|A_2\right|^2\right)\right]A_S\\ &+ i\alpha_S\left[\sum_A Q_{S,A}^{(\mathrm{FWM1})}A_1^2A_A^*\exp\left\{i\left[\left(2\beta_1-\beta_A-\beta_S\right)z-\left(2\omega_1-\omega_A-\omega_S\right)t\right]\right\}\right.\\ &\quad + Q_{S,A}^{(\mathrm{FWM2})}A_2^2A_A^*\exp\left\{\left[\left(2\beta_2-\beta_A-\beta_S\right)z-\left(2\omega_2-\omega_A-\omega_S\right)t\right]\right\}\\ &\quad \left.+ Q_{S,A}^{(\mathrm{FWM3})}A_1A_2A_A^*\exp\left\{i\left[\left(\beta_1+\beta_2-\beta_A-\beta_S\right)z-\left(\omega_1+\omega_2-\omega_A-\omega_S\right)t\right]\right\}\right],\end{aligned} \tag{4.4.2}$$

where $\beta_{\nu,q}(\omega_0)=\left(\partial^\nu\beta_q(\omega)/\partial\omega^\nu\right)_{\omega_0}$ accounts for dispersion. The number of terms required in the dispersion expansion will depend on the bandwidth under consideration. The dynamics equation for the anti-Stokes mode A is obtained by the substitution S ↔ A in Eq. (4.4.2). While Eqs. (4.4.1) are in a form which can

be solved using the nonlinear Fourier split-step technique [27], Eq. (4.4.2) requires a much slower finite-difference procedure. In addition, the nature of Eq. (4.4.2) necessitates extremely small t and z step sizes to accurately capture potentially high frequency beating. As such, in this portion of the paper we limit our efforts to utilizing Eq. (4.4.1) to perform a partial validation of our analysis. That is, we explore FWM-based parametric amplification where the generated Stokes and anti-Stokes signals are both in the same spatial mode(s) as the pump(s), but at new frequencies. In this case the FWM processes are equivalent to the scalar modulation instability (SMI) and cross-phase modulation instability (XPMI) previously explored in both single-mode and multi-mode fibers [42] [43].

Since the Fourier split-step simulation technique requires finite-duration signals, we use 0.8 ns length supergaussian pulses. For each test case we perform 100 simulations with white Gaussian noise added to the beam profiles before propagation. This noise acts as a seed for signal generation. We then analyze the ensemble average spectra after propagation. When performing the Fourier transforms of the final envelopes, we only utilize the beam content within the pulse width to better approximate CW behavior. Dispersion terms up to fourth order (β_4) are included to ensure that the phase matching processes within the simulations are accurate across the bandwidth of interest.

As for the fiber, we consider an air-core ring fiber as shown in Fig. 4.2(a) [37] [41] [44] [45] [46] [47]. It consists of an 8 μm radius air-filled core surrounded by a 2 μm thick high refractive index ring of a GeO_2-SiO_2 mixture, followed by a cladding of pure SiO_2. The ring-shaped refractive index profile

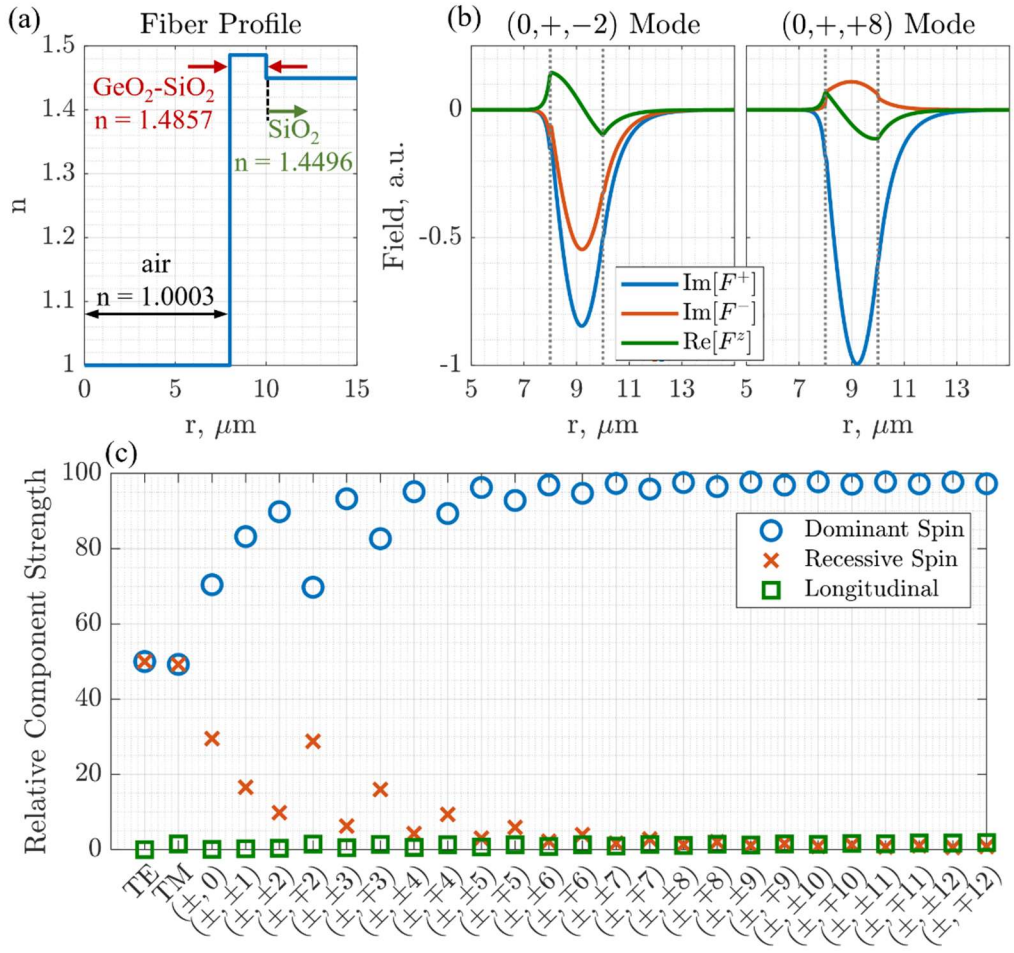


Figure 4.2: (a) Refractive index profile for the air-core ring fiber under consideration. (b) Field profiles of the (0,–,+2) and (0,+,+8) modes. The mode solving procedure utilized generates profiles with purely real F^z components and purely complex F^+ and F^- components. (c) Relative strengths of mode components for select fiber modes, quantified per Eq. (4.4.3). The radial orders p is omitted to keep the figure more legible but are equal to 0. All quantities displayed are evaluated at 1.064 μm.

allows for the stable guiding of SO modes which have characteristic donut intensity profiles. Examples of mode profiles are shown in Fig. 4.2(b). We observe that, for the (0,+,–2) mode, the recessive spin component (RCP in this case) is comparable to, but still smaller than, the dominant spin component (LCP). On the other hand, the higher- mode (0,+,+8) has a fairly negligible recessive spin

component. To characterize this effect across all modes in the fiber, we quantify the relative strengths of each mode's $\hat{\mathbf{e}}_j$ component as

$$\bar{P}_q^j = \frac{\int d^2r \left| \tilde{\mathbf{F}}_q(\mathbf{r}_\perp, \omega_0) \cdot \hat{\mathbf{e}}_j \right|^2}{\int d^2r \left| \tilde{\mathbf{F}}_q(\mathbf{r}_\perp, \omega_0) \right|^2}. \tag{4.4.3}$$

The results for a selection of modes are shown in Fig. 4.2(c). As discussed earlier, the two spin components for TE and TM modes have the same strengths. Additionally, as *m* increases, the recessive spin component does become weak. Generally speaking, modes with higher *m* can be well approximated by the profile $\tilde{\mathbf{F}}_{(p,\pm,m)}(\mathbf{r}_\perp, \omega_0) \simeq \hat{\boldsymbol{\sigma}}_\pm \tilde{F}_{(p,\pm,m)}(r, \omega_0) \exp[im\varphi]$, and FWM processes amongst these modes will, also to good approximation, conserve OAM and SAM independently. On the other hand, TE, TM, and modes with low *m* are better described by their full forms Eqs. (4.2.7) – (4.2.10), and will not have such a restriction. What quantifies as "high" versus "low" *m* will vary depending on the fiber design and the level of analytical precision desired.

4.4.2 Scalar Modulation Instability of the (0,–,+8) Spatial Mode

We first explore the case of a single pump: a 0.8 ns supergaussian pulse in the (0,–,+8) spatial mode at 1.064 μm, with 1 kW peak power propagating over 3 meters. We consider only new Stokes and anti-Stokes signals which are also in the (0,–,+8) spatial mode; this is equivalent to scalar modulation instability (SMI). The relevant dispersion and overlap coefficients are provided in the first column of Table 2. Note that, for SMI, $Q^{(\mathrm{SPM})} = Q^{(\mathrm{FWM1})}$. Since this mode is in the anomalous dispersion regime ($\beta_2 < 0$) it will undergo the typical scalar modulation

instability [27] and develop broad, symmetric sidebands about the pump frequency with peaks at λ_S = 1.108 μm and λ_A = 1.023 μm. In addition, the dispersion curve is phase matched at a further detuning with peaks at λ_S = 1.305 μm, λ_A = 0.898 μm. The simulation results are compared to the predictions of Eq. (4.3.8) in Fig. 4.3.

Table 2: Dispersion and overlap parameters used for simulations. Quantities are evaluated at the wavelength λ = 1.064 μm.

	(0,–,+8)	(0,+,+2)	(0,+, –2)
n_{eff}	1.4648	1.4719	1.4714
β_1, s/m	5.043E−09	5.021E−09	5.022E−09
β_2, s^2/m	−4.997E−28	2.088E−26	2.065E−26
β_3, s^3/m	5.327E−41	3.086E−41	2.660E−41
β_4, s^4/m	5.342E−56	2.991E−56	5.989E−56
$Q^{(SPM)}$, V^4/W^2-m^2	2.424E+15	2.761E+15	3.285E+15
$Q^{(XPM)}$, V^4/W^2-m^2	–	3.412E+15	3.412E+15

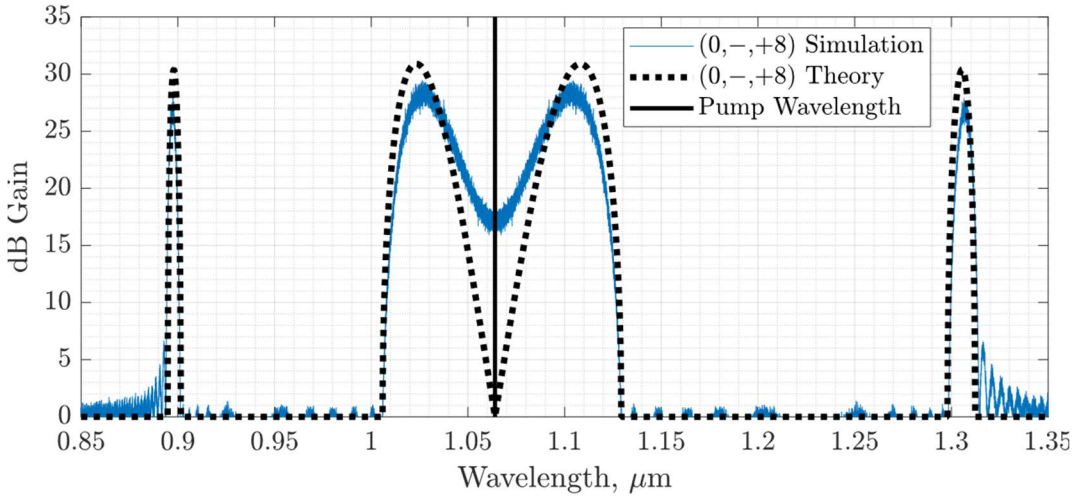


Figure 4.3: Simulation and theory results of a pump in the (0,–,+8) spatial mode at 1.064 μm, 1 kW peak power, and propagating over 3 m. The two pairs of peaks are also in the (0, –,+8) spatial mode, and are characteristic of SMI.

We observe that the locations of the new modes are accurately predicted, including the spectral widths, although the gains are slightly overpredicted. When considering signals that may be generated in new spatial modes, and the large number of spatial modes that are available in the fiber, it may be desirable to ensure the new signals have smaller bandwidths to prevent spectral overlap and avoid possible interference in signal growth. In Eqs. (4.3.8) we observe that decreasing the pump power will decrease the signal bandwidth, though a longer fiber will be needed to reach the same power levels. To test this, we repeat the

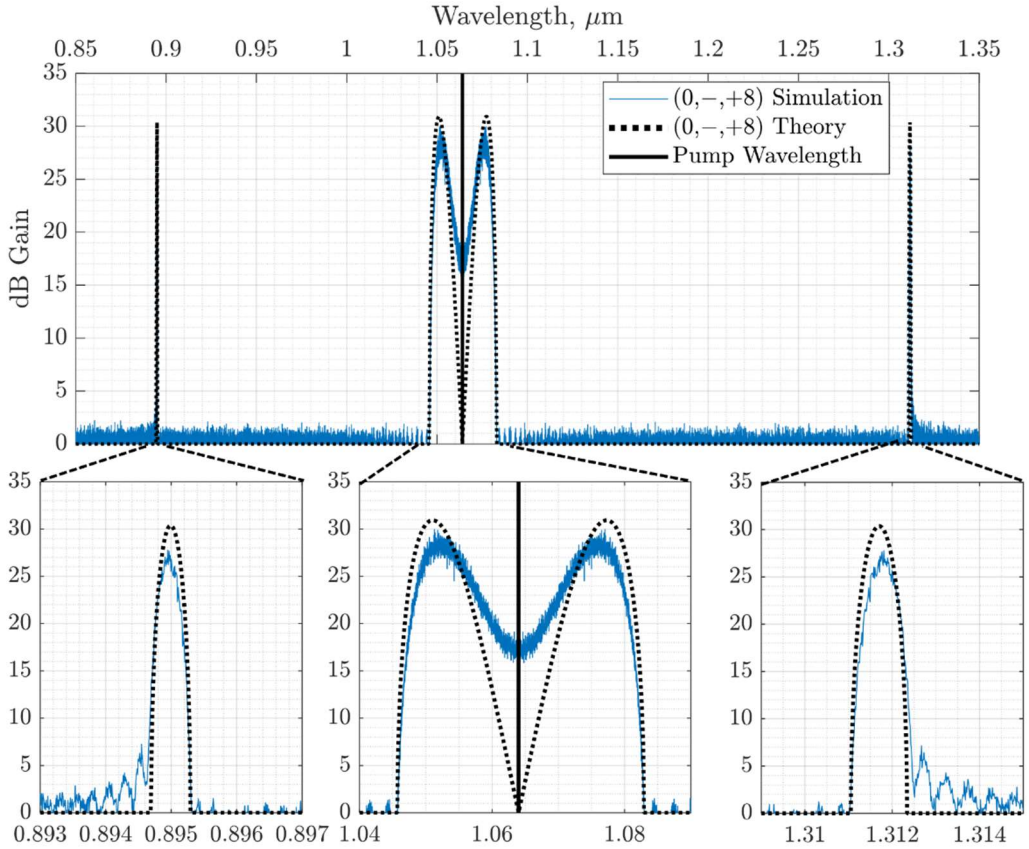


Figure 4.4: Simulation and theory results of a pump in the (0,–,+8) spatial mode at 1.064 μm, 100 W power, and propagating over 30 m. Compared to the prior case, the lower power and longer fiber length allows for new signals with narrower bandwidths.

prior case but with a 100 W pump and 30 m fiber length. The results are shown in Fig. 4.4. As predicted, the peak gains remain unchanged while the spectral widths are reduced to ≲1 nm for the further detuned signals.

4.4.3 Cross Phase Modulation Instability of the (0,±,+2) Spatial Modes

We next explore the case of two pumps: one in the (0,–,+2) spatial mode, and the other in the (0,+,+2) spatial mode. Here, again, both pumps consist of 0.8 ns supergaussian pulses centered at 1.064 μm, have 100 W peak power, and propagate 30 m. We consider only new Stokes and anti-Stokes signals in either (0,±,+2) spatial modes. This is equivalent to cross phase modulation instability (XPMI). The relevant dispersion and overlap coefficients are provided in the second and third columns of Table 2 (note that, for XPMI, $Q^{(\mathrm{XPM})} = Q^{(\mathrm{FWM3})}$).

The simulation results are presented in Fig. 4.5. Neither mode has phase-matched SMI processes as the (0,–,+8) spatial mode does; however, there is a XPMI process predicted to occur, based on Eq. (4.3.8), with the (0,–,+2) spatial mode at $\lambda_S = 1.1138$ μm and the (0,+,+2) spatial mode at $\lambda_A = 1.0185$ μm. This is consistent with XPMI observed in other fiber types, where the slow mode (higher β_1) is Stokes shifted, while the fast mode (lower β_1) is anti-Stokes shifted [42] [47]. Equation (4.3.8) also predicts a set of peaks detuned by ~0.1 nm from the pump. These correspond to the first-order approximation to the phase matching condition, $(\beta_{1,S} - \beta_{1,A})\ \Omega = \theta_1 + \theta_2 - \theta_S - \theta_A$, where Ω is the detuning. These signals are not present in the simulation: neither at the end of the 30 m fiber, nor any intermediately sampled distance. Analogous peaks were similarly not present for other simulations that used different inputs spatial modes, powers, and/or

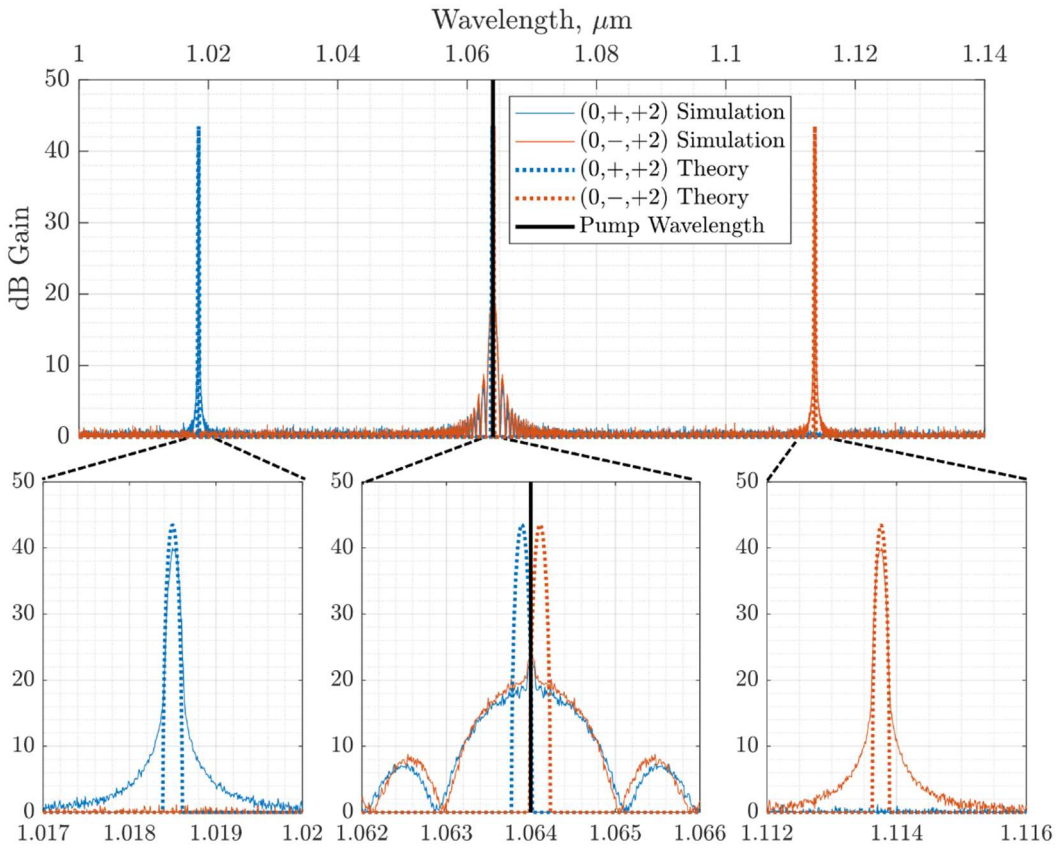


Figure 4.5: Simulation and theory results of pumps in the (0,+,+2) and (0,–,+2) spatial modes at 1.064 μm, 100 W power, and propagating over 30 m. The set of peaks with the slow mode (higher β_1) Stokes shifted and fast mode (lower β_1) anti-Stokes shifted is consistent with the XPMI phenomenon.

propagation lengths. Since the derivation of the growth rates provided in Eqs. (4.3.8) effectively assume *distinct* modes which are sufficiently separated in frequency, the very narrow detuning of these modes, and even partial overlap in the gain curves with the pump frequency, may feed other nonlinear processes which suppresses their growth.

4.5 Generation of New Spatial Modes

We now study the generation of spatial modes different than the pump(s), continuing with the case of pumps in the (0,±,+2) spatial modes at 1.064 μm. The

FWM overlap integrals, Eqs. (4.3.7), are evaluated for all spatial mode permutations and, when they are nonzero, Eqs. (4.3.8) are calculated for the peak growth rates. The results for degenerate and nondegenerate FWM processes are shown in Figs. 4.6 and 4.7 respectively. The growth rates are normalized to the pump power and are accurate for pumps up to ~1 kW (changes in the Stokes and anti-Stokes frequencies due to nonlinear phase shifts are at most ~1nm for 1 kW pumps for this test case). The *x*-axis denotes the Stokes and anti-Stokes modes generated. Note that all generated modes have zero radial order, and thus *p* is omitted from the mode labels to make the figures more legible. In addition, the last numbers in the labels are the wavelengths in μm. To emphasize how angular

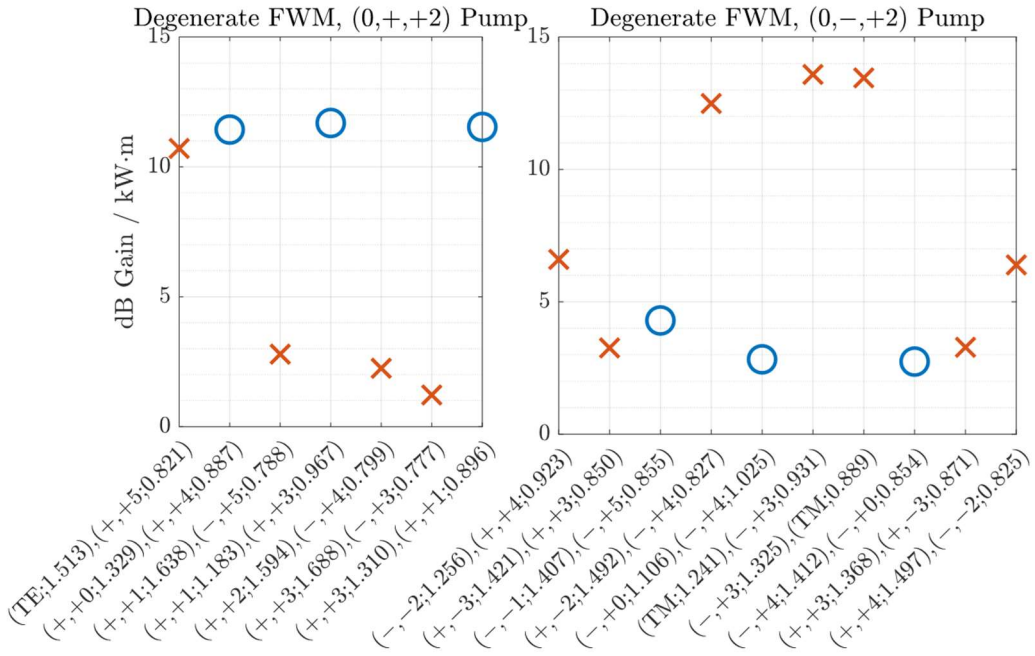


Figure 4.6: New modes created by *degenerate* FWM-based parametric amplification from (0,+,+2) and (0,–,+2) pumps at 1.064 μm. The radial orders *p* is omitted to keep the figure more legible, but are equal to 0. The last numbers in the mode labels are the wavelengths in μm. Processes that conserve SAM and OAM independently are marked with blue circles, while those that only conserve TAM are marked with red x's.

momentum evolves between the pump(s) and amplified modes, processes which conserve OAM and SAM independently are marked with blue circles while processes which do not are marked with red x's.

Figure 4.6 (left) provides the growth rates for modes generated by degenerate FWM of the (0,+,+2) pump. Recall that the TAM of an SO mode is quantized by J in Eqs. (4.2.5) and (4.2.6), i.e. $J = s + m$, where s is the dominant spin component and m is the transverse OAM of that dominant spin component, with $J = 0$ for TE and TM modes. Thus, to obtain a nonzero FWM overlap integral, the selection rule $2J_1 = J_A + J_S = +6$ must be satisfied. All of the modes shown satisfy this condition. The differences in gain are due to variations in the

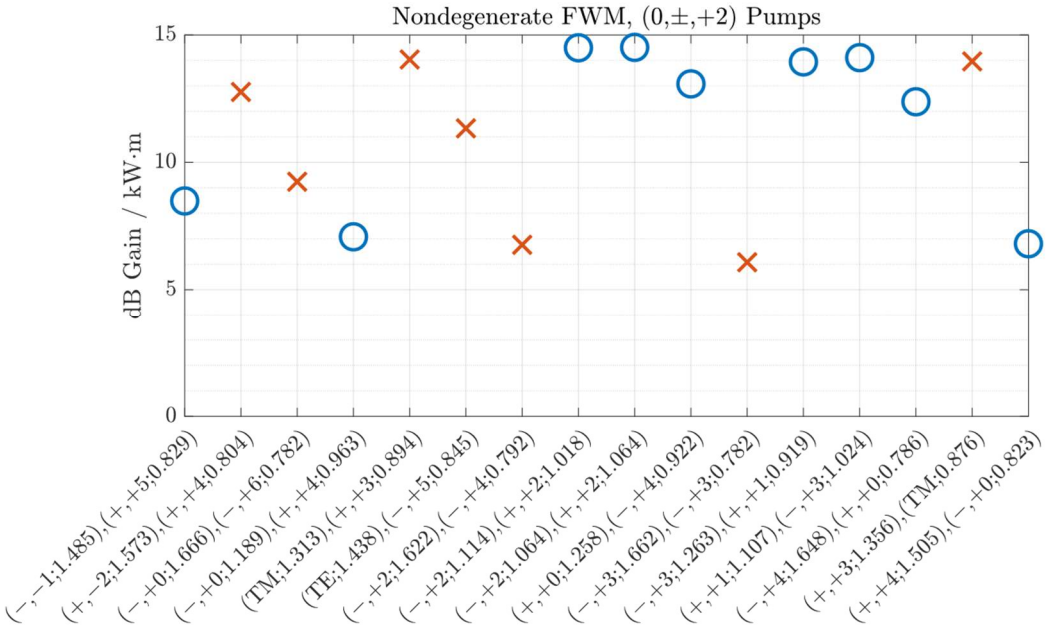


Figure 4.7: Modes created by *nondegenerate* FWM-based parametric amplification with (0,+,+2) and (0,–,+2) pumps at 1.064 μm. The radial orders p is omitted to keep the figure more legible, but are equal to 0. The last numbers in the mode labels are the wavelengths in μm. Processes that conserve SAM and OAM independently are marked with blue circles, while those that only conserve TAM are marked with red x's.

mode profiles and thus overlap integral values. An equivalent selection rule of $2J_2 = J_A + J_S = +2$ is enforced for degenerate FWM from the (0, –,+2) pump, which is shown in Fig. 4.6 (right). Fig. 4.7 shows the growth rates for modes generated by nondegenerate FWM of the two pumps. Here, the selection rule $J_1 + J_2 = J_S + J_A = +4$ is enforced. We note that Raman scattering of the pumps will likely produce a peak at ~1.12 μm, which may mask or disrupt the generation of the modes shown [41].

Under different conditions, such as for a fiber profile with a thicker "ring" section and thus smaller spin-orbit coupling, or when only larger-m modes are involved in the FWM processes, the recessive spin components of the mode profiles can reasonably be discarded, i.e. $\tilde{\mathbf{F}}_{(p,\pm,m)}(\mathbf{r}_\perp,\omega_0) \simeq \hat{\boldsymbol{\sigma}}_\pm \tilde{F}_{(p,\pm,m)}(r,\omega_0)\exp[im\phi]$. In this case the overlap integrals for FWM-based parametric amplification would enforce independent conservation of SAM and OAM, as has been demonstrated in prior experiments [41] [45]. However, for the fiber design and pump configuration considered in this paper, such an approximation is unjustified. For example, one of the most efficient degenerate FWM processes of the (0,–,+2) pump will generate the (0,+,–2) and (0,–,+4) spatial modes at $\lambda_S = 1.492$ μm and $\lambda_A = 0.827$ μm, respectively. Such a process would be "forbidden" under the reduced case.

4.6 Conclusions

In this chapter, we presented a generalized theory of four-wave mixing (FWM)-based parametric amplification for modes in azimuthally symmetric optical fibers. Strictly speaking, the modes in such fibers are characterized by a total angular

momentum (TAM) quanta *J*, where each photon carries $J\hbar\hat{\mathbf{z}}$ angular momentum. Such modes have nonzero LCP and RCP spin components. We showed that this feature translates to selection rules during FWM-based parametric amplification, wherein TAM must be conserved. This is a generalization of prior research [41] [45], where the fiber design and mode subset utilized allowed for the modes to be well-approximated as "pure" spin-orbit (SO) modes rather than TAM modes. In such cases the selection rules are more restrictive and correspond to conservation of orbital angular momentum (OAM) and spin angular momentum (SAM) independently.

In addition, we derived growth rates of new modes via degenerate and nondegenerate parametric amplification. Numerical simulations were performed for the cases where the generated Stokes and anti-Stokes modes are in the same spatial mode as the pump(s) – equivalent to scalar and cross-phase modulation instability of the pump beam(s). Our numerical simulations are in good agreement with our theory. We also calculated the growth rates of all new SO modes from a nondegenerate pump configuration and found that processes which "break" the selection rules for independent conservation of SAM and OAM, but are allowed under conservation of TAM, can be significant.

Chapter 5 Future Work

The most evident avenue for future work is rigorous experimental validation of the theories presented. For Chapter 2, which discussed the evolution of low power LG beams in turbulence, one could perform a tabletop experiment utilizing a sequence of spatial light modulators (SLMs) to mimic the effects of turbulence in a highly controlled fashion [48] [49] [50]. The full LG mode composition of the distorted beam can be determined using a combined log-polar and fractional Fourier transformers [50].

For the high-power pulses investigated in Chapter 3, the high intensities necessary to achieve self-focusing will likely damage SLMs and other optical elements. In addition, mimicking the impact of GVD on long distance pulse propagation on a tabletop is difficult. As such, the best option is likely an experimental configuration akin to the one utilized by Helle *et al.* [26]. A technique for measuring the LG mode composition of a high-power beam will need to be determined.

Finally, experimental configurations that could validate the results of Chapter 4 already exist, and were depicted in Fig. 1.4 [41] [45] [47]. Designing and fabricating a fiber with and viable FWM phase matching conditions and SO modes with sufficiently strong "recessive" components may be difficult. That said, utilizing pumps in the TE and/or TM modes should allow for the confirmation of total angular momentum conservation during FWM processes.

Appendix A Simulations of Low Power Beams in Turbulence

Throughout this manuscript, we have mentioned utilizing simulations to directly evaluate complex, statistical differential equations as a comparison point for reduced models and tests of phenomenology. Here, we provide details on the simulation procedures utilized for low power beam propagation through turbulence seen in Chapter 2.

Consider the paraxial wave equation without turbulence: $\partial_z \tilde{U}_0(\mathbf{r}_\perp,\omega) = \frac{i}{2k_0}\nabla_\perp^2 \tilde{U}_0(\mathbf{r}_\perp,\omega)$. Fourier transforming in the transverse direction ($\mathbf{r}_\perp \leftrightarrow \boldsymbol{\kappa}_\perp$), one can readily obtain the solution for the field at z given an initial field via

$$\tilde{U}_0(\boldsymbol{\kappa}_\perp,z) = \tilde{U}_0(\boldsymbol{\kappa}_\perp,0)\exp\left[\frac{-iz}{2k_0}\left(\kappa_x^2+\kappa_y^2\right)\right]. \tag{A.1}$$

Or, if we want to utilize the initial and final fields in real space, we can write this as

$$\tilde{U}_0(\mathbf{r}_\perp,z) = \mathbb{F}_{2\mathrm{D}}^{-1}\left\{\exp\left[\frac{-iz}{2k_0}\left(\kappa_x^2+\kappa_y^2\right)\right]\mathbb{F}_{2\mathrm{D}}\left\{\tilde{U}_0(\mathbf{r}_\perp,0)\right\}\right\}, \tag{A.2}$$

where $\mathbb{F}_{2\mathrm{D}}$ and $\mathbb{F}_{2\mathrm{D}}^{-1}$ indicate 2D forward and inverse Fourier transforms, respectively.

The effects of turbulence are introduced with the Rytov approximation – that is, $\tilde{U}(\mathbf{r}) = \tilde{U}_0(\mathbf{r})\exp\left[\Psi(\mathbf{r})\right]$, where Ψ is the path-integrated phase shift which obeys the statistics of the desired turbulent spectrum (e.g. Kolmogorov or

modified von Kármán). Since the Rytov approximation is only valid for weak turbulence $\sigma_R^2 \ll 1$, to simulate propagation through moderate or strong turbulence one needs to break the full propagation distance into sections for which $\sigma_R^2 \ll 1$. This procedure is often called the (Fourier) Split-Step Method. Enumerating the steps to propagate an initial beam $\tilde{U}(\mathbf{r}_\perp, 0)$ through turbulence to obtain $\tilde{U}(\mathbf{r}_\perp, z)$:

1. Determine a distance Δz such that $\sigma_R^2(\Delta z) \ll 1$ and $z = N_{\Delta z}\Delta z$ for some integer $N_{\Delta z}$.
2. Apply Eq. (A.2) to propagate the beam a distance $\Delta z/2$.
3. Multiply the beam by a phase perturbation $\exp[\Psi(\mathbf{r})]$.
4. Apply Eq. (A.2) again to propagate the perturbed beam a distance $\Delta z/2$.
5. Repeat steps $2-4$ $(N_{\Delta z} - 1)$ times.

This process is illustrated in Fig. A.1. Note that this procedure will only provide a single realization of propagated beam. In practice, the statistics of various quantities are of interest; thus, the simulation is performed many times to form a Monte Carlo ensemble. For further details on free-space beam propagation techniques, Schmidt [52] is recommended.

What was omitted from the above description is the actual construction of phase screens $\Psi(\mathbf{r}_\perp)$. In this dissertation we utilize the Paulson-Wu-Davis algorithm [53] [54]. A detailed description of this and other algorithms is beyond the scope of this dissertation.

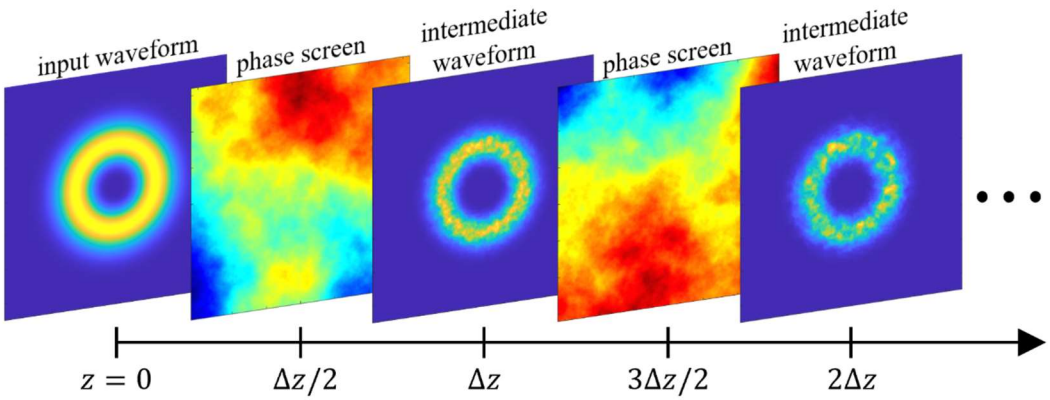


Figure A.1: Illustration of the split-step beam propagation method for a low power CW beam in turbulence. Each step size Δz obeys $\sigma_R^2(\Delta z) \ll 1$, such that the Rytov approximation is valid.

The MATLAB functions presented after the appendices will allow you to perform simple simulations of low power beams propagating through turbulence. The principal function for low power propagation is `simpleSplitStepTurb.m`, which takes in an initial beam profile `UIn` and propagates it a requested distance `L`, returning the distorted beam profile at `L` and half-way between every phase screen. The function `pwdPhaseScreenMvk.m` constructs phase screens using the Paulson-Davis-Wu algorithm [53]. `ft2.m` and `ift2.m` perform digital Fourier and inverse Fourier transforms in a concise fashion.

The script `testLinearSplitStepTurb_SCRIPT.m` provides an example of how to execute a simulation. In it, a Gaussian beam is propagated through moderate Kolmogorov turbulence to characterize the beam centroid displacement and the on-axis scintillation index. The ensemble average values are then compared to a theoretical result [18] [55], which is also provided as `beamWanderVarianceTheory.m` and `onAxisIntensityTheory.m`. The output of the script is shown in Fig. A.2.

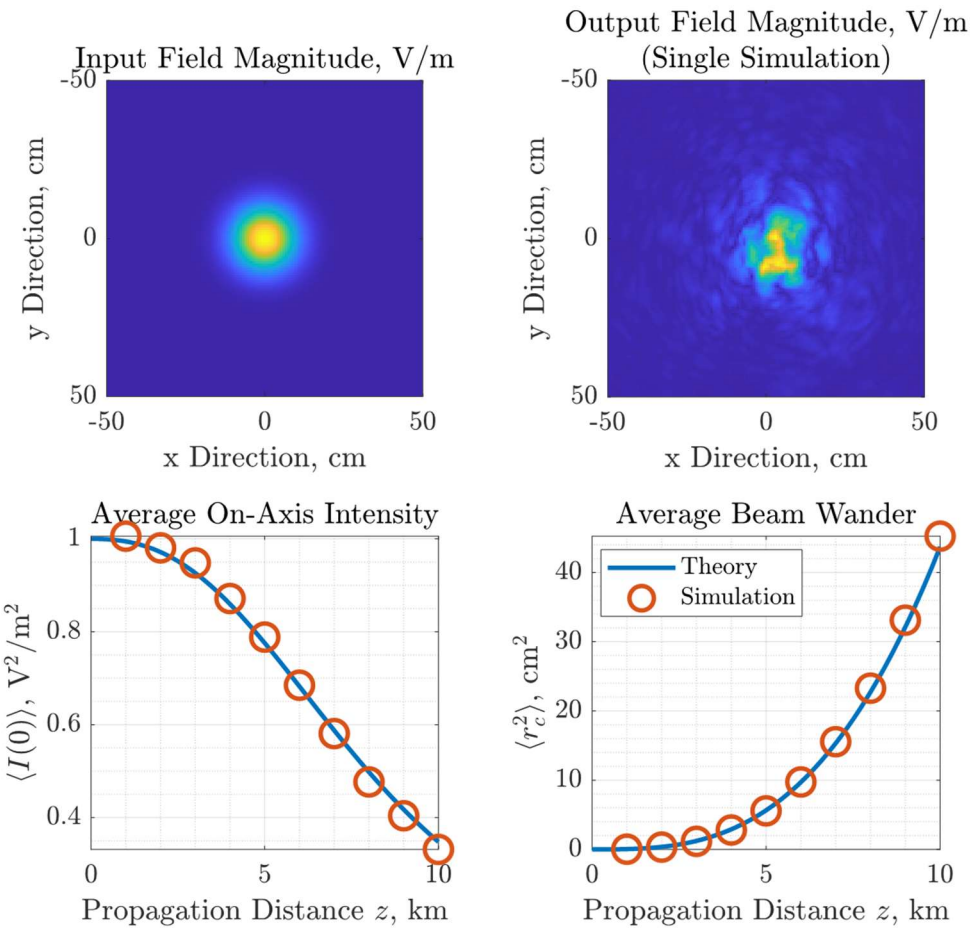


Figure A.2: Simulation results for the propagation of a low power CW Gaussian beam in Kolmogorov turbulence. The average on-axis intensity and beam wander are compared to analytic relations.

Note that all MATLAB code presented in these Appendices has been made available online at https://gitlab.com/henry.elder/nonlin-beam-prop.

Appendix B Simulations of High-Power Pulses in Turbulence

We now expand upon the Fourier split-step simulation procedure introduced in Appendix A by including SPM and dispersion. We again account for turbulence using the Rytov approximation, so we first want to propagate our governing nonlinear pulse differential equation with $\delta n = 0$. Splitting it into linear $\hat{L}$ and nonlinear $\hat{N}$ parts,

$$\partial_\eta U_0(\mathbf{r}_\perp,\eta,\tau) = \Bigg[\underbrace{\frac{i}{2k_0}\nabla_\perp^2 - \frac{ik_2}{2}\partial_\tau^2}_{\hat{L}} + \underbrace{\frac{3ik_0\chi^{(3)}}{8n_0^2}|U|^2}_{\hat{N}} \Bigg] U_0(\mathbf{r}_\perp,\eta,\tau). \tag{B.1}$$

An initial pulse envelope can be propagated from η to $\eta+\Delta\eta$ via

$$U_0(\mathbf{r}_\perp,\eta+\Delta\eta,\tau) = \exp\left[\left(\hat{L}+\hat{N}\right)\Delta\eta\right] U_0(\mathbf{r}_\perp,\eta,\tau). \tag{B.2}$$

To perform this propagation, we use the *symmetrized*, *nonlinear* Fourier split-step technique: [27] [56]

$$\begin{aligned} &U_0(\mathbf{r}_\perp,\eta+\Delta\eta,\tau) = \\ &\quad \exp\left[\hat{L}\frac{\Delta\eta}{2}\right]\exp\left[\int_\eta^{\eta+\Delta\eta} d\eta'\,\hat{N}(\eta')\right]\exp\left[\hat{L}\frac{\Delta\eta}{2}\right] U_0(\mathbf{r}_\perp,\eta,\tau). \end{aligned} \tag{B.3}$$

Here, the linear portion utilizes the same technique as in Appendix A, but with spatial and temporal Fourier transforms to account for diffraction and dispersion:

$$\begin{aligned} &\exp\left[\hat{L}\frac{\Delta\eta}{2}\right] U_0(\mathbf{r}_\perp,\eta,\tau) = \\ &\quad \mathbb{F}_{2D+1}^{-1}\left\{ \exp\left[\frac{-i\Delta\eta}{4k_0}\left(\kappa_x^2+\kappa_y^2\right)+\frac{ik_2\Delta\eta}{4}\omega^2\right]\mathbb{F}_{2D+1}\left\{U_0(\mathbf{r}_\perp,\eta,\tau)\right\}\right\}, \end{aligned} \tag{B.4}$$

where $\mathbb{F}_{2D+1}$ and $\mathbb{F}_{2D+1}^{-1}$ indicate 2D spatial, 1D temporal forward and inverse Fourier transforms, respectively. The nonlinear portion is trickier: upon

inspection, one realizes that solving the integral implies knowledge of the field envelope between η and $\eta+\Delta\eta$ – i.e. we already know the solution. To deal with this, the integral is solved iteratively with a two-point trapezoidal approximation. Enumerating the steps to propagate a beam $\tilde{U}_0(\mathbf{r}_\perp,\eta,\tau)$ over a distance $\Delta\eta$:

1. Perform a linear propagation over a distance $\Delta\eta/2$ to obtain $\tilde{U}_0^{(1)}(\mathbf{r}_\perp,\eta+\Delta\eta/2,\tau)$.
2. Calculate the first estimate of the nonlinear contribution using this mid-point value, i.e. $\int_\eta^{\eta+\Delta\eta} d\eta'\,\hat{N}(\eta') \approx \Delta\eta\,\frac{3ik_0\chi^{(3)}}{8n_0^2}\left|\tilde{U}_0^{(1)}(\mathbf{r}_\perp,\eta+\Delta\eta/2,\tau)\right|^2$.
3. Perform another linear propagation over a distance $\Delta\eta/2$ to obtain $\tilde{U}_0^{(1)}(\mathbf{r}_\perp,\eta+\Delta\eta,\tau)$.
4. Calculate a new (and improved) estimate of the nonlinear contribution using $\int_\eta^{\eta+\Delta\eta} d\eta'\,\hat{N}(\eta') \approx \frac{\Delta\eta}{2}\frac{3ik_0\chi^{(3)}}{8n_0^2}\left[\left|\tilde{U}_0^{(1)}(\mathbf{r}_\perp,\eta+\Delta\eta,\tau)\right|^2+\left|\tilde{U}_0(\mathbf{r}_\perp,\eta,\tau)\right|^2\right]$.
5. Perform another linear propagation over a distance $\Delta\eta/2$ to obtain a new (and improved) estimate of the beam at $\eta+\Delta\eta$, $\tilde{U}_0^{(2)}(\mathbf{r}_\perp,\eta+\Delta\eta,\tau)$.
6. Repeat steps 4 and 5 until convergence.

Note that for this process to be accurate, the step size $\Delta\eta$ needs to be fairly small – much smaller than would typically be dictated by the Rytov weak-turbulence requirement. One can estimate the characteristic nonlinear length scale via $L_{\mathrm{NL}} = 8n_0^2 \big/ 3k_0\chi^{(3)}\left|U\right|_{\max}^2$, where $\left|U\right|_{\max}^2$ is the peak value of $\left|U\right|^2$. As long as $\delta\eta \ll L_{\mathrm{NL}}$, the iterative procedure for incorporating Kerr focusing will be accurate.

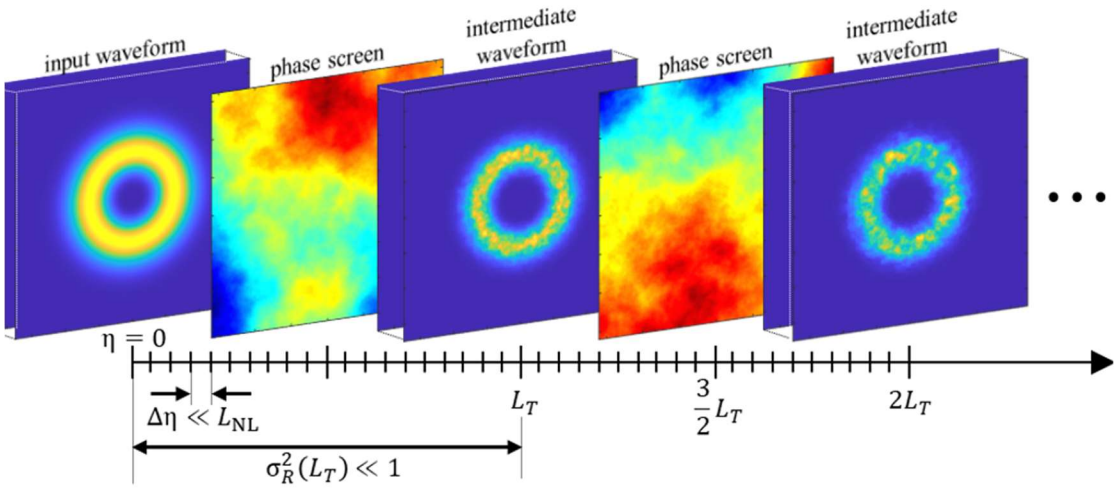


Figure B.1: Illustration of the nonlinear split-step beam propagation method for a high-power pulse in turbulence. The step size obeys $\Delta\eta \ll L_{\mathrm{NL}}$ where $L_{\mathrm{NL}} = 8n_0^2 \big/ 3k_0\chi^{(3)}\left|U\right|^2_{\max}$ is the characteristic nonlinear length scale. The phase screens are separated by L_T, which satisfies $\sigma_R^2(L_T) \ll 1$.

Phase screens can still be added to account for turbulence. The turbulent, non-linear Fourier split-step procedure is illustrated in Fig. B.1. Again, note that this procedure will only provide a single realization of the propagated beam. In practice, the statistics of various quantities are of interest; thus, the simulation is performed many times to form a Monte Carlo ensemble.

The MATLAB functions provided at the end of these appendices will perform nonlinear simulations through turbulence. The principal function is `simpleNonLinSplitStepTurb.m`, which takes in an initial pulse profile `UIn` and propagates it a requested distance `L`, returning select characteristics of the pulse at `L` and half-way between every phase screen. The function `pwdPhaseScreenMvk.m` is borrowed from Appendix A. `ft2p1.m` and `ift2p1.m` perform digital 2D+1 Fourier and inverse Fourier transforms in a

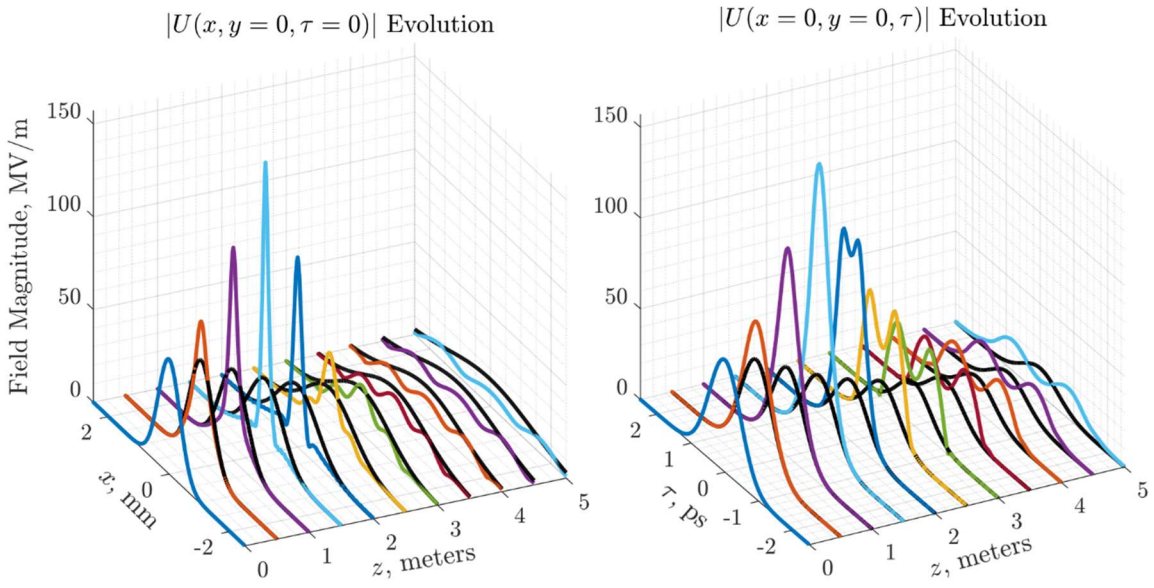


Figure B.2: Simulation results for the propagation of high power Gaussian pulse water. The left and right figures show the evolution of the envelope magnitudes along the x and τ axes, respectively. The peak power is large enough to instigate self-focusing and pulse splitting, but not enough to cause collapse. The black traces show what the linear evolution would be.

concise fashion. The script `testNonLinSplitStepTurb_SCRIPT.m` provides an example of how to execute a simulation. In it, a high-power Gaussian pulse is propagated through water, undergoing self-focusing and pulse splitting. The output of the script is shown in Fig. B.2.

Often times, the computer memory requirement to save the entire pulse state throughout propagation is untenable; rather, select quantities are extracted and saved. In this case we record the pulse profiles along the x- and τ-axes, along with the pulse energy. The energy is a useful value to track – ensuring its near-conservation helps provides a check that simulation performed adequately. There will be some energy loss since the provided routine utilizes a supergaussian taper function to prevent energy from accumulating at the gridding boundaries, which

would cause numerical issues. Though these losses should not be more than a fraction of one percent.

Also, note that building an ensemble of simulations for nonlinear propagation through turbulence is a significant computational effort – typically requiring a computing cluster to yield results in acceptable timeframes. The example provided forgoes turbulence by setting $C_n^2 = 0$ and will run suitably on a typical personal computer.

Note that all MATLAB code presented in these appendices has been made available online at https://gitlab.com/henry.elder/nonlin-beam-prop.

Appendix C Simulations of High-Power Pulses in Waveguides

We now consider the nonlinear propagation of light through fiber, when the light is in the superposition of two spatial modes A_1 and A_2. Just as in the bulk media case, we split our governing propagation equation into linear $\hat{L}$ and nonlinear $\hat{N}$ parts. Working in the retarded time frame relative to the mean group velocity $\overline{\beta}_1 = \left(\beta_{1,1} + \beta_{1,2}\right)/2$, we have

$$\begin{aligned}
&\partial_\eta A_1(\eta,\tau) = \\
&\Bigg[\underbrace{\left(\overline{\beta}_1 - \beta_{1,1}\right)\partial_\tau + \sum_{\nu>1} \frac{i^{\nu+1}}{\nu!}\beta_{\nu,1}\partial_\tau^\nu}_{\hat{L}_1} + \underbrace{i\alpha_1\left(Q_1^{(\mathrm{SPM})}\left|A_1\right|^2 + Q_{1,2}^{(\mathrm{XPM})}\left|A_2\right|^2\right)}_{\hat{N}_1} \Bigg] A_1(\eta,\tau), \\
&\partial_\eta A_2(\eta,\tau) = \\
&\Bigg[\underbrace{\left(\overline{\beta}_1 - \beta_{1,2}\right)\partial_\tau + \sum_{\nu>1} \frac{i^{\nu+1}}{\nu!}\beta_{\nu,2}\partial_\tau^\nu}_{\hat{L}_2} + \underbrace{i\alpha_2\left(Q_{2,1}^{(\mathrm{XPM})}\left|A_1\right|^2 + Q_2^{(\mathrm{SPM})}\left|A_2\right|^2\right)}_{\hat{N}_2} \Bigg] A_2(\eta,\tau),
\end{aligned} \tag{C.1}$$

where $\alpha_q = \varepsilon_0 \chi^{(3)} \omega_q / 8$ and the overlap integrals Q were defined in Chapter 4. We again utilize the symmetrized nonlinear Fourier split-step technique, e.g. for A_1

$$A_1(\eta+\Delta\eta,\tau) = \exp\left[\hat{L}_1\frac{\Delta\eta}{2}\right]\exp\left[\int_\eta^{\eta+\Delta\eta} d\eta'\,\hat{N}_1(\eta')\right]\exp\left[\hat{L}_1\frac{\Delta\eta}{2}\right]A_1(\eta,\tau), \tag{C.2}$$

where the linear portion is handled in the Fourier domain via

$$\begin{aligned}
&\exp\left[\hat{L}_1\frac{\Delta\eta}{2}\right]A_1(\eta,\tau) \\
&\quad = \mathbb{F}_1^{-1}\left\{\exp\left[-i\left(\left(\overline{\beta}_1 - \beta_{1,1}\right)\omega + \sum_{\nu>1}\frac{i^{\nu+1}}{\nu!}\beta_{\nu,1}\omega^\nu\right)\frac{\Delta\eta}{2}\right]\mathbb{F}_1\left\{A_1(\eta,\tau)\right\}\right\},
\end{aligned} \tag{C.3}$$

where $\mathbb{F}_1$ and $\mathbb{F}_1^{-1}$ indicate the 1D forward and inverse Fourier transforms, respectively. The nonlinear portion can be carried out in an analogous fashion as the bulk media case presented in Appendix B; however, for this coupled systems, each beam is propagated simultaneously.

The MATLAB functions provided at the end of these appendices will perform a single nonlinear simulation of two spatial modes through fiber. The principal simulation function is `simpleNonLinSplitStepFiber.m`, which takes in two initial pulses profile `A1In A2In` and propagates them a requested distance `L`, returning the pulse states at `L` and at `NSave` intermediate locations. `ft1.m` and `ift1.m` perform digital 1D Fourier and inverse Fourier transforms in a concise fashion.

The script `testNonLinSplitStepFiber_SCRIPT.m` provides an example of how to execute a simulation. In it, we propagate a bright-dark soliton

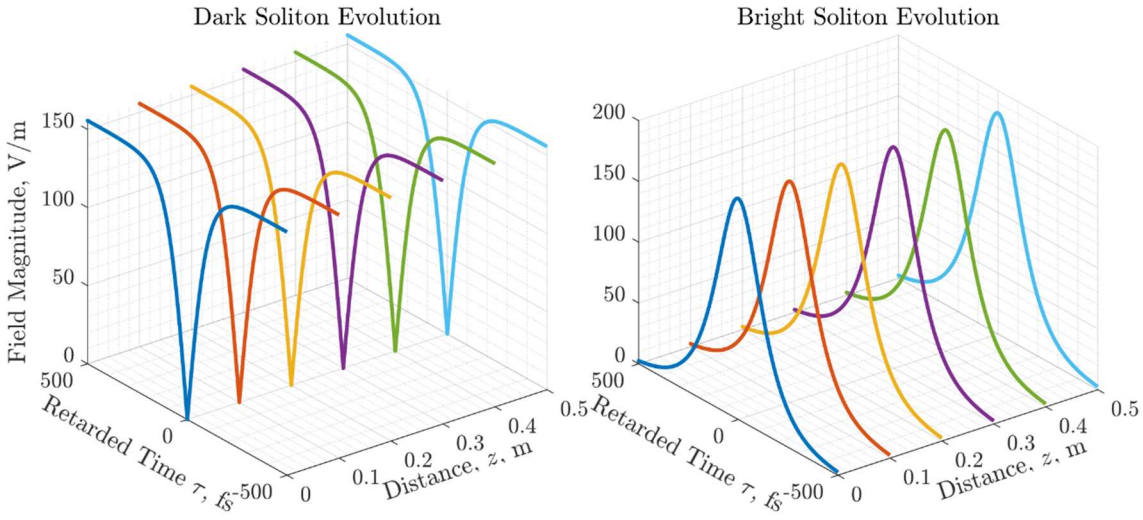


Figure C.1: Simulation results for the propagation of a bright-dark soliton pair. Without the nonlinear interactions the pulses would lengthen to about 1 ps.

pair; the dark soliton (A_1) is a null in a CW background signal, while the bright soliton (A_2) has a more typical sech form [27]. In the low power regime these waveforms would undergo significant pulse broadening, but SPM and XPM balance dispersion to produce soliton behavior. The output of the script is shown in Fig. C.1.

Note that all MATLAB code presented in these appendices has been made available online at https://gitlab.com/henry.elder/nonlin-beam-prop.

List of Publications and Talks

- H. F. Elder, S. K. Dacha, T. E. Murphy, and P. Sprangle, "Theory of Four-Wave Mixing-Based Parametric Amplification of Spin-Orbit Modes", Optics Express [Submitted October 2023. Currently In Review]
- H. F. Elder and P. Sprangle, "Full Mode Power Spectrum for Laguerre-Gauss Beams in Strong Kolmogorov Turbulence", Optics Express 30(25) (2022).
- H. F. Elder and P. Sprangle, "Mode Power Spectrum for Laguerre-Gauss Beams in Kolmogorov Turbulence", Optics Letters 47(14) (2022).
- S. K. Dacha, H. F. Elder, Z. Wenqi, A. Agrawal, P. Sprangle, and T. E. Murphy, "Observation of Conjugate OAM Mode Generation via Modulational Instability in a Hollow Ring-Core Fiber", Optica Nonlinear Optics Topical Meeting, Th3A.6 (2023).
- H. F. Elder, V. Markov, and P. Sprangle, "Propagation of Orbital Angular Momentum Beams in the Atmosphere", DEPS Directed Energy Systems Symposium, 21-Systems-128 (2021).
- H. F. Elder, V. Markov, A. Khizhnyak, and P. Sprangle, "Nonlinear Propagation of Orbital Angular Momentum Beams in Turbulence", DEPS Advanced High-Power Laser and Beam Control Conference, 21-AHPL-019 (2021).
- H. F. Elder, A. Khizhnyak, V. Markov, and P. Sprangle. "Nonlinear Dynamics of the Laser Spot Size and Pulse Duration in Turbulence", SPIE Proceedings Volume 11834, Laser Communication and Propagation through the Atmosphere and Oceans X; 118340Q (2021).

```
% testLinearSplitStepTurb_SCRIPT.m
% Demonstrate the use of simpleSplitStepTurb.m by comparing the on-axis
% scintillation and beam centroid wander of a Gaussian beam in Kolmogorov
% turbulence against theoretical results. This test case demonstrates the
% accurate implementation of diffraction and turbulence.
%
% Henry Elder, helder@umd.edu

clear; close all; clc;
% Specify beam parameters
LAM0 = 1600E-9; % wavelength, m
W0 = 0.1; % initial spot size, m
F0 = inf; % initial phase curvature, m
% Specify the air channel parameters
N0 = 1.0003; % refractive index
K0 = 2*pi*N0/LAM0; % wavenumber, rad/m
CN2 = 1.39E-15; % structure constant, m^-2/3
ELL0 = 0; % inner scale length, m
L0 = inf; % outer scale length, m
L  = 10E3; % total propagation distance, m
% Specify sampling parameters
DXY = 7.5E-3; % grid spacing, m
NXY = 256; % number of grid points
NSCREEN = 10; % number of phase screens
NMONTE = 1000; % number of Monte Carlo iterations

% Define input (Gaussian) waveform
X1D = (-NXY/2:NXY/2-1)*DXY;
[X2D,Y2D] = meshgrid(X1D,X1D); % 2D X and Y domains, m
UIn = exp(-(1/W0^2+0.5i*K0/F0)*(X2D.^2+Y2D.^2)); % input Gaussian, V/m

% Run simulation
Intensity0 = zeros(NMONTE,NSCREEN); % on-axis intensity, V^2/m^2
Xc = zeros(NMONTE,NSCREEN); % X centroid positions, m
Yc = zeros(NMONTE,NSCREEN); % Y centroid positions, m
hw = waitbar(0,'Generating Monte Carlo Ensemble of Simulation Results');
for j = 1:NMONTE
    [UOut,Z] = simpleSplitStepTurb(UIn,K0,          ...
                                   DXY,L,NSCREEN,   ...
                                   CN2,ELL0,L0);
    % Extract and save on-axis intensity and beam centroid position for
    % this iteration
    for jj = 1:NSCREEN
        Intensity = abs(squeeze(UOut(jj,:,:))).^2;
        Power = sum(Intensity,'all') * DXY^2;
        Intensity0(j,jj) = Intensity(NXY/2+1,NXY/2+1);
        Xc(j,jj) = sum(X2D.*Intensity,'all') * DXY^2 / Power;
        Yc(j,jj) = sum(Y2D.*Intensity,'all') * DXY^2 / Power;
    end
    waitbar(j/NMONTE,hw);
end
close(hw);
```

```
% Display results
figure;
tiledlayout(2,2);
% Plot input waveform
nexttile;
imagesc(X1D*1E2,X1D*1E2,abs(UIn));
xlabel('x Direction, cm','interpreter','latex');
ylabel('y Direction, cm','interpreter','latex');
title('Input Field Magnitude, V/m','interpreter','latex');
axis square;
% Plot output waveform for last simulation
nexttile;
imagesc(X1D*1E2,X1D*1E2,squeeze(abs(UOut(end,:,:))));
xlabel('x Direction, cm','interpreter','latex');
ylabel('y Direction, cm','interpreter','latex');
title('Output Field Magnitude (Single Simulation), V/m', ...
      'interpreter','latex');
axis square;
% Plot on-axis intensity
nexttile;
fplot(@(z) onAxisIntensityTheory(K0,W0,F0,CN2,ELL0,L0,z*1E3),[0,L*1E-3],...
      'LineWidth',2);
hold on;
plot(Z*1E-3,mean(Intensity0,1),'o','LineWidth',2,'MarkerSize',12);
grid; grid minor;
xlabel('Propagation Distance $z$, km','interpreter','latex');
ylabel('Average On-Axis Intensity $\langle I(0) \rangle$, V$^2$/m$^2$', ...
       'interpreter','latex');
title('Average On-Axis Intensity of a Gaussian in Turbulence', ...
      'interpreter','latex');
legend('Theory (Andrews and Phillips, 2005)','Simulation',...
       'interpreter','latex');
% Plot beam wander variance
nexttile;
fplot(@(z) 1E4*beamWanderVarianceTheory(K0,W0,F0,CN2,z*1E3),[0,L*1E-3], ...
      'LineWidth',2);
hold on;
plot(Z*1E-3,1E4*mean(Xc.^2+Yc.^2,1),'o','LineWidth',2,'MarkerSize',12);
grid; grid minor;
xlabel('Propagation Distance $z$, km','interpreter','latex');
ylabel('Beam Centroid Variance $\langle r_c^2 \rangle$, cm$^2$', ...
       'interpreter','latex');
title('Beam Wander Variance of a Gaussian in Turbulence', ...
      'interpreter','latex');
legend('Theory (Klyatskin \& Kon, 1972)','Simulation',...
       'interpreter','latex');
% End of testLinearSplitStepTurb_SCRIPT.m
```

```
function [UOut,Z] = simpleSplitStepTurb(UIn,K0,Dxy,L,NScreen,Cn2,Ell0,L0)
%[UOut,Z]=simpleSplitStepTurb(UIn,K0,Dxy,L,NScreen,Cn2,Ell0,L0)
% A simple Fourier split-step beam propagation in turbulence routine. Will
```

```
% return the pulse states at L and half-way between each phase screen.
% Output will be single precision to aid in memory management.
% Inputs
%   UIn - initial beam state, 2D array, [x,y], V/m
%   K0 - carrier wavenumber, scalar, rad/m
%   Dxy - X/Y grid spacing for uin, scalar, m
%   L - total propagation distance, scalar, m
%   NScreen - number of phase screens, scalar
%   Cn2 - turbulence's refractive index structure constant, scalar, m^-2/3
%   Ell0 - turbulence's inner scale length, scalar, m
%   L0 - turbulence's outer scale length, scalar, m
% Outputs
%   UOut - output beam state, 3D array, [step,x,y], V/m
%   Z - propagation distances for UOut, 1D array, m
%
% Henry Elder, helder@umd.edu

% Check grid sizing on UIn
if ~ismatrix(UIn) ||                ... % UIn is 2D?
   (size(UIn,1) ~= size(UIn,2)) || ... % UIn is square?
   (rem(size(UIn,1),2) ~= 0)        % UIn has an even number of samples?
    error(['This function requires a square grid with ' ...
           'an even number of grid points for UIn']);
end

% Check that DZ is small enough for Rytov approximation
if 1.23*Cn2*K0^(7/6)*(L/NScreen)^(11/6) > 0.2
    warning(['Turbulence does not obey RytovVariance << 1. ' ...
             'Results may not be accurate']);
end

% Randomize the seed for MATLAB's random number generator
rng('shuffle');

% Define some useful parameters
Nxy = size(UIn,1); % number of grid points
DFxy = 1 / (Nxy * Dxy); % frequency domain grid spacing, 1/m
Dz = L / NScreen; % distance for each screen's contribution, m
Z = (1:NScreen)*L/NScreen; % propagation distances for UOut, m

% Define phase factor for Fresnel propagation over distance Dz/2
[Nx2D,Ny2D] = meshgrid(-Nxy/2:Nxy/2-1);
Fresnel = exp(1i/(2*K0) * (2i*pi*DFxy)^2*(Nx2D.^2+Ny2D.^2) * Dz/2);

% Define supergaussian taper (absorbing boundary conditions)
SuperGauss = exp(-(Nx2D.^2+Ny2D.^2).^8/(0.43*Nxy)^16);

% Initialze flag for when to compute phase screens
ScreenFlag = true;

% Begin split-step procedure
UOut = single(zeros(NScreen,Nxy,Nxy));
for j = 1:NScreen
    % Propagate dz/2
    UMiddle = ift2(Fresnel .* ft2(UIn,Dxy),DFxy);
```

```
    % Apply phase screen
    if ScreenFlag % Need to compute screens
        [Phase1,Phase2] = pwdPhaseScreenMvk(K0,Nxy,Dxy,Dz,Cn2,Ell0,L0);
        UMiddle = UMiddle .* exp(1i*Phase1);
        ScreenFlag = false;
    else % Do not need to compute new screens
        UMiddle = UMiddle .* exp(1i*Phase2);
        ScreenFlag = true;
    end
    % Propagate another dz/2, and reset for next step
    UIn = SuperGauss .* ift2(Fresnel .* ft2(UMiddle,Dxy),DFxy);
    % Save beam state
    UOut(j,:,:) = single(UIn);
end

return % simpleSplitStep.m
```

```
function [Phase1,Phase2] = pwdPhaseScreenMvk(K0,Nxy,Dxy,Dz,Cn2,Ell0,L0)
%[Phase1,Phase2] = pwdPhaseScreenMvk(K0,Nxy,Dxy,Dz,Cn2,Ell0,L0)
% Create two phase screens based on the Paulson-Davis-Wu method for a
% modified von Karman turbulent spectrum. See D. Paulson, C. Wu and C.
% Davis, "Randomized Spectral Sampling for Efficient Simulation of Laser
% Propagation Through Optical Turbulence," Journal of the Optical Society
% of America B, vol. 36, no. 11, pp. 3249-3262, 2019, and M. Charnotskii,
% Four code examples for turbulent phase screens simulation,
% https://doi.org/10.6084/m9.figshare.10565714.v2 (retrieved Sept. 2023)
% Inputs
%   K0 - carrier wavenumber, rad/m
%   Nxy - grid size
%   Dxy - grid spacing, m
%   Dz - propagating step distance, m
%   Cn2 - turbulence's refractive index structure constant, m^-2/3
%   Ell0 - turbulence's inner scale length, m
%   L0 - turbulence's outer scale length, m
% Outputs
%   Phase1 and Phase2: two independent phase screens
%
% Henry Elder, helder@umd.edu

% Number of subharmonic layers
NSH = 5;

% Spatial domain, m
X = (-Nxy/2:Nxy/2-1)*Dxy; % row vector
Y = X'; % column vector

% Frequency domain, rad/m
Dk = 2*pi/(Nxy*Dxy);
K = (-Nxy/2:Nxy/2-1)*Dk;

% Subharmonics prep arguments
% Subharmonic frequency spacings
DkSubHarm = Dk ./ 3.^(1:NSH);
```

```
% Make matrices of each element, 3x3 each (3x3xNSH)
DkSubHarm3D = reshape(repmat(DkSubHarm,9,1),3,3,NSH);
% "Columnize"
DkSubHarm1D = reshape(DkSubHarm3D,9*NSH,1);
% Copy NSH times (3x3xNSH)
SubHarmGridX1D = repmat([-1 0 1],3,1);
SubHarmGridY1D = SubHarmGridX1D';
SubHarmGridX3D = repmat(SubHarmGridX1D,1,1,NSH);
SubHarmGridY3D = repmat(SubHarmGridY1D,1,1,NSH);

% Build PWD phase plane
% Randomly displaced DFT wavevectors (iid U(-Dk/2,Dk/2))
Kx_r = Dk * (rand - 0.5);
Ky_r = Dk * (rand - 0.5);
Kx = K  + Kx_r; % row vector
Ky = K' + Ky_r; % column vector
% High frequency IFT exponent
Expo = exp(-1i*Ky_r.*Y) * exp(-1i*Kx_r.*X); % (NXYxNXY)
% Compute phase PSD
KMatrix = sqrt(repmat(Kx,Nxy,1).^2 + repmat(Ky,1,Nxy).^2);
PowerSpectrum = 2*pi*0.033*K0^2*Cn2*Dz * exp(-(KMatrix/(5.92/Ell0)).^2) ...
                    ./ (KMatrix.^2+(2*pi/L0)^2).^(11/6);
% Remove DC value
PowerSpectrum(Nxy/2+1,Nxy/2+1) = 0;
% Random draw for coefficients
Coefs = (randn(Nxy) + 1i*randn(Nxy)) .* sqrt(PowerSpectrum) * Dk;
% FT for phase screen
% Note that real and imaginary parts are uncorrelated screens
ScreenHighFreq = ft2(Coefs, 1) .* Expo;

% Now build subharmonics
% Wavenumber coordinates for each subharmonic
KSubHarmX = DkSubHarm3D .* (SubHarmGridX3D + (rand(3,3,NSH)-0.5));
KSubHarmY = DkSubHarm3D .* (SubHarmGridY3D + (rand(3,3,NSH)-0.5));
% Columnize
KSubHarmX1D = reshape(KSubHarmX,9*NSH,1);
KSubHarmY1D = reshape(KSubHarmY,9*NSH,1)';
% Compute phase power spectral density
KMatrixSubHarm = sqrt(KSubHarmX1D.*KSubHarmX1D  ...
                      + (KSubHarmY1D.*KSubHarmY1D)');
PowerSpectrumSubHarm = 2*pi*0.033*K0^2*Cn2*Dz                ...
                    * exp(-(KMatrixSubHarm/(5.92/Ell0)).^2) ...
                    ./ (KMatrixSubHarm.^2+(2*pi/L0)^2).^(11/6);
% Remove DC value for all but highest subharmonic
PowerSpectrumSubHarm(5:9:9*(NSH-1)) = 0;
% Random draw for coefficients
Coefs = (randn(9*NSH,1) + 1i*randn(9*NSH,1))    ...
        .* sqrt(PowerSpectrumSubHarm) .* DkSubHarm1D;
ScreenSubHarm = exp(1i*Y*KSubHarmY1D)*diag(Coefs)*exp(1i*KSubHarmX1D*X);

% Sum and return
Screens = (ScreenHighFreq + ScreenSubHarm);
Phase1 = real(Screens);
Phase2 = imag(Screens);
```

```
return % pwdPhaseScreenMvk.m
```

```
function f = ft2(g,dxy)
%f=ft2(g,dxy)
% 2D Fourier transform -- consolidated
f = fftshift(fftn(fftshift(g))) * dxy^2;
end % ft2.m
```

```
function g = ift2(f,dfxy)
%g=ift2(f,dfxy)
% 2D inverse Fourier transform -- consolidated
g = ifftshift(ifftn(ifftshift(f))) * (size(f,1)*dfxy)^2;
end % ift2.m
```

```
function RcSquared = beamWanderVarianceTheory(K0,W0,F0,Cn2,Z)
%RcSquared = beamWanderVarianceTheory(K0,W0,F0,CN2,Z)
% Calculate theoretical beam wander variance for a Gaussian in Kolmogorov
% turbulence, based on Klyatskin, V., Kon, I., On the displacement of
% spatially-bounded light beams in a turbulent medium in the
% Markovian-random-process approximation, Radiophys. Quantum Electron., 15,
% 1051-1061 (1972).
% Inputs
%   K0 - wavenumber, scalar, rad/m
%   W0 - initial spot size, scalar, m
%   F0 - initial phase curvature, scalar, m
%   Cn2 - turbulence structure constant, scalar, m^-2/3
%   Z - propagation distance(s), 1D array, m
RcSquared = zeros(1,length(Z));
for j = 1:length(Z)
    Integrand = @(K,z) (Z(j)-z).^2 .* K.^3 .* (0.033*Cn2*K.^(-11/3))    ...
        .* exp(-(K.^2*W0^2/4) .* ((1-z/F0).^2 + (2*z/(K0*W0^2)).^2)
  ...
        - 2*pi * (K.*z/K0).^(5/3) .* (0.55*K0^2*z*Cn2));
    RcSquared(j) = 4*pi^2*integral2(Integrand, 0, inf, 0, Z(j));
end

end % beamWanderVarianceTheory.m
```

```
function Intensity0 = onAxisIntensityTheory(K0,W0,F0,Cn2,Ell0,L0,Z)
%Intensity0 = onAxisIntensityTheory(K0,W0,F0,Cn2,Ell0,L0,Z)
% Calcualte the theoretical value for ensemble average on-axis intensity of
% a Gaussian beam in modified von Karman turbulence. Based on the equations
% presented in Andrews, L., Phillip, R., "Laser Beam Propagation Through
% Random Media", 2ed, SPIE (2005).
% Inputs
%   K0 - wavenumber, scalar, rad/m
%   W0 - initial spot size, scalar, m
%   F0 - initial phase curvature, scalar, m
```

```
%   Cn2 - turbulence structure constant, scalar, m^-2/3
%   Ell0 - turbulence inner scale length, m
%   L0 - turbulence outer scale length, m
%   Z - propagation distance(s), 1D array, m
% Outputs
%   Intensity0 - ensemble average on-axis intensity at Z, 1D array, V^2/m^2
%
% Henry Elder, helder@umd.edu

% Calculate diffractive spot size, m
Wz = linearGaussianEvolution(K0,W0,F0,inf,0,0,Z);
% Calculate Fresnel term
Lambda = 2*Z./(K0*Wz.^2);
% Loop through propagation distances
Intensity0 = zeros(1,length(Z));
for j = 1:length(Z)
    % Define integrand (with spherical wave structure function)
    if and(Ell0==0,isinf(L0)) % Kolmogorov case
        Integrand = @(Q) Q .* exp(-K0*Q.^2./(4*Lambda(j)*Z(j))) ...
            .* exp(-0.545*Cn2*K0^2*Z(j)*Q.^(5/3));
    else % Modified von Karman turbulence case
        Integrand = @(Q) Q .* exp(-K0*Q.^2./(4*Lambda(j)*Z(j))) ...
            .* exp(-0.545*Cn2*K0^2*Z(j)*Ell0^(-1/3)*Q.^2 .*     ...
                    ((1+Q.^2/Ell0^2).^(-1/6) - 1.329*(Ell0/L0)^(1/3)));
    end
    % Evaluate integrand
    Intensity0(j) = K0^2*W0^2/(4*Z(j)^2) * integral(Integrand,0,10*W0);
end

return % onAxisIntensityTheory.m
```

```
function [Wz,Tz,Uz] = linearGaussianEvolution(K0,W0,F0,T0,C0,K2,Z)
%[Wz,Tz,Uz]=linearGaussianEvolution(K0,W0,F0,T0,C0,K2,Z)
% Calculate the spot-size, duration, and amplitude evolution of a Gaussian
% pulse in free space.
% Inputs
%   K0 - wavenumber, scalar, rad/m
%   W0 - initial spot size, scalar, m
%   F0 - initial phase curvature, scalar, m
%   T0 - initial pulse length, scalar, sec
%   C0 - initial pulse chirp
%   K2 - group velocity dispersion, scalar, m^2/sec
%   Z  - propagation distance(s), 1D array, m
% Outputs
%   Wz - spot size at Z distance(s), 1D array, m
%   Tz - pulse length at Z distance(s), 1D array, sec
%   Uz - (fractional) peak amplitude at Z distance(s), 1D array
%
% Henry Elder, helder@umd.edu

% Spot size evolution
Wz = W0 * sqrt((1-Z/F0).^2 + (2*Z/(K0*W0^2)).^2);
```

```
% Pulse length evolution
Tz = T0 * sqrt((1+2*C0*K2*Z/T0^2).^2 + (2*K2*Z/T0^2).^2);

% Amplitudes via conservation of energy
Uz =  (W0./Wz) .* sqrt(T0./Tz);

return % LinearGaussianEvolution.m
```

```
% testNonLinSplitStepTurb_SCRIPT.m
% Demonstrate the use of simpleNonLinSplitStepTurb.m by observing the
% evolution of a short, Gaussian pulse.
%
% Henry Elder, helder@umd.edu

clear; close all; clc;
% Speed of light
C    = 299792458; % /ms
MU0  = pi*4E-7; % H/m
EPS0 = 1/(MU0*C^2); % F/m
% Specify beam parameters
LAM0 = 800E-9; % wavelength, m
W0   = 0.5E-3; % spot size, m
F0   = inf; % phase curvature, m
T0   = 650E-15; % length, sec
C0   = 0; % chirp
P0 = 2.65E6; % peak power, GW
% Specify medium parameters
N0 = 1.3296; % refractive index
K0 = 2*pi*N0/LAM0; % wavenumber, rad/m
K2 = 250E-28; % group velocity dispersion, s^2/m
CN2 = 0; % turbulence structure constant, m^-2/3
ELL0 = 0; % turbulence inner scale length, m
L0   = 0; % turbulence outer scale length, m
CHI3 = 2.5E-22; % third order nonlinear susceptibility, m^2/V^2
L    = 5; % total propagation distance, m
% Specify sampling parameters
NXY  = 256; % number of transverse grid points
DXY  = 14*W0/NXY; % transverse grid spacing, m
NTAU = 256; % number of temporal grid points
DTAU = 16*T0/NTAU; % temporal grid spacing, sec
NSCREEN = 10; % number of phase screens
DETA = 0.05; % step size, m
NMONTE = 1; % number of Monte Carlo iterations
NLITER = 2; % number of nonlinear iterations

% Now define the rest of the input parameters
X1D = (-NXY/2:NXY/2-1)*DXY;
Tau1D = (-NTAU/2:NTAU/2-1)*DTAU;
[X3D,Y3D,Tau3D] = meshgrid(X1D,X1D,Tau1D); % 3D X, Y, and Tau domains
U0  = (2/W0)*sqrt(P0/(pi*N0*EPS0*C)); % peak field, V/m
UIn = U0 * exp(-(1/W0^2+0.5i*K0/F0)*(X3D.^2+Y3D.^2) ...
               -(1+1i*C0)*Tau3D.^2/T0^2); % input Gaussian pulse, V/m
```

```
% Run simulations
[XCut,TauCut,Energy,Z] =      ...
    simpleNonLinSplitStepTurb(UIn,N0,CHI3,K0,K2, ...
                              DXY,DTAU,DETA,L,    ...
                              NSCREEN,NLITER,     ...
                              CN2,ELL0,L0);

% Compute linear, non-turbulence evolution for comparison
[Wz,Tz,Uz] = linearGaussianEvolution(K0,W0,F0,T0,C0,K2,Z);

%% Display results
tiledlayout(1,2);
% Plot x cuts
nexttile;
plot3(zeros(1,NXY),X1D*1E3,abs(squeeze(UIn(:,NXY/2+1,NTAU/2+1)))*1E-6, ...
      'LineWidth',2);
hold on;
for j = 1:NSCREEN
    plot3(Z(j)*ones(1,NXY),X1D*1E3,abs(XCut(j,:))*1E-6, ...
          'LineWidth',2);
    plot3(Z(j)*ones(1,NXY),X1D*1E3,U0*Uz(j)*exp(-X1D.^2/Wz(j).^2)*1E-6, ...
          'k--','LineWidth',2);
end
grid on; grid minor;
xlabel('Propagation Distance $z$, meters','interpreter','latex');
ylabel('Transverse Coordinate $x$, mm','interpreter','latex');
zlabel('Field Magnitude, MV/m','interpreter','latex');
title('$|U(x,y=0,\tau=0)|$ Evolution','interpreter','latex');
% Plot tau cuts
nexttile;
plot3(zeros(1,NTAU),Tau1D*1E12,                  ...
      abs(squeeze(UIn(NXY/2+1,NXY/2+1,:)))*1E-6,...
      'LineWidth',2);
hold on;
for j = 1:NSCREEN
    plot3(Z(j)*ones(1,NTAU),Tau1D*1E12,abs(TauCut(j,:))*1E-6, ...
          'LineWidth',2);
    plot3(Z(j)*ones(1,NTAU),Tau1D*1E12,             ...
          U0*Uz(j)*exp(-Tau1D.^2/Tz(j).^2)*1E-6,    ...
          'k--','LineWidth',2);
end
grid on; grid minor;
xlabel('Propagation Distance $z$, meters','interpreter','latex');
ylabel('Retarded Time Coordinate $\tau$, ps','interpreter','latex');
zlabel('Field Magnitude, MV/m','interpreter','latex');
title('$|U(x=0,y=0,\tau)|$ Evolution','interpreter','latex');
% End of testNonLinSplitStepTurb_SCRIPT.m
```

```
function [XCut,TauCut,Energy,Z] =    ...
                          simpleNonLinSplitStepTurb(UIn,N0,Chi3,K0,K2, ...
                                                    Dxy,Dtau,Deta,L,    ...
                                                    NScreens,NLIter,   ...
```

```
                                                        Cn2,Ell0,L0)
%[XCut,TauCut,Z]=simpleNonLinSplitStepTurb(UIn,N0,Chi3,K0,K2,Dxy,Dtau,  ...
% Deta,L,NScreens,NLIter,Cn2,Ell0,L0)
% A simple symmetric non-linear Fourier split-step beam propagation in
% turbulence routine. Will return pulse's x-axis and tau-axis field
% profiles state and total energy at L and half-way between each phase
% screen.
% Inputs
%   UIn - initial pulse state, 3D array, [x,y,tau], V/m
%   N0 - medium's refractive index, scalar
%   Chi3 - medium's third-order nonlinear susceptibility, scalar, m^2/V^2
%   K0 - pulse's carrier wavenumber, scalar, rad/m
%   K2 - pulse's GVD parameter, scalar, s^2/m
%   Dxy - x/y grid spacing, scalar, m
%   Dtau - tau grid spacing, scalar, s
%   Deta - propagation step size, scalar, m
%   L - total propagation distance, scalar, m
%   NScreens - number of turbulent phase screens to apply, scalar
%   NLIter - number of iterations for nonlinear step evaluation, scalar
%   Cn2 - turbulence's refractive index structure constant, scalar, m^-2/3
%   Ell0 - turbulence's inner scale length, scalar, m
%   L0 - turbulence's outer scale length, scalar, m
% Outputs
%   XCut - Field profiles along x-axis, 2D array, [z,x], V/m
%   TauCut - Field profiles along tau-axis, 2D array, [z,tau], V/m
%   Energy - Pulse energy, 1D array, J
%   Z - propagation distances for UOut, 1D array, m
%
% Henry Elder, helder@umd.edu

% Speed of light
C    = 299792458; % /ms
MU0  = pi*4E-7; % H/m
EPS0 = 1/(MU0*C^2); % F/m

% Check grid sizing on UIn
if (ndims(UIn) ~= 3) ||             ... % UIn is 3D?
   (size(UIn,1) ~= size(UIn,2)) || ... % Spatial part is square?
   (rem(size(UIn,1),2) ~= 0) ||    ... % Spatial part has even samples?
   (rem(size(UIn,3),2) ~= 0)           % Temporal part has even samples?
    error(['This function requires a square transverse grid and ' ...
           'an even number of grid points for UIn']);
end

% Check that screen-to-screen distance is small enough for Rytov approx.
if 1.23*Cn2*K0^(7/6)*(L/NScreens)^(11/6) > 0.2
    warning(['Turbulence does not obey RytovVariance << 1. ' ...
             'Results may not be accurate']);
end

% Get Z domain for characterizations and phase screens
Z = (1:NScreens)*L/NScreens; % characterization distances, m
ZScreen = [0 Z(1:end-1)] + 0.5*diff([0,Z]); % phase screen distances, m
IndexZ = round(Z/Deta); % split-step indices for characterization
IndexScreen = round(ZScreen/Deta); % split-step indices for phase screens
```

```
NDeta = round(L/Deta); % total number of steps
if (max(IndexZ*Deta - Z) > 10*eps(L)) ||            ...
   (max(IndexScreen*Deta - ZScreen) > 10*eps(L)) || ...
   (rem(L,Deta) > 10*eps(L))
    warning(['Propagation step Deta, total propagation distance L, and' ...
             ' number of phase screens NScreen do not allow for an '    ...
             'integer number of steps between screens and '             ...
             'characterizations. Results may not be accurate']);
end

% Randomize the seed for MATLAB's random number generator
rng('shuffle');

% Define some useful parameters
Nxy = size(UIn,1); % number of spatial grid points
Ntau = size(UIn,3); % number of temporal grid points
DFxy = 1 / (Nxy * Dxy); % frequency domain grid spacing, 1/m
DFtau = 1 / (Ntau * Dtau); % frequency domain grid spacing, Hz
Gamma  = 3i*K0*Chi3/(8*N0^2); % nonlinear prefactor, m/V^2
EnergyFactor = N0*EPS0*C/2 * Dxy^2 * Dtau;

% Define phase factor for Fresnel propagation over distance DEta/2
[Nx3D,Ny3D,Ntau3D] = meshgrid(-Nxy/2:Nxy/2-1, ...
                              -Nxy/2:Nxy/2-1, ...
                              -Ntau/2:Ntau/2-1);
Fresnel = exp((1i/(2*K0) * (2i*pi*DFxy)^2*(Nx3D.^2+Ny3D.^2)    ...
              -1i*K2/2   * (-2i*pi*DFtau)^2*Ntau3D.^2) * Deta/2);

% Define supergaussian taper
SuperGauss = exp(-(Nx3D.^2+Ny3D.^2).^8/(0.43*Nxy)^16 ...
                 -Ntau3D.^16/(0.43*Ntau)^16);

% Initialze flag for when to compute phase screens
ScreenFlag = true;

% Initialize outputs
XCut = zeros(NScreens,Nxy);
TauCut = zeros(NScreens,Ntau);
Energy = zeros(NScreens,1);
% Begin split-step procedure
% hwb = waitbar(0,'Propagating');
for j = 1:NDeta
    % Propagate DEta/2
    UMiddle = ift2p1(Fresnel .* ft2p1(UIn,Dxy,Dtau),DFxy,DFtau);
    % First nonlinear iteration
    UNonLin = exp(Gamma * abs(UMiddle).^2 * Deta) .* UMiddle;
    UOut = ift2p1(Fresnel .* ft2p1(UNonLin,Dxy,Dtau),DFxy,DFtau);
    % Iterate nonlinear solution
    for jj = 1:NLIter
        % Use trapezoidal rule to estimate nonlinear contribution
        UNonLin = exp(Gamma * (abs(UIn).^2 + abs(UOut).^2) * Deta/2)  ...
                        .* UMiddle;
        UOut = ift2p1(Fresnel .* ft2p1(UNonLin,Dxy,Dtau),DFxy,DFtau);
    end
    % Check if we need to apply a phase screen
```

```
    if any(j == IndexScreen)
        % Apply phase screen
        if ScreenFlag % Need to compute screens
            [Phase1,Phase2] = pwdPhaseScreenMvk(K0,Nxy,Dxy,L/NScreens,  ...
                                                Cn2,Ell0,L0);
            UOut = UOut .* exp(1i*Phase1);
            ScreenFlag = false;
        else % Do not need to compute new screens
            UOut = UOut .* exp(1i*Phase2);
            ScreenFlag = true;
        end
    end
    % Check if we need to store beam state
    if any(j == IndexZ)
        % Extract desired parameters
        [~,ii] = find(j == IndexZ);
        XCut(ii,:) = squeeze(UOut(:,Nxy/2+1,Ntau/2+1));
        TauCut(ii,:) = squeeze(UOut(Nxy/2+1,Nxy/2+1,:));
        Energy(ii) = EnergyFactor * sum(abs(UOut).^2,'all');
    end
    % Apply taper and set UIn for next step
    UIn = SuperGauss .* UOut;
%     waitbar(j/NDeta(end),hwb);
end
% close(hwb);

return % simpleNonLinSplitStepTurb.m
```

```
function f = ft2p1(g,dxy,dt)
%F=FT2P1(G,DXY,DT)
% 3D (2D space, 1D time) inverse Fourier transform -- consolidated
f = fftshift(fftn(fftshift(g))) * dxy^2 * dt;
end % ft2p1.m
```

```
function g = ift2p1(f,dfxy,dft)
%G=IFT2P1(F,DFXY,DFT)
% 3D (2D space, 1D time) inverse Fourier transform -- consolidated
% indexing of f should be [space,space,time]
g = ifftshift(ifftn(ifftshift(f))) * (size(f,1)*dfxy)^2 * size(f,3)*dft;
end % ift2p1.m
```

```
% testNonLinSplitStepFiber_SCRIPT.m
% Demonstrate the use of simpleNonLinSplitStepFiber.m using the
% "bright-dark" soliton pair example from Agrawal, "Nonlinear Fiber Optics,
% 5ed", Academic Press (2013), section 7.3.1. Mode 1 will be the "dark"
% soliton -- that is, it the "turning off" of a CW beam that acts as the
% wave. Mode 2 is the "bright" soliton, which is just the opposite (and the
% usual case). This test case demonstrates the accurate implementation if
% dispersion (to second order), SPM, and XPM.
%
```

```
% Henry Elder, helder@umd.edu

clear; close all; clc;
% Speed of light
C    = 299792458; % m/s
MU0  = pi*4E-7; % H/m
EPS0 = 1/(MU0*C^2); % F/m
% Specify some beam and fiber parameters
LAM1 = 1450E-9; % mode 1 wavelength, m
BETAS1 = [1.5/C, -1.5E-25]; % mode 1 dispersion, s/m and s^2/m
QSPM1 = 1E15; % mode 1 SPM overlap integral, V^4/W^2-m^2
BETAS2 = [BETAS1(1),  1.0E-25]; % mode 2 dispersion, s/m and s^2/m
QSPM2 = QSPM1; % mode 2 SPM overlap integral, V^4/W^2-m^2
LAMREF = 1100E-9; % reference (central) wavelength, m
QXPM = 2*QSPM1; % mode 1-2 XPM overlap integral, V^4/W^2-m^2
T0   = 100E-15; % length of solitons, sec
CHI3 = 2.5E-22; % third order nonlinear susceptibility, m^2/V^2
L     = 0.5; % total propagation distance, m
% Specify sampling parameters
NTAU  = 2^19; % number of temporal grid points
DTAU  = 400*T0/NTAU; % temporal grid spacing, sec
NSAVE = 5; % number of intermediate save points
DETA  = 1E-3; % step size, m
NLITR = 2; % number of nonlinear iterations

% Now define the rest of the input parameters
FreqRef = 2*pi*C/LAMREF; % central frequency, rad/sec
Omega1  = 2*pi*C/LAM1 - FreqRef; % mode 1 detuning, rad/sec
Omega2  = -abs(BETAS1(2))*Omega1/BETAS2(2); % mode 2 detuning, rad/sec
Gamma1 = EPS0*CHI3*(FreqRef+Omega1)*QSPM1/8; % mode 1 nonlinear parameter
Gamma2 = EPS0*CHI3*(FreqRef+Omega2)*QSPM2/8; % mode 2 nonlinear parameter
B1sqrd = (2*Gamma1*BETAS2(2)-Gamma2*BETAS1(2))/(3*T0^2*Gamma1*Gamma2);
B2sqrd = (Gamma1*BETAS2(2)-2*Gamma2*BETAS1(2))/(3*T0^2*Gamma1*Gamma2);
Beta1Ref = BETAS1(1) - BETAS1(2)*Omega1; % reference group velocity, s/m

% Define input soliton waveforms
% Taper the bright soliton to avoid wraparound effects
NTau1D = -NTAU/2:NTAU/2-1;
Tau = NTau1D*DTAU; % Retarded time domain, sec
SuperGauss = exp(-NTau1D.^16/(0.43*NTAU)^16);
A1In = sqrt(B1sqrd)*tanh(Tau/T0).*exp(-1i*Omega1*Tau) .* SuperGauss;
A2In = sqrt(B2sqrd)*sech(Tau/T0).*exp(-1i*Omega2*Tau);

% Run simulation
[A1Out,A2Out,Z] =  ...
         simpleNonLinSplitStepFiber(A1In,(FreqRef+Omega1),BETAS1,QSPM1, ...
                                    A2In,(FreqRef+Omega2),BETAS2,QSPM2, ...
                                    Beta1Ref, QXPM, CHI3,               ...
                                    DTAU,DETA,L,NSAVE,NLITR);

% Display results
tiledlayout(1,2);
% Plot dark soliton (mode 1)
nexttile;
plot3(zeros(1,NTAU),Tau*1E15,abs(A1In),'linewidth',2);
```

```
hold on;
for j = 1:NSAVE
    plot3(Z(j)*ones(1,NTAU),Tau*1E15,abs(A1Out(j,:)),'linewidth',2);
end
grid; grid minor; ylim([-5*T0 5*T0]*1E15);
xlabel('Propagation Distance $z$, meters','interpreter','latex');
ylabel('Retarded Time $\tau$, fs','interpreter','latex');
zlabel('Field Magnitude, V/m','interpreter','latex');
title('Dark Soliton Evolution','interpreter','latex');
% Plot bright soliton (mode 2)
nexttile;
plot3(zeros(1,NTAU),Tau*1E15,abs(A2In),'linewidth',2); hold on;
for j = 1:NSAVE
    plot3(Z(j)*ones(1,NTAU),Tau*1E15,abs(A2Out(j,:)),'linewidth',2);
end
grid; grid minor; ylim([-5*T0 5*T0]*1E15);
xlabel('Propagation Distance, $z$, m','interpreter','latex');
ylabel('Retarded Time $\tau$, fs','interpreter','latex');
zlabel('Field Magnitude, V/m','interpreter','latex');
title('Bright Soliton Evolution','interpreter','latex');

% End of testNonLinSplitStepFiber_SCRIPT.m
```

```
function [A1Out,A2Out,Z] =  ...
            simpleNonLinSplitStepFiber(A1In,Omega1,Betas1,Qspm1, ...
                                       A2In,Omega2,Betas2,Qspm2, ...
                                       Beta1Ref,Qxpm,Chi3,       ...
                                       Dtau,Deta,L,NSaves,NLIter)
%[A1Out,A2Out,Z]= ...
%   simpleNonLinSplitStepFiber(A1In,Omega1,Betas1,Qspm1, ...
%                              A2In,Omega2,Betas2,Qspm2, ...
%                              Beta1Ref,Qxpm,Chi3,       ...
%                              Dtau,Deta,L,NSaves,NLIter)
% A simple symmetric non-linear Fourier split-step beam propagation in
% fiber routine for two pulses. Will return the pulses' states at L and
% NSaves distances along the fiber.
% Inputs
%   A1In - initial pulse state for mode 1, 1D array, [tau], W
%   Omega1 - mode 1 carrier frequency, scalar, rad/s
%   Betas1 - dispersion parameters for mode 1 as a Taylor series, 1D array,
%       SI units
%   Qspm1 - self-phase modulation overlap integral for mode 1, scalar,
%       (V/m)^4/(W/m)^2
%   A2In, Omega1, Betas2, Qspm2 - same as above, but for mode 2
%   Beta1Ref - reference inverse-group-velocity for retarded time frame,
%       scalar, s/m
%   Qxpm - cross-phase modulation overlap integral, scalar, (V/m)^4/(W/m)^2
%   Chi3 - third-order nonlinear susceptibility of fiber, scalar, m^2/V^2
%   Dtau - tau grid spacing, scalar, s
%   Deta - propagation step size, scalar, m
%   L - total propagation distance, scalar, m
%   NSaves - number of locations along fiber to save pulse states, scalar
%   NLIter - number of iterations for nonlinear step evaluation, scalar
```

```
% Outputs
%   A1Out - output mode 1 state, 2D array, [step,tau], W
%   A2Out - output mode 2 state, 2D array, [step,tau], W
%   Z - propagation distances for A1Out and A2Out, 1D array, m
%
% Henry Elder, helder@umd.edu

% Speed of light
C    = 299792458;
MU0  = pi*4E-7;
EPS0 = 1/(MU0*C^2);

% Check grid sizing on A1In and A2In
if (length(A1In) ~= length(A2In)) || ... % A1In and A2In same length?
   (rem(length(A1In),2) ~= 0)            % Even number of samples?
    error(['This function requires the input mode profiles to have the '...
           'same length, and have an even number of grid points']);
end

% Get Z domain for state characterizations
Z = (1:NSaves)*L/NSaves; % characterization distances, m
IndexZ = round(Z/Deta); % split-step indices for characterization
NDeta = round(L/Deta); % total number of steps
if (max(IndexZ*Deta - Z) > 10*eps(L)) ||            ...
   (rem(L,Deta) > 10*eps(L))
    warning(['Propagation step Deta, total propagation distance L, and' ...
             ' number of characterizations NSaves do not allow for an ' ...
             'integer number of steps between characterizations. '      ...
             'Results may not be accurate']);
end

% Define some useful parameters
Ntau = length(A1In); % number of temporal grid points
DFtau = 1 / (Ntau * Dtau); % frequency domain grid spacing, Hz
Alpha1 = 1i*EPS0*Chi3*Omega1/8; % (complex) mode 1 NL prefactor
Alpha2 = 1i*EPS0*Chi3*Omega2/8; % (complex) mode 2 NL prefactor

% Define phase factors for linear propagation over distance DEta/2
Ntau1D = (-Ntau/2:Ntau/2-1);
% Accrue dispersion exponent for mode 1
DispersionPhase1 = (Beta1Ref - Betas1(1)) * (-2i*pi*DFtau*Ntau1D);
for j = 2:length(Betas1)
    DispersionPhase1 = DispersionPhase1 ...
          + (1i)^(j+1)/factorial(j) * Betas1(j) * (-2i*pi*DFtau*Ntau1D).^j;
end
% Convert to phase factor over Deta/2
Dispersion1 = exp(DispersionPhase1 * Deta/2);
% Accrue dispersion exponent for mode 2
DispersionPhase2 = (Beta1Ref - Betas2(1)) * (-2i*pi*DFtau*Ntau1D);
for j = 2:length(Betas2)
    DispersionPhase2 = DispersionPhase2 ...
          + (1i)^(j+1)/factorial(j) * Betas2(j) * (-2i*pi*DFtau*Ntau1D).^j;
end
% Convert to phase factor over Deta/2
Dispersion2 = exp(DispersionPhase2 * Deta/2);
```

```
% Define supergaussian taper
SuperGauss = exp(-Ntau1D.^16/(0.43*Ntau)^16);

% Begin split-step procedure
A1Out = single(zeros(NSaves,Ntau));
A2Out = single(zeros(NSaves,Ntau));
hwb = waitbar(0,'Propagating');
for j = 1:IndexZ(end)
    % Propagate DEta/2
    A1Middle = ift1(Dispersion1 .* ft1(A1In,Dtau),DFtau);
    A2Middle = ift1(Dispersion2 .* ft1(A2In,Dtau),DFtau);
    % First nonlinear iteration
    A1NonLin = exp(Alpha1*Deta *    ...
                   (Qspm1*abs(A1Middle).^2+Qxpm*abs(A2Middle).^2)) ...
                .* A1Middle;
    A2NonLin = exp(Alpha2*Deta *    ...
                   (Qxpm*abs(A1Middle).^2+Qspm2*abs(A2Middle).^2)) ...
                .* A2Middle;
    A1End = ift1(Dispersion1 .* ft1(A1NonLin,Dtau),DFtau);
    A2End = ift1(Dispersion2 .* ft1(A2NonLin,Dtau),DFtau);
    % Iterate nonlinear solution
    for jj = 1:NLIter
        % Use trapezoidal rule to estimate nonlinear contribution
        A1NonLin = exp(Alpha1*Deta/2 *                    ...
                   (Qspm1*(abs(A1In).^2+abs(A1End).^2) ...
                   +Qxpm*(abs(A2In).^2+abs(A2End).^2))) .* A1Middle;
        A2NonLin = exp(Alpha2*Deta/2 *                    ...
                   (Qxpm*(abs(A1In).^2+abs(A1End).^2) ...
                   +Qspm2*(abs(A2In).^2+abs(A2End).^2))) .* A2Middle;
        A1End = ift1(Dispersion1 .* ft1(A1NonLin,Dtau),DFtau);
        A2End = ift1(Dispersion2 .* ft1(A2NonLin,Dtau),DFtau);
    end
    % Check if we need to store beam state
    if any(j == IndexZ)
        % Save envelopes
        [~,ii] = find(j == IndexZ);
        A1Out(ii,:) = A1End;
        A2Out(ii,:) = A2End;
    end
    % Apply taper and set AIn for next step
    A1In = SuperGauss .* A1End;
    A2In = SuperGauss .* A2End;
    waitbar(j/NDeta(end),hwb);
end
close(hwb);

return % simpleNonLinSplitStepFiber.m
```

```
function f = ft1(g,dx)
%F=FT1(G,DX)
%1D Fourier transform -- consolidated
f = fftshift(fft2(fftshift(g))) * dx;
end % ft1.m
```

```
function g = ift1(f,df)
%G=IFT1(F,DF)
%1D inverse Fourier transform -- consolidated
g = ifftshift(ifft2(ifftshift(f))) * (length(f)*df);
end
```

References

[1] J. D. Jackson, Classical Electrodynamics, New York: John Wiley & Sons, 1962.

[2] R. A. Beth, "Mechanical Detection and Measurement of the Angular Momentum of Light," *Phys. Rev.,* vol. 50, no. 2, 1936.

[3] L. Allen, M. W. Beijersbergen, R. J. C. Spreeuw and J. P. Woerdman, "Orbital Angular Momentum of Light and the Transformation of Laguerre-Gaussian Laser Modes," *Physical Review A,* vol. 45, no. 11, 1992.

[4] H. He, M. E. J. Friese, N. R. Heckenberg and H. Rubinsztein-Dunlop, "Direct Observation of Transfer of Angular Momentum to Absorptive Particles from a Laser Beam with a Phase Singularity," *Physical Review Letters,* vol. 75, no. 5, 1995.

[5] M. P. J. Lavery, F. C. Speirits, S. M. Barnett and M. J. Padgett, "Detection of a Spinning Object Using Light's Orbital Angular Momentum," *Science,* vol. 341, no. 6145, pp. 537-540, 2013.

[6] N. Cvijestic, G. Milione, E. Ip and T. Wang, "Detecting Lateral Motion Using Light's Orbital Angular Momentum," *Nature Scientific Reports,* 2015.

[7] G. Gibson, J. Courtial and M. Padgett, "Free-Space Information Transfer Using Light Beams Carrying Orbital Angular Momentum," *Optics Express,* vol. 12, no. 22, 2004.

[8] Y. Ren, Z. Wang, P. Liao, L. Li, G. Xie, H. Huang, Z. Zhao, Y. Yan, N. Ahmed, A. Willner, M. Lavery, N. Ashrafi, S. Ashrafi, R. Bock, M. Tur, I. Djordjevic, M. Niefeld and A. Willner, "Experimental Characterization of a 400 Gbit/s Orbital Angular Momentum Multiplexed Free-Space Optical Link Over 120 m," *Optics Express,* vol. 41, no. 3, 2016.

[9] M. Mirhosseini, M. Malik, Z. Shi and R. W. Boyd, "Efficient Separation of the Orbital Angular Momentum Eigenstates of Light," *Nature Communications,* vol. 4, no. 2781, 2013.

[10] D. G. Grier, "A Revolution in Optical Manipulation," *Nature,* vol. 424, pp. 810-816, 2003.

[11] T. A. Klar, E. Engel and S. W. Hell, "Breaking Abbe's Diffraction Resolution Limit in Flourescence Microscopy with Stimulated Emission Depletion Beams of Various Shapes," *Phys Rev E,* vol. 64, p. 066613, 2001.

[12] L. Yan, P. Gregg, E. Karimi, A. Rubano, L. Marrucci, R. Boyd and S. Ramachandran, "Q-Plate Enabled Spectrally Diverse Orbital-Angular-Momentum Conversion for Stimulated Emission Depletion Microscopy," *Optica,* vol. 2, no. 10, pp. 900-903, 2015.

[13] P. W. Milonni and J. H. Eberly, Laser Physics, Hoboken: Wiley & Sons, 2010.

[14] N. Chattrapiban, E. A. Rogers, D. Cofield, W. T. Hill and R. Roy, "Generation of Nondiffracting Bessel Beams By Use of a Spatial Light Modulator," *Optics Letters,* vol. 28, no. 22, pp. 2183-2185, 2003.

[15] M. A. Bandres and J. C. Gutiérrez-Vega, "Ince-Gauss Beams," *Optics Letters,* vol. 29, no. 2, pp. 144-146, 2004.

[16] L. F. Richardson, Weather Prediction by Numerical Process, Cambridge: Cambridge University Press, 1922.

[17] A. N. Kolmogorov, "The Local Structure of Turbulence in an Incompressible Viscous Fluid for Very Large Reynolds Numbers," *C. R. (Doki) Academy of Science, USSR,* vol. 30, pp. 301-305, 1941.

[18] L. Andrews and R. Phillips, Laser Beam Propagation Through Turbulent Media, Second Edition, Bellingham, Washington: SPIE, 2005.

[19] M. Charnotskii, "Common Ommisions and Misconceptions of Wave Propagation in Turbulence: Discussion," *Journal of the Optical Society of America,* vol. 29, no. 5, 2012.

[20] A. Ishimaru, Wave Propagation and Scattering in Random Media, Volume 2, New York: Academic Press, Inc., 1978.

[21] C. Paterson, "Atmospheric Turbulence and Orbital Angular Momentum of Single Photons for Optical Communication," *Physical Review Letters,* vol. 94, 2005.

[22] C. M. Mabena and F. S. Roux, "Optical Orbital Angular Momentum Under Strong Scintillation," *Physical Review A,* vol. 99, p. 013828, 2019.

[23] C. Y. Young, Y. V. Gilchrest and B. Macon, "Turbulence Induced Beam Spreading of Higher Order Mode Optical Waves," *Optical Engineering,* vol. 41, no. 5, pp. 1097-1103, 2002.

[24] J. A. Anguita, H. Rodriguez and C. Quezada, "Experimental Propagation of Optical Laguerre-Gauss Beams in Turbulence," in *2014 IEEE Aerospace Conference*, Big Sky, Montana, 2014.

[25] R. Boyd, Nonlinear Optics, 4rd Edition, Orlando, FL: Academic Press, Inc., 2020.

[26] M. Helle, G. DiComo, S. Gregory, A. Mamonau, D. Kaganovich, R. Fischer, J. Palastro, S. Melis and J. Penano, "Beating Optical-Turbulence Limits Using High-Peak-Power Lasers," *Physical Review Applied,* vol. 12, no. 5, 2019.

[27] G. Agrawal, Nonlinear Fiber Optics, 5th Edition, Academic Press, 2013.

[28] P. Sprangle, J. R. Penano and B. Hafizi, "Propagation of Intense Short Laser Pulses in the Atmosphere," *Physical Review E,* vol. 66, no. 4, 2002.

[29] L. T. Vuong, T. D. Grow, A. Ishaaya, A. L. Gaeta, G. W. 't Hooft, E. R. Eliel and G. Fibich, "Collapse of Optical Vortices," *Physical Review Letters,* vol. 96, 2006.

[30] L. Sa and J. Vieira, "Self-Focusing of Multiple Interacting Laguerre-Gauss Beams in Kerr Media," *Physical Review A,* vol. 100, no. 1, 2019.

[31] P. Sprangle, A. Ting and C. M. Tang, "Analysis of Radiation Focusing and Steering in the Free-Electron Laser by Use of a Source-Dependent Expansion Technique," *Physical Review A,* vol. 36, no. 6, 1987.

[32] B. Hafizi, J. R. Penano, J. P. Palastro, R. P. Fischer and G. DiComo, "Laser Beam Self-Focusing in Turbulent Dissipative Media," *Optics Letters,* vol. 42, no. 2, 2017.

[33] A. W. Snyder and J. D. Love, Optical Waveguide Theory, New York: Springer, 1983.

[34] C. Yeh and G. Lindgren, "Computing the Propagation Characteristics of Radially Statified Fibers: An Efficient Method," *Applied Optics,* vol. 16, no. 2, 1977.

[35] S. R. A. Dods, "Fiber Vector Modesolver - Improvements to the Efficient 4×4 Matrix Method," in *Integrated Photonics Research and Applications/Nanophotonics Technical Digest*, 2006.

[36] M. Hammond, "FiMS: Modes of Circular Multi-Step Index Optical Fibers," [Online]. Available: https://www.computational-photonics.eu/fims.html. [Accessed November 2023].

[37] G. Guerra, M. Lonardi, A. Galtarossa, L. Rusch, A. Bononi and L. Palmieri, "Analysis of Modal Coupling Due to Birefringence and Ellipticity in Strongly Guiding Ring-Core OAM Fibers," *Optics Express,* vol. 27, no. 6, 2019.

[38] R. Bhandari, "Nature of the Orbital Angular Momentum (OAM) Fields in a Multilayered Fiber," *OSA Continuum,* vol. 4, no. 6, pp. 1859-1874, 2021.

[39] F. Poletti and P. Horak, "Description of Ultrashort Pulse Propagation in Multimode Optical Fibers," *Journal of the Optical Society of America B,* vol. 25, no. 10, 2008.

[40] C. Antonelli, M. Shtaif and A. Mecozzi, "Modeling of Nonlinear Propagation in Space-Division Multiplexed Fiber-Optic Transmission," *Journal of Lightwave Technology,* vol. 34, no. 1, 2016.

[41] X. Liu, E. N. Christensen, K. Rottwitt and S. Ramachandran, "Nonlinear Four-Wave Mixing with Enhanced Diversity and Selectivity via Spin and Orbital Angular Momentum Conservation," *APL Photonics,* vol. 5, no. 010802, 2019.

[42] A. Kudlinski, A. Bendahmane, D. Labat, S. Virally, R. T. Murray, E. J. R. Kelleher and A. Mussot, "Simultaneous Scalar and Cross-Phase Modulation Instabilities in Highly Birefringent Photonic Crystal Fiber," *Optics Express,* vol. 21, no. 7, 2013.

[43] L. Li, J. Leng, P. Zhou and J. Chen, "Modulation instability induced by intermodal cross-phase modulation in step-index multimode fiber," *Applied Optics,* vol. 58, no. 16, pp. 4283-4287, 2019.

[44] P. Gregg, P. Kristensen, A. Rubano, S. Golowich, L. Marrucci and S. Ramachandran, "Enhanced Spin Orbit Interaction of Light in Highly Confining Optical Fibers For Mode Division Multiplexing," *Nature Communications,* vol. 10, no. 4707, 2019.

[45] S. K. Dacha, W. Zhu, A. Agrawal, K. J. Ritter and T. E. Murphy, "Nonlinear Rotation of Spin-Orbit Coupled States in Hollow Ring-Core Fibers," *Optics*

Express, vol. 30, no. 11, 2022.

[46] K. Rottwitt, J. G. Koefoed, K. Ingerslev and P. Kristensen, "Inter-modal Raman amplification of OAM fiber modes," *APL Photonics,* vol. 4, no. 030802, 2019.

[47] S. K. Dacha, H. F. Elder, A. Agrawal, P. A. Sprangle and T. E. Murphy, "Observation of Conjugate OAM Mode Generation via Modulational Instability in a Hollow Ring-Core Fiber," in *Optica Nonlinear Optics Topical Meeting 2023*, Honolulu, 2023.

[48] L. Burger, I. A. Litvin and A. Forbes, "Simulating Atmospheric Turbulence Using a Phase-Only Spatial Light Modulator," *South African Journal of Science,* vol. 104, no. 3, pp. 129-134, 2008.

[49] P. Jacquemin, B. Fernandez, C. C. Wilcox, T. Martinez and B. Agrawal, "Deep Horizontal Atmospheric Turbulence Modeling and Simulation with a Liquid Crystal Spatial Light Modulator," Naval Postgraduate School, Monterey, 2012.

[50] M. Malik, M. O'Sullivan, B. Rodenburg, M. Mirhosseini, J. Leach, M. P. J. Lavery, M. J. Padgett and R. W. Boyd, "Influence of Atmospheric Turbulence on Optical Communications Using Orbital Angular Momentum for Encoding," *Optics Express,* vol. 20, no. 12, p. 13195, 2012.

[51] D. Fu, Y. Zhou, R. Qi, S. Oliver, Y. Wang, S. M. H. Rafsanjani, J. Zhao, M. Mirhosseini, Z. Shi, P. Zhang and R. W. Boyd, "Realization of a Scalable Laguerre-Gaussian Mode Sorter Based on a Robust Radial Mode Sorter," *Optics Express,* vol. 25, no. 10, p. 33057, 2018.

[52] J. Schmidt, Numerical Simulation of Optical Wave Propagation With Examples in MATLAB, Bellingham, WA: SPIE, 2010.

[53] D. Paulson, C. Wu and C. Davis, "Randomized Spectral Sampling for Efficient Simulation of Laser Propagation Through Optical Turbulence," *Journal of the Optical Society of America B,* vol. 36, no. 11, pp. 3249-3262, 2019.

[54] M. Charnotskii, "Comparison of four techniques for turbulent phase screens simulations," *JOSA A,* vol. 37, no. 5, pp. 738-747, 2020.

[55] V. Klyatskin and I. Kon, "On the Displacement of Spatially-Bound Light Beams in a Turbulent Medium in the Markovian-Random-Process Appoximation," *Radiophys. Quantum Electron.,* vol. 15, pp. 1051-1061, 1972.

[56] J. A. Fleck Jr., J. R. Morris and M. D. Feit, "Time-Dependent Propagation of High Energy Laser Beams Through the Atmosphere," *Applied Physics,* vol. 10, no. 2, pp. 129-160, 1976.

[57] G. Luther, J. Moloney, A. Newell and E. Wright, "Self-Focusing Threshold in Normally Dispersive Media," *Optics Letters,* vol. 19, no. 12, 1994.

[58] P. Chernev and V. Petrov, "Self-Focusing of Light Pulses in the Presence of Normal Group-Velocity Dispersion," *Optics Letters,* vol. 17, no. 3, 1992.

[59] J. W. Cooley and J. W. Tukey, "An Algorithm for the Machine Calculation of Complex Fourier Series," *Mathematics of Computation,* pp. 297-301, 1965.

[60] A. E. Siegman, "Defining the Effective Radius of Curvature of a Nonideal Optical Beam," *IEEE Journal of Quantum Electronics,* vol. 27, no. 5, pp. 1146-1148, 1991.

[61] S. Minardi, F. Eilenberger, Y. V. Kartashov, A. Szameit, U. Röpke, K. J., K. Schuster, H. Bartelt, S. Nolte, L. Torner, F. Lederer, .. A. Tünnermann and T. Pertsch, "Three-Dimensional Light Bullets in Arrays of Waveguides," *Physical Review Letters,* vol. 105, no. 26, p. 263901, 2010.

[62] G. DiComo, M. Helle, J. Peñano, A. Ting, A. Schmitt-Sody and J. Elle, "Implementation of a Long Range, Distributed-Volume, Continuously Variable Turbulence Generator," *Applied Optics,* vol. 55, no. 19, pp. 5192-5197, 2016.

[63] J. W. Fleming, "Dispersion in GeO2-SiO2 Glasses," *Applied Optics,* vol. 23, no. 24, 1984.

[64] A. Wada, S. Okude, T. Sakai and R. Yamauchi, "GeO2 Concentration Dependence of Nonlinear Refractive Index Coefficients of Silica-Based Optical Fibers," *Electronics and Communications in Japan, Part 1,* vol. 79, no. 11, 1996.

[65] R. A. Beth, "Mechanical Detection and Measurement of the Angular Momentum of Light," *Physical Review,* vol. 50, no. 2, 1936.

[66] T. A. Klar, E. Engel and S. W. Hell, "Breaking Abbe's Diffraction Resolution Limit in Flourescence Microscopy with Stimulated Emission Depletion Beams of Various Shapes," *Physical Review E,* vol. 64, p. 066613, 2001.

[67] L. Li, J. Leng, P. Zhou and J. Chen, "Modulation Instability Induced by Intermodal Cross-Phase Modulation in Step-Index Multimode Fiber," *Applied Optics,* vol. 58, no. 16, pp. 4283-4287, 2019.

[68] S. Trillo, S. Wabnitz, E. M. Wright and G. I. Stegeman, "Optical Solitary Waves Induced by Cross-Phase Modulation," *Optics Letters,* vol. 13, no. 10, pp. 871-873, 1988.

[69] M. Mirhosseini, M. Malik, Z. Shi and R. W. Boyd, "Efficient Separation of the Orbital Angular Momentum Eigenstates of Light," *Nature Communications,* vol. 4, 2013.

[70] C. M. Mabena and F. S. Roux, "Optical Orbital Angular Momentum Under Strong Scintillation," *Physical Review A,* vol. 99, 2019.

[71] K. Rottwitt, J. G. Koefoed, K. Ingerslev and P. Kristensen, "Inter-Modal Raman Amplification of OAM Fiber Modes," *APL Photonics,* vol. 4, no. 030802, 2019.